# ACTUAL PROBLEMS OF PARTICLE PHYSICS

*Proceedings of International School-Seminar*

*Vol. I*

PROCEEDINGS of
INTERNATIONAL SCHOOL-SEMINAR
"ACTUAL PROBLEMS OF PARTICLE PHYSICS"

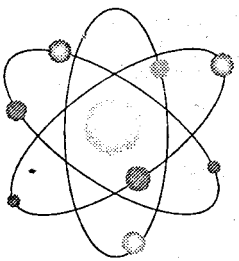

Joint Institute for Nuclear Research (Dubna, Russia),
National Center of Particle and High Energy Physics (Minsk, Belarus),
Institute of Physics (Minsk, Belarus) & Institute of Metal Polymer Systems (Gomel, Belarus) of National Academy of Sciences of Belarus,
Gomel State University,
Gomel Polytechnic Institute



July 30 – August 8, 1999, Gomel, Belarus

# Accelerator Physics, LHC Program, Physics "in" and "out" of Framework of Standard Model, Soft and Hard QCD Processes, Quantum Field Theory, Relativistic Nuclear Physics

Edited by the Editorial Board

Vol. I

Dubna, 2000

C346(04)+C343(04)

## INTERNATIONAL ADVISORY COMMITTEE:

V.Kadyshevsky JINR (Chairman), N.Amaglobeli IHEP, A.Baldin JINR, M.Danilov ITEP, M.Della Negra CERN, S.Dubnicka IP, V.Dzhelepov JINR, M.Finger Charl. Univ., V.Gaisyonok SCST, P.Jenni CERN, G.Kozlov Min. of Sc., A.Kozulin BSU, A.Logunov IHEP, V.Matveev INR, I.Meshkov JINR, V.Rubakov INR, V.Savrin NPI MSU, D.Shirkov JINR, A.Skrinsky Ac. of Sc. & BINP, R.Sosnovsky INP, P.Spillantini INFN, V.Strazhnev Min. of Ed., N.Tyurin IHEP, H.Vartapetyan ErPI, A.Voytovich Nat. Ac. of Sc., A.Wagner DESY, I.Zalyubovsky KhSU

## ORGANIZING COMMITTEE from JINR:

A.Sissakian (Chairman), N.Skatchkov (Vice-Chairman, Rector), S.Shulga (Scientific Secretary), E.Russakovich (School Secretary), P.Bogolyubov, J.Budagov, A.Filippov, I.Golutvin, I.Ivanov, S.Ivanova, V.Kekelidze, A.Kurilin, A.Malakhov, M.Nazarenko, N.Russakovich

## ORGANIZING COMMITTEE from BELARUS:

V.Gaisyonok SCST (Chairman), N.Shumeiko NC PHEP (Vice-Chairman), Y.Pleskachevsky IMMPS (Vice-Chairman), N.Maksimenko GSU (Pro-rector), V.Andreev GSU (Scientific Secretary), A.Tolkachev NC PHEP (Scientific Secretary), V.Baryshevsky RINP, A.Bogush SIP, S.Chigrinov "Sosny", V.Davydovych Gomel Executive Committee, N.Kazak SIP, A.Kukharev Council of Ministers, V.Kuvshinov SIP, A.Pankov GSTU, S.Rakhmanov BSU, V.Rumyantsev NC PHEP, S.Scherbakov GUT, A.Shaginyan GSTU, L.Shemetkov GSU, I.Solovtsov GSTU, S.Timoshin GSTU, L.Tomilchik SIP

## EDITORIAL BOARD:

A.Bogush, V.Gaisyonok, M.Maksimenko, A.Pankov, S.Shulga, N.Shumeiko, A.Sissakian, N.Skatchkov, P.Starovoitov, A.Tolkachev

ISBN 5-85165-579-8



## CONTENTS

## Preface

International scientific conferences and seminars in different fields held in Belarus significantly facilitate the development of science in the republic. The «Golden Sands» holiday center in Gomel region hosted seminars on micro-world physics in 1971, 1973, 1977 and 1997. The school-seminar on particle physics is held here again in August 1999. The initiative to hold all these events belongs to the outstanding scientists such as N.Bogolubov, F.Fedorov, V.Kadyshevsky, V.Bely, B.Bokut and their followers A.Sissakian, N.Skatchkov, N.Shumeiko, A.Bogush, L.Tomilchik, N.Maksimenko, Yu.Pleskachevsky, S.Shcherbakov and others.

Micro-world physics or in other words high energy and particle physics is exceptionally important for understanding fundamental basis of structure and properties of matter and development and practical use of update technologies in micro-electronics, computing, deep vacuum and law temperatures physics, radioactive engineering and other fields. The main aim of the present school-seminar is educating scientific youth, discussing update fundamental results in modern physics, information and experience exchange in experimental methodology, making working contacts between scientists from leading international and national scientific centers.

The organizers of the International School-Seminar «The Actual Problems of Particle Physics» 1999 are the Joint Institute for Nuclear Research (Dubna), National Center of Particle and High Energy Physics (Belarussian State University), B.Stepanov Institute of Physics, V.Bely Institute of Mechanics of Metal Polymer Systems (National Academy of Science), F.Scaryna Gomel State University and P.Sukhoy Gomel State Technical University (Ministry of Education).

The agenda is packed with scientific lectures and reports on physics and collider technologies, experimental and theoretical problems in particle physics. The problems of experimental equipment for new colliders and fundamental high energy interactions are the key ones. Lectures and reports are delivered by scientists from the institutes-organizers and world-known scientific centers of the USA, Germany, Switzerland, France, Czech Republic, Austria and CIS. CERN Laboratory is represented widely too. There are 26 professors and 29 associate professors among the participants of the school-seminar. One of the participants represents Latin America.

The organizers of the Gomel School-Seminar 1999, scientists and authorities of Gomel Region, the «Golden Sands» holiday center staff hope to keep the tradition of holding similar events going in the next millennium.

Organizing Committee



# LHC program: ATLAS, CMS

# Physics at the LHC: ATLAS performance

S. Tapprogge[a]

[a]CERN, EP Division, Geneva

The expected performance of the ATLAS detector at LHC is summarized for a variety of physics processes. Besides a description of the discovery potential for Higgs bosons, Supersymmetry and other new physics processes, examples for precision measurements of Standard Model processes (such as parton densities, the $W$ boson mass, the top quark mass), of masses and parameters of Higgs bosons and of supersymmetric particles are presented.

## 1. Introduction

This report gives an overview of the physics studies expected to be performed with the ATLAS detector [1] in proton-proton collisions at $\sqrt{s} = 14$ TeV at LHC. The results presented here are documented in more detail in [2], and can be divided into two classes: searches for Higgs boson(s) and physics beyond the Standard Model (SM) and precision measurements of Standard Model and non-Standard Model processes.

In the following section, a brief description of the ATLAS detector is given. The next four sections discuss precision measurements in the areas of QCD, electroweak physics, top quark physics and B physics. Then searches and measurements of Higgs bosons are described. Next, the search for and measurements of supersymmetry (SUSY) are discussed and finally searches for other physics beyond the Standard Model are presented.

## 2. The ATLAS detector

The ATLAS detector[1] is one of the two general purpose $4\pi$ detectors for LHC. The interaction point is surrounded by silicon pixel and silicon strip layers, followed by a transition radiation tracker. These tracking detectors are located inside a 2 T solenoid. Calorimeters are located outside of the solenoid. They consist of liquid Argon (LAr) calorimeters for the e.m. compartment and a combination of iron-scintillator based and LAr based calorimeters for the hadronic part. The muon measurement is performed in the central tracker and by an independent open air-core toroid system with muon detectors. The detector has been optimized in terms of

lepton, photon, jet and missing $E_T$ measurements for studies within the Standard Model and searches and measurements of new physics. Precision measurements of leptons ($e$, $\mu$, $\tau$), photons and jets are possible for pseudo-rapidities of $|\eta| < 2.5$. The measurement of jets and of missing transverse energy (both with calorimetry only) extends up to $|\eta| = 5$.

Due to the huge amount of CPU time needed to simulate in detail the response of the ATLAS detector, most of the results presented here have been obtained from a fast simulation using a parameterized response of the detector. This reponse has been obtained from detailed simulations and for crucial channels (like the case of $H \rightarrow \gamma\gamma$) explicit cross-checks with a full (GEANT based) simulation have been performed.

The running scenario assumed for the machine is that the first three years will be at a luminosity of $10^{33}$ cm$^{-2}$s$^{-1}$, yielding an integrated luminosity of 10 fb$^{-1}$ per year. At the design luminosity of $10^{34}$ cm$^{-2}$s$^{-1}$, a value of 100 fb$^{-1}$ per year is assumed. The ultimate sensitivity is given for 300 fb$^{-1}$. For the examples shown in the next sections, in most cases no details on the selection procedure are given. These can be found in [2], together with other measurements not mentioned here.

## 3. QCD studies

### 3.1. Minimum bias events

At design luminosity, there will be about 25 inelastic interactions per bunch-crossing (i.e. every 25 ns) at the LHC energy. Almost all of these events will be of minimum bias nature, i.e. they will not contain large $p_T$ scattering contributions. Measurements of the properties of these events (to be done at low luminosities to avoid the occurence of pile-up) are essential to understand their influence on measurements of high $p_T$ scattering events, without having to rely on model predictions.

Figure 1 shows the predictions from several models (PYTHIA, PHOJET, ISAJET and HERWIG) for the charged particle density $\mathrm{d}N_{ch}/\mathrm{d}\eta$ and for the transverse momentum spectrum $E \cdot \mathrm{d}^3\sigma/\mathrm{d}p^3$ of the charged particles. The models containing a contribution from hard scattering processes (PYTHIA and PHOJET) agree for $E \cdot \mathrm{d}^3\sigma/\mathrm{d}p^3$, whereas HERWIG and ISAJET predict a steeper spectrum. For $\mathrm{d}N_{ch}/\mathrm{d}\eta$ clear differences in the predictions are observed. The charged particle density (at $|\eta| \approx 0$) varies between 4 (ISAJET) and 8.5 (PYTHIA), where the PYTHIA version 5.724 (solid line) is the model used for minimum bias events in all studies done by ATLAS.



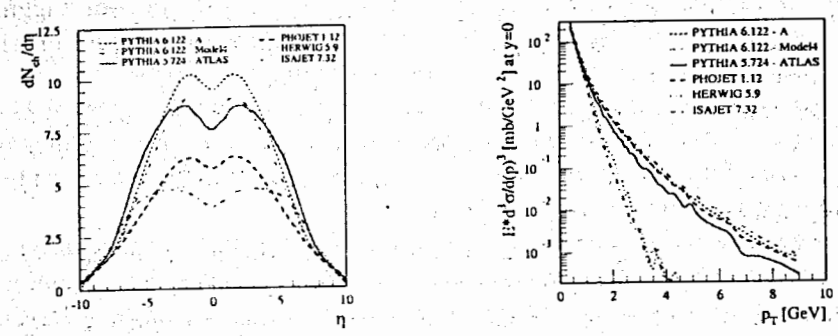


*Figure 1. Charged particle density as a function of pseudorapidity (left) and $p_T$ spectrum of charged particles (right) in minimum bias events for several Monte Carlo models.*

### 3.2. Hard diffractive scattering

Diffractive scattering constitutes a major part of the total cross-section for hadron-hadron scattering and can be described in the framework of Regge theory, when as leading trajectory the Pomeron trajectory is introduced. The first observation of hard processes in diffractive scattering was made by the UA8 collaboration, observing the production of jets together with a leading anti-proton.

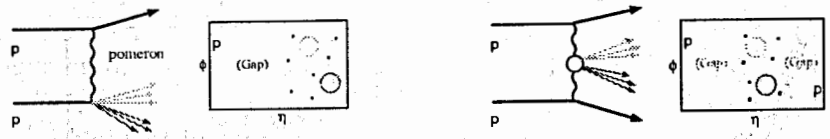


*Figure 2. Sketch of hard single diffractive scattering (left) and hard central diffraction (right).*

In figure 2, signatures of hard diffractive scattering are shown both for single and for central diffraction. Besides one (or two) outgoing leading protons, i.e. protons with a momentum close to the one of the beam particles, the final state contains one (or two) rapidity gaps. These gaps separate the (in the central detector undetected) leading proton(s) from the final state (containing e.g. jets as result of the hard scattering). An optimal detection and measurement of such events needs an extension of the detector beyond the acceptance of $|\eta| = 5$, for tagging (and measure-

ment) of particle production (possibly up to $|\eta| \approx 7.5$) and for tagging and measurement of leading protons. Investigations are ongoing on the feasibility of such detectors and on possible running scenarios.

When both outgoing protons are tagged, the dominating process at high energies is central diffraction. The measurement of both proton momenta would 'transform' the LHC into a Pomeron-Pomeron collider with center-of-mass energies reaching up to 2 TeV.

Besides jets, other probes can be used in hard diffractive scattering to gain information on the partonic content. This includes the production of photons, $W$ and $Z$ bosons and heavy quarks, together with a leading proton and / or a rapidity gap.

### 3.3. Parton densities

A variety of probes will be used to obtain, via hard scattering, information on the parton densities of the proton. $W$- and $Z$ bosons as well as Drell-Yan lepton pairs will give information mostly on the quark (and anti-quark) densities. For the gluon density, the production of direct photons and of $b$ (and $t$) quarks can be used. Jets are sensitive to a combination of quark and gluon densities, where the fraction of events with at least one (anti-)quark entering the hard scattering increases with increasing $E_T$ of the jets.

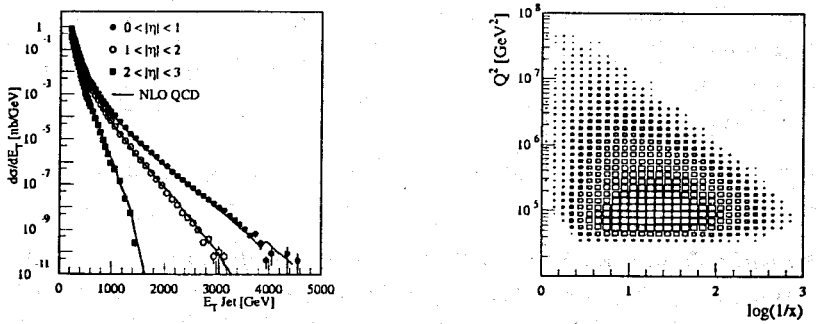


*Figure 3. Inclusive jet cross-section for different pseudo-rapidity ranges (left) and reach in the $(1/x, Q^2)$ plane from di-jet production (right).*

Figure 3 (left part) shows the expected inclusive jet cross-section as a function of the minimal jet transverse energy $E_T^{jet}$ for different ranges in pseudo-rapidity. In case of central production with $|\eta| < 1$ about 30



(3000 resp. $4 \cdot 10^5$) events are expected with $E_T > 3$ TeV ($> 2$ TeV resp. $> 1$ TeV) for an integrated luminosity of 30 fb$^{-1}$. Using the production of di-jet events, one can deduce from the jet properties ($E_T$ and $\eta_{1,2}$) the parton momenta $x_{1,2}$ and the hard scattering scale $Q^2$. In the right part of figure 3, the reach in the $(1/x, Q^2)$ plane is shown for $E_T > 180$ GeV and $|\eta_{1,2}| < 3.2$.

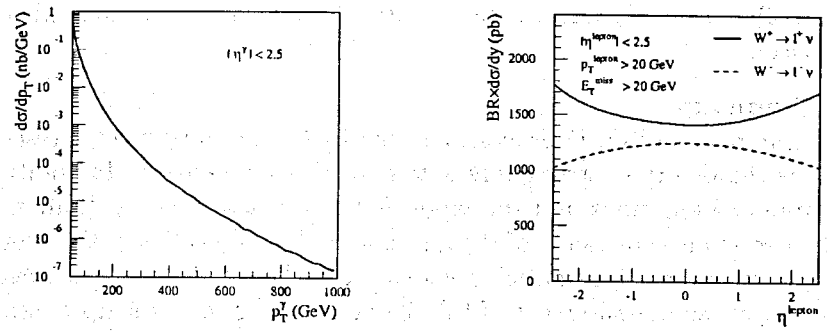


*Figure 4. Cross-section for direct photon production as a function of the transverse momentum $p_T^\gamma$ of the photon (left) and cross-section for $W$ production as a function of the decay lepton pseudo-rapidity $\eta^{lepton}$ (right).*

Direct photon production with $p_T^\gamma > 40$ GeV allows to cover the range of $5 \cdot 10^{-4} < x < 0.2$ with $Q^2 > 10^3$ GeV$^2$. In figure 4 (left part) the expected cross section (at leading order) for direct photon production is shown as a function of the transverse momentum $p_T^\gamma$ of the photon. The production of $W$ ($Z$) bosons probes the parton densities at a scale of $Q^2 = M_W^2$ ($M_Z^2$) and covers the range in Bjorken-$x$ of about $3 \cdot 10^{-4} < x < 10^{-1}$ (for $Q^2 \approx 6(8) \cdot 10^3$ GeV$^2$). Due to the differences between valence and sea quarks, the distributions of $W^+$ and W$^-$ bosons differ in rapidity. More $W^+$ bosons are produced in the forward direction ($|\eta| \gg 0$) than in the central region ($|\eta| \approx 0$). This difference survives in the distribution of the pseudo-rapidity $\eta^{lepton}$ of the decay lepton, as shown in the right part of figure 4. For comparison, the HERA range for deep-inelastic scattering in $x$ is kinematically restricted to $x > 0.01$ for $Q^2 > 10^3$ GeV$^2$ and to $x > 0.1$ for $Q^2 > 10^4$ GeV$^2$.

### 3.4. Strong coupling constant

A precise measurement of the strong coupling constant $\alpha_s$, which would give access to the highest scales up to $\mathcal{O}$(TeV), will be a challenge at LHC. Whereas a measurement based on the inclusive jet cross-section implies a strong correlation with the gluon density, the ratio of the cross-section for 3-jet production to the one for 2-jet production should have a reduced sensitivity to the parton densities. Further studies are needed to quantify the possible accuracy and the use of other channels, like prompt photon production.

### 3.5. Summary

Measurements of QCD processes at the LHC will allow further tests of QCD as the theory of strong interaction at very high energy. In addition, the large cross-sections and the large center-of-mass energy will allow to make precise measurements of the quark and gluon densities in the proton in as yet uncovered kinematical regions. A challenge still to be proven is a highly precise measurement of the strong coupling constant up to scales of $\mathcal{O}$(TeV).

Studies of hard diffractive scattering could also be performed at LHC. These require most likely extensions of the ATLAS detector in order to increase the acceptance for particle production beyond $|\eta| = 5$ and for detection and measurement of leading protons.

## 4. Electroweak physics

### 4.1. Measurement of the $W$ boson mass

The $W$ boson mass is measured in the reaction $pp \rightarrow W + X$, where $W \rightarrow l\nu_l$ with $l = e, \mu$. Due to the unmeasured longitudinal momentum of the neutrino (its transverse momentum $p_T^\nu$ can be reconstructed from the lepton $l$ and the recoil system $X$) no direct mass reconstruction is possible. Instead, the transverse mass $m_T^W$ is used. It is given by the following expression:

$$m_T^W = \sqrt{2p_T^l p_T^\nu (1 - \cos\Delta\phi)}, \qquad (1)$$

where $\Delta\phi$ is the azimuthal angle between the lepton and the neutrino.

The left part of figure 5 shows the expected distribution of $m_T^W$, where the trailing edge is sensitive to $m_W$. Shown are both the distribution at particle level and after including effects of detector smearing. At low luminosity, about $6 \cdot 10^7$ reconstructed $W$ boson events are expected per



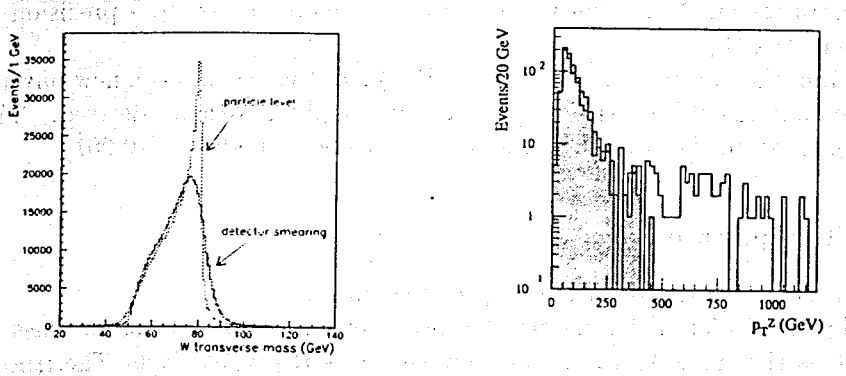


*Figure 5. Transverse mass of the $W$ boson (left) and $p_T^Z$ spectrum for $WZ$ production (right).*

year, giving a negligible statistical uncertainty. The dominating systematic uncertainty will come from the knowledge of the lepton energy scale. If this scale was known to about 0.02 % (the standard assumption is 0.1 %) it would imply an uncertainty of about 15 MeV on the $W$ mass. Further uncertainties are due to the knowledge of the detector energy resolution, the $p_T$ of the $W$, the knowledge of the parton densities and the contribution from radiative decays. Their expected size ranges between 5 and 10 MeV.

### 4.2. Triple gauge boson couplings

These couplings are a consequence of the non-Abelian structure of the SM gauge group. In addition, they could receive contributions from new physics. The vertices for $WWZ$ and $WW\gamma$ (leading to the production of $WZ$ and $W\gamma$ bosons) can be described at tree level in the Standard Model by five parameters. The right part of figure 5 shows the distribution of the transverse momentum $p_T^Z$ of the $Z$ boson in the case of $WZ$ production, for the Standard Model ($\Delta g_1^Z = 0$, shaded histogram) and for a value of $\Delta g_1^Z = 0.05$ (open histogram). After three years of low luminosity, about 1200 events are expected.

### 4.3. Summary

Although the precise measurement of the mass of the $W$ boson at a hadron collider is challenging, first studies indicate that, thanks to the large statistics and the availability of sizeable control samples (e.g. $Z \rightarrow l^+l^-$), an overall precision of about 15 MeV could be achieved (when combining ATLAS and CMS measurements). This however imposes very strong

constraints on the knowledge of the lepton energy scale (to a precision of about 0.02 %).

From the production of $WZ$ (resp. $W\gamma$) pairs, constraints on new physics contributions to the triple gauge boson couplings can be derived. The accuracies on the couplings are expected to be as high as $\mathcal{O}(0.001)$.

## 5. Top quark physics

### 5.1. Measurement of the top quark mass

The gold plated channel for the measurement of the top quark mass at LHC is the single lepton decay channel: $t\bar{t} \to W(jj)bW(l\nu)\bar{b}$. The lepton from one $W$ decay is used to provide a trigger, the other $W$ decay is used to fully reconstruct one top quark decay with one $b$-quark and two light quarks in the final state.

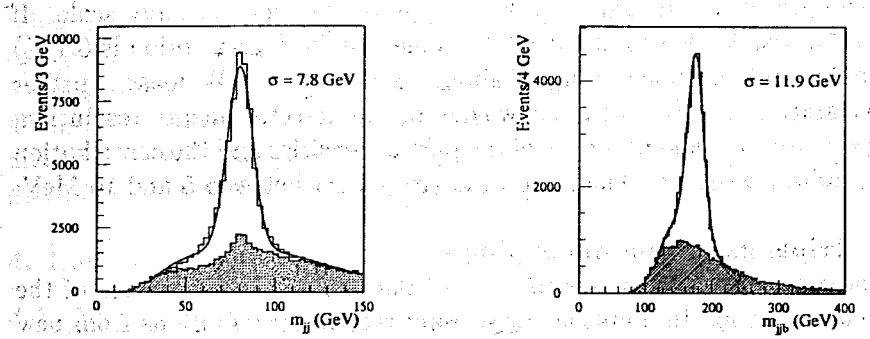


*Figure 6. Invariant mass of the $W \to jj$ decay (left) and the $t \to Wb$ decay (right) from top pair production.*

In the left part of figure 6 the reconstructed mass for the decay $W \to jj$ is shown together the background (shaded histogram), which is dominated by wrong assignments of jets to $W$ decays. In the right part of this figure the invariant mass of the combination of the jet pair from the $W$ with a $b$-tagged jet is shown. Again, the shaded histogram indicates the background. In both cases, clear signals (of $W \to jj$ and $t \to Wb$) are observed. The mass resolution obtained is $\sigma(m_{jj}) = 7.8$ GeV resp. $\sigma(m_{Wb}) = 11.9$ GeV.

Due to the large statistics expected (more than $10^5$ events per year at low luminosity), a negligible statistical uncertainty ($< 0.1$ GeV) on the top



quark mass is expected. The systematic uncertainties are dominated by the knowledge of the jet energy scales (for light quark and $b$ quark jets) and the effects of final state radiation (and to a lesser extent the one of initial state radiation). An overall uncertainty of less than 2 GeV seems reachable.

### 5.2. $t\bar{t}$ resonances

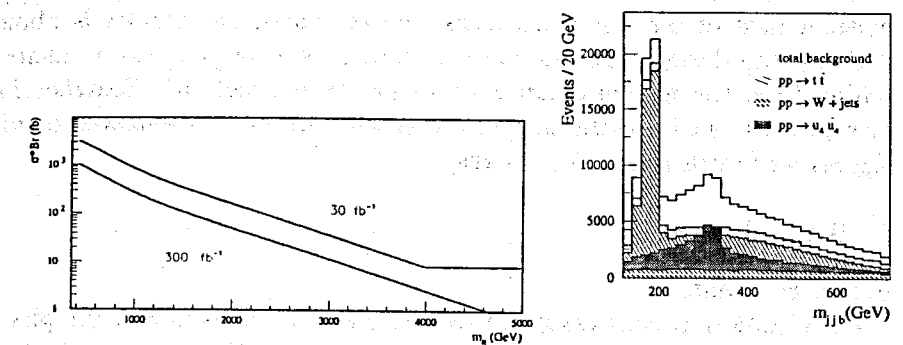


*Figure 7. Sensitivity ($\sigma \cdot BR$) to production of a resonance decaying to $t\bar{t}$ as a function of $m_{t\bar{t}}$ (left) and expected signal from a fourth generation quark $u_4$ ($m(u_4) = 300$ GeV), decaying to $W + b$ (right).*

An investigation has been performed to determine the discovery potential for generic resonances decaying to $t\bar{t}$ pairs. The mass resolution was found to be $\sigma(m(t\bar{t}))/m(t\bar{t}) \approx 7$ %. The sensitivity for a $5\sigma$ discovery ranges from values of $BR \cdot \sigma = 300$ fb at a mass of 1 TeV to about 2 fb at 4 TeV (for 300 fb$^{-1}$), as shown in figure 7 (left part).

### 5.3. Top quark decays and couplings

The branching ratios of top quarks to $b$ quarks (resp. $W$ bosons) are expected to be measurable with a statistical accuracy of $\mathcal{O}(10^{-2})$. Rare decay modes of top quarks (sensitive to flavour changing neutral currents) should be observable for branching ratios between $10^{-4}$ and $10^{-3}$. The production of single top quarks (an electroweak process) can be used to determine the CKM matrix element $V_{tb}$.

### 5.4. Fourth generation quarks

The measurement of the number of light neutrinos (equal to three) done at LEP does not exclude the existence of additional families with heavy

neutrinos. Fourth generation quarks of $u$ type ($u_4$) would decay similarly to a top quark. An example of a signal from the decay of a $u_4$ quark with a mass of 300 GeV is shown in figure 7 (right part), together with the expected background contributions. In the case of $u$ like fourth generation quarks, the discovery reach is extends up to masses of 700 GeV.

### 5.5. Summary

The LHC can be considered as a 'top' factory. Besides an accurate measurement of the top quark mass (the estimated uncertainty is about 2 GeV), top decays and top quark couplings will be precisely measured (either from top pair production or single top production). Searches for new physics can be performed in the production of $t\bar{t}$ resonances or via signals for fourth generation quarks.

## 6. B physics

### 6.1. CP violation

CP violation in weak decays in the Standard Model is due to the phase of the CKM matrix, describing the quark mixing. Unitarity constraints can be described in terms of a triangle, whose angles are $\alpha$, $\beta$ and $\gamma$. CP violation leads to different decay rates for $B^0$ and $\bar{B}^0$ to a CP eigenstate $f$. This can be expressed in terms of a time-dependent asymmetry:

$$A(t) = \frac{N(B^0 \to f)(t) - N(\bar{B}^0 \to f)(t)}{N(B^0 \to f)(t) + N(\bar{B}^0 \to f)(t)} \qquad (2)$$

which has the following functional dependence on $t$:

$$A(t) = a\cos(\Delta m t) + b\sin(\Delta m t). \qquad (3)$$

Here $a$ is the direct CP violation parameter, $b$ is the parameter for mixing induced CP violation and $\Delta m$ the mass difference between the $B$ meson states. For the simplified case of $a = 0$, a time-integrated asymmetry $A^{obs}$ can be defined. This time integrated asymmetry can be expressed as follows

$$A^{obs} \propto D_{tag} D_{back}(D_{int} b + A^P), \qquad (4)$$

where $b \propto \sin 2\beta$. $A^p$ is the asymmetry present in the production and $D_{tag} = 1 - 2p_W$ is the dilution factor for the tagging, where $p_W$ is the mistagging probability. $D_{back} = N_S/(N_S + N_B)$ and $D_{int} = x/(1 + x^2)$ are



the dilution factors for the background (where $N_S$ ($N_B$): number of signal (background) events) and for the time integration ($x = \Delta m/\Gamma$).

To measure CP violation parameters, the flavour of the $B$ meson at production needs to be tagged. This can either be done using lepton tagging (e.g. the muon used for the first level trigger selection) or by $B - \pi$ tagging (correlation of the charge of pions produced close to the $B$ meson).

#### 6.1.1. Measurement of $\sin 2\beta$

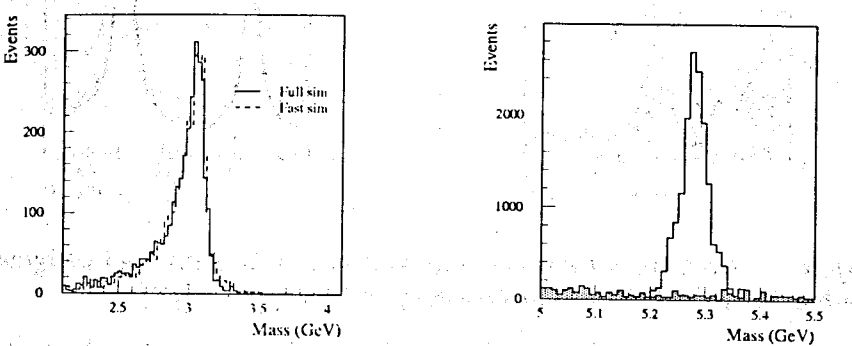


*Figure 8. Invariant mass of $J/\Psi \to ee$ (left) and of $J/\Psi(ee)K^0_s(\pi\pi)$ from $B^0_d \to J/\Psi K^0_s$ and background (right).*

The measurement of $\sin 2\beta$ will be made using the decay of $B^0_d$ mesons to final states with a $J/\Psi$ and a $K^0_s$. In the left part of figure 8 the reconstructed invariant mass of electron pairs from the $J/\Psi$ decay is shown, yielding a mass resolution of about 60 MeV. The tail to lower masses is due to bremsstrahlung energy losses. The mass spectrum from fully simulated events (solid histogram) is well reproduced by a fast simulation of the detector response (dashed histogram). The right part of this figure shows the reconstructed invariant mass of the $J/\Psi(ee)K^0_s(\pi\pi)$ system. A clear $B^0_d$ signal with a mass resolution of 26 MeV is observed.

For three years of running at low luminosity, the expected statistical uncertainty on $\sin 2\beta$ is about 0.010 (when lepton and $B - \pi$ tagging and $J/\Psi \to ee$ and $J/\Psi \to \mu\mu$ decay modes are combined). The expected size of the systematic uncertainty (due to asymmetries in the production, the tagging and the background, as well as the knowledge of the various dilution factors) is about 0.005. Thus the expected precision on $\sin 2\beta$ is better than the expected accuracy from the $e^+e^-$ B-factories (e.g. 0.05 in the case of BaBar).

### 6.1.2. Measurement of the angle $\alpha$

The decay $B_d^0 \to \pi\pi$ is sensitive to the angle $\alpha$, but is theoretically complicated due to the interplay between CP violation contributions from tree and from Penguin amplitudes.

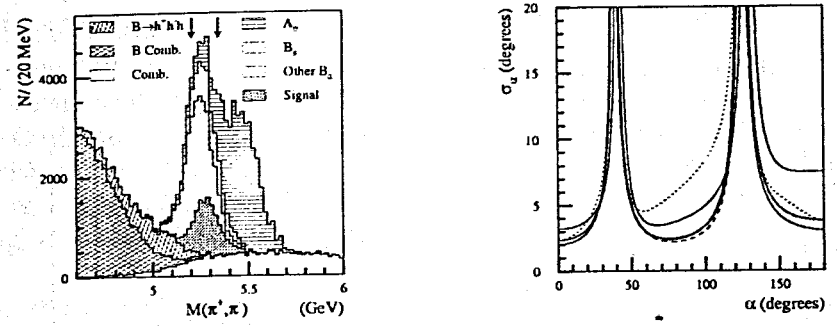


*Figure 9. Reconstructed two pion invariant mass with signal and background contributions (left) and expected accuracy on the angle $\alpha$ (right).*

The measurement of the angle $\alpha$ of the unitrarity triangle is limited by the poor $\pi/K$ separation capabilities of ATLAS (which give at most a $1\sigma$ separation for momenta of about 4 GeV). In the left part of figure 9 the expected distribution for the invariant mass of a reconstructed pion pair is shown. Besides the signal from $B_d \to \pi\pi$ the contributions from other 2 and 3-body decays are shown ($B_d \to \pi K$, $B_s \to \pi K$ or $KK$, $\Lambda_b \to \pi p$ or $Kp$ and $B \to \rho\pi$ or $\pi\pi\pi$).

Nonetheless after three years an accuracy of up to 2° on the angle $\alpha$ can be reached. The exact value depends on various theoretical uncertainties. Figure 9 shows in the right part the dependence of the expected accuracy $\sigma_\alpha$ for $\alpha$ on the value of $\alpha$ itself, for different assumptions on the phase $\delta$ between tree and Penguin amplitudes (showing as solid lines the three values $\delta = 0, 30°, 60°$ - from bottom to top) and for a 50 % uncertainty on the ratio $A_P/A_T$ of the Penguin to the tree amplitude (the dotted line - $\delta = 30°$).

### 6.1.3. Measurement of the angle $\gamma$

The study of the decay $B_s \to J/\Psi\phi$ could be used in principle to determine the angle $\gamma$. The phase $\xi$ of the interference between the weak decay and the decay via mixing is proportional to $\sin\gamma$. However the expected



statistical accuracy of 0.03 on $\xi$ is of the same magnitude as the expected value of $\xi$. Thus an extraction of $\sin\gamma$ does not seem to be feasible.

### 6.2. $B_s^0$ oscillations

Oscillations between the $B_s^0$ and $\bar{B}_s^0$ (which are linear combinations of mass eigenstates with different masses $m_H$ and $m_L$) are expected in the Standard Model. The oscillation frequency depends on the mass difference $\Delta m_s = m_H - m_L$; however no observation has yet been made. The present limit on the mass difference $\Delta m_s$ is $\Delta m_s > 12.4$ ps$^{-1}$ (at 95 % C.L., from LEP, SLD and CDF), the expected value is in the Standard Model is below 20 ps$^{-1}$ (also at 95 % C.L.).

The reconstruction of $B_s$ decays uses the channel $B_s \to D_s^- \pi^+$, where the $D_s^-$ decays to $\phi\pi^-$ and the $\phi$ is detected via the $K^+K^-$ decay mode. The resolution on the proper decay time of the $B_s$ is found to be 0.071 ps, yielding a reach in $\Delta m_s$ of up to 38.5 ps$^{-1}$ (for 30 fb$^{-1}$).

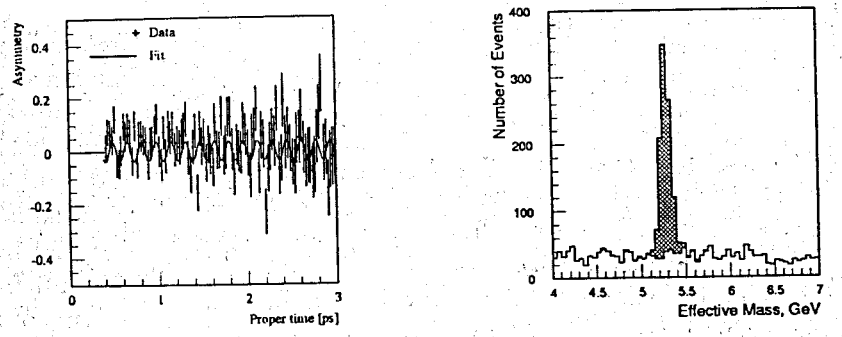


*Figure 10. Expected oscillation signature for $B_s$ mesons with $\Delta m_s = 38.5$ ps$^{-1}$ (left) and expected signal (shaded histogram) and background for the rare decay $B_d^0 \to K^{0*}\mu^+\mu^-$ (right).*

The left part of figure 10 shows the expected result in the time dependent asymmetry of a single experiment (for $\Delta m_s = 38.5$ ps$^{-1}$ and 30 fb$^{-1}$). The expected accuracy on $\Delta m_s$ itself ranges between 0.04 and 0.16 ps$^{-1}$.

### 6.3. Rare $B$ meson decays

Due to their signature with two muons in the final state, rare $B$ meson decays are considered to be 'self-triggering'. The expected branching ratios are in the range between $10^{-5}$ and $10^{-10}$ in the Standard Model. The right

part of figure 10 shows the expected signal for the decay $B_d^0 \to K^{0*}\mu^+\mu^-$, where a clear signal can be observed for 30 fb$^{-1}$.

### 6.4. Summary

Due to the high statistics of $b\bar{b}$ events ($\approx 2 \cdot 10^{10}$ per year selected by the first level trigger at low luminosity) precise measurements of the CP violation parameters $\sin 2\beta$ (expected accuracy of 0.01 (stat.)) and of the angle $\alpha$ (accuracy of down to 2°) can be made by ATLAS. Oscillations of $B_s$ mesons will be detected for mass differences up to $\Delta m_s = 38.5$ ps$^{-1}$. Furthermore the rare decay of the $B_s$ meson to two muons should be discovered with a significance of $4.3\sigma$, the one of the $B_d$ meson can be excluded down to a branching ratio of $3 \cdot 10^{-10}$ (assuming an integrated luminosity of 130 fb$^{-1}$).

## 7. Higgs bosons

### 7.1. Standard Model Higgs boson

Despite the success of the Standard Model in describing a large variety of precision measurements of electroweak processes, no experimental evidence for the Higgs mechanism as the source of electroweak symmetry breaking has yet been obtained. In its simplest form, one scalar doublet field is required. Three of the four components couple to the $W^{\pm}$ and $Z$ bosons to provide their longitudinal degree of freedom, leaving one physical field: the Higgs boson. The present limit on the Higgs mass as obtained from direct searches at LEP2 is $m_H > 95.2$ GeV (at 95 % C.L.) [3]. Results from a fit to precision electroweak data provide an indirect determination of the Higgs mass with $m_H = 92^{+78}_{-45}$ GeV, giving an upper limit of $m_H < 245$ GeV at 95 % C.L. [3]. Unitarity arguments lead to a theoretical upper bound of 1 TeV on the Higgs mass.

The dominant production mechanism for the Standard Model (SM) Higgs boson at LHC energies is gluon-gluon fusion, which proceeds via a heavy quark triangle loop. For larger masses, the $WW$ fusion process starts to contribute significantly.

For masses of the SM Higgs boson below 150 GeV, the dominant decay modes are to $b\bar{b}$ (BR $\approx$ 90 %) and to $\tau\tau$ (BR $\approx$ 10 %). The decay to two photons is a rare decay with a branching ratio of less than $2 \cdot 10^{-2}$. At larger masses (> 180 GeV) the decay to $WW$ (BR $\approx$ 75 %) and $ZZ$ (BR $\approx$ 20 %) dominates. The branching ratio to $t\bar{t}$ is less than 20 % above threshold.



#### 7.1.1. $H \to \gamma\gamma$

The detection of this rare decay mode of the SM Higgs boson requires an excellent mass resolution and a very good photon identification and reconstruction efficiency together with an excellent rejection power against jets.

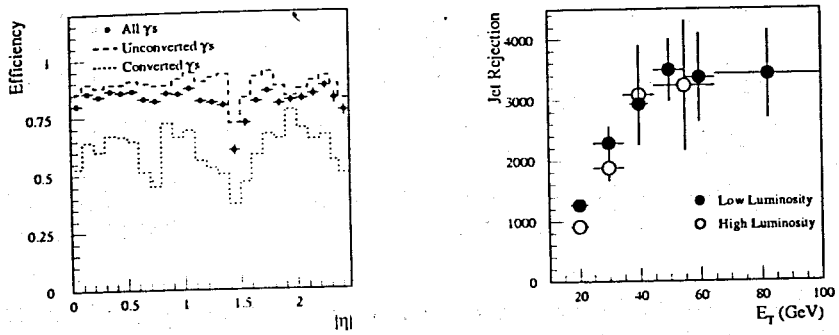


*Figure 11. Efficiency for photon reconstruction as a function of the photon pseudo-rapidity $|\eta|$ (left), and rejection against jets as a function of the transverse energy $E_T$ (right).*

Combining the detection of uncoverted photons with the 'recovery' of photons converting in the tracking volume, an overall efficiency of about 85 % has been obtained, as shown in the left part of figure 11. The probability for a conversion to occur is between 20 and 40 %. For this efficiency, a rejection larger than $3 \cdot 10^3$ against jets has been obtained (where the dominating background is the production of a leading $\pi^0$ in the jet, faking a photon signature). In the right part of figure 11, the rejection against jets obtained is shown as a function of the transvere energy.

With this performance the reducible background from $\gamma$-jet and jet-jet production contributes between 12–30 % relative to the irreducible background from photon pair production, after the photon identification selection has been applied.

The left part of figure 12 shows the expected $\gamma\gamma$ invariant mass distribution together with the signal of a Higgs boson of $m_H = 120$ GeV. The right part shows the background subtracted signal (for 100 fb$^{-1}$). The expected invariant mass resolution is $\sigma(m_{\gamma\gamma}) = 1.31$ GeV at high luminosity and improves to 1.1 GeV at low luminosity. The two dominant contributions at high luminosity are the necessity to reconstruct the vertex from

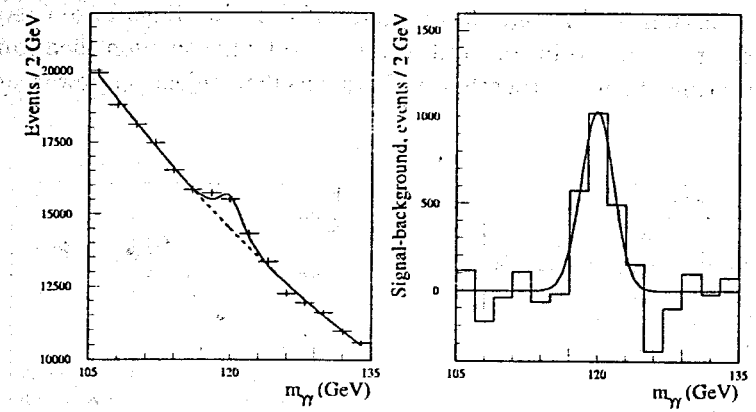


*Figure 12. $\gamma\gamma$ invariant mass distribution for the $H \to \gamma\gamma$ signal and background before (left) and after (right) background subtraction.*

the pointing information of the photon shower in the calorimeter and the contribution from pile-up events to the energy resolution.

In the evaluation of the significance for the discovery potential, direct production and associated production ($WH$, $ZH$ and $t\bar{t}H$) with the decay $H \to \gamma\gamma$ have been studied. For a Higgs mass of 120 GeV, the expected significances (defined as $S/\sqrt{B}$, where $S$ is the number of signal events and $B$ the number of background events) are 6.5 for direct production, 4.3 for associated production, where $W, Z, t\bar{t} \to leptons + X$, and 5.2 for $H + jet$ production (for an integrated luminosity of 100 fb$^{-1}$).

### 7.1.2. $t\bar{t}H \to t\bar{t}b\bar{b}$

Additional significance for small Higgs masses can be obtained from the associated production of a Higgs boson together with a $t\bar{t}$ pair. The Higgs is reconstructed via the decay $H \to b\bar{b}$. One top quark is required to decay leptonically, the other hadronically. This leads to a final state with $l\nu jjb\bar{b}b\bar{b}$.

In figure 13 two examples for the reconstructed $b\bar{b}$ mass spectrum are shown for $m_H = 100$ GeV (left) and $m_H = 120$ GeV (right), for an integrated luminosity of 100 fb$^{-1}$. The expected significances are 5 for $m_H = 100$ GeV and 3.6 for $m_H = 120$ GeV (with 30 fb$^{-1}$). This channel requires an excellent b-jet tagging capability.



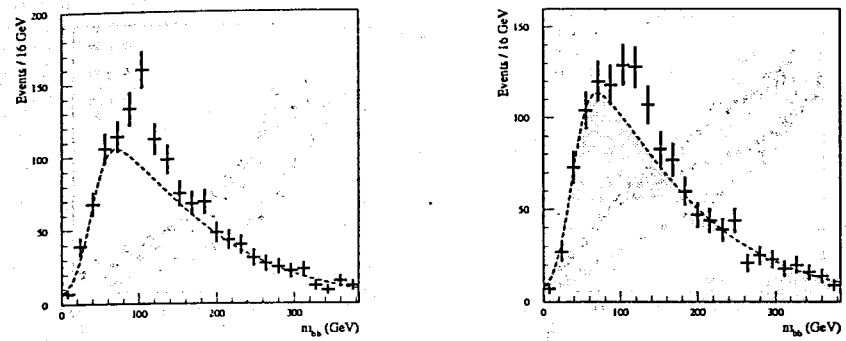


*Figure 13. Invariant mass of $b\bar{b}$ pairs from associated production of Higgs ($H \to b\bar{b}$) with $t\bar{t}$ (left part: $m_H = 100$ GeV, right part: $m_H = 120$ GeV).*

Due to the long lifetime of B hadrons ($c\tau \approx 470\mu$m), events containing a $b$ quark should exhibit displaced vertices, which can either be reconstructed directly or identified through impact parameter measurements. The latter approach has been used to obtain high efficiencies, which are shown in the left part of figure 14, together with the jet rejection for light quark ($u$), gluon ($g$) and charm ($c$) jets. For an efficiency of 60 % (at high luminosity) rejection factors of about 100 against light quark jets should be obtained; those for gluon (charm) jets are lower by a factor of about 2 (10). A further method for tagging of $b$ jets is to search for (soft) electrons (or muons) from semi-leptonic decays of the $b$ quark. The right part of figure 14 shows the expected rejection as a function of the tagging efficiency for this method.

### 7.1.3. $H \to ZZ^* \to 4l$

The selection for this channel requires a lepton pair $l^+l^-$ with an invariant mass close to the $Z$ mass and a second pair with an invariant mass above some threshold. In figure 15 the expected signal is shown for the case of a four electron (left) and a four muon (right) final state. The reconstruction efficiency is expected to be about 91 % (96 %) per lepton in case of electrons (muons). The reduction of the reducible background (mainly $t\bar{t}$ production and $Zb\bar{b}$ production) is achieved using lepton isolation and vertexing.

The significance for this channel exhibits a 'dip' between $150 < m_H < 180$ GeV due to the opening of the decay $H \to WW$.

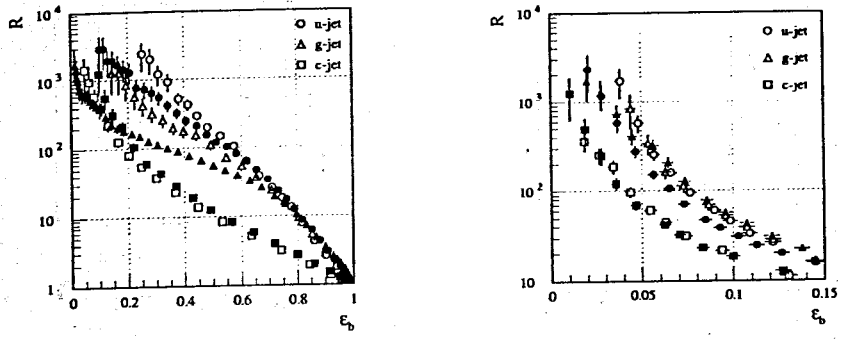


*Figure 14. Jet rejection as a function of the b-tagging efficiency for tagging based on vertexing (left) and on electron tags (right). In both figures open symbols are for $m_H = 100$ GeV, full symbols are for $m_H = 400$ GeV.*

### 7.1.4. $H \to ZZ \to 4l$

Figure 16 shows the expected invariant mass distribution of four lepton final states (two pairs of opposite sign and same flavour leptons) with a clear signal from a Higgs of 300 GeV above the background from $ZZ$ continuum production (shown for 10 fb$^{-1}$). The significance of the signal can be further increased by a cut on the transverse momentum of one of the $Z$ bosons, as shown in the right part of the same figure. The $p_T$ distribution of $Z$ bosons from the Higgs decay is expected to be harder than in the case of continuum production. However the effect of higher order corrections on the $p_T$ distribution needs to be studied further. The expected significance for 30 fb$^{-1}$ is more than 15 for $200 < m_H < 400$ GeV and has a value of 5.9 at $m_H = 600$ GeV.

### 7.1.5. $H \to WW \to l\nu jj$ for large Higgs masses

For large Higgs boson masses, the decay $H \to WW \to l\nu jj$ gives a larger rate and allows the full mass reconstruction. The left part of figure 17 shows the expected signal and background for the case of $m_H = 300$ GeV (and 30 fb$^{-1}$), the right part the case of $m_H = 600$ GeV (and 100 fb$^{-1}$). The selection includes the requirement of two forward jets (at $|\eta| > 2$), to enhance the signal production process ($WW$ and $ZZ$ fusion), and no additional jets (besides the ones from $W \to jj$) in the central region. For the case of $m_H = 600$ GeV, the significance is expected to reach values of up to 13.



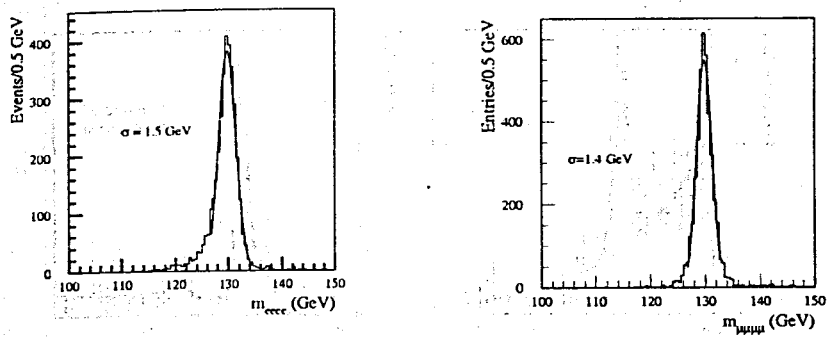


*Figure 15. Four lepton invariant mass distribution for $H \to ZZ^* \to 4l$ (left: $m_{eeee}$, right: $m_{\mu\mu\mu\mu}$).*

### 7.1.6. Discovery reach

In the evaluation of the discovery reach, no K-factors (ratio of the cross-section at next-to-leading order to the one at leading order) have been used, neither for the signal process nor for background processes. This approach is a conservative one, as long as the following relation holds: $K_{signal} > \sqrt{K_{background}}$.

Besides the channels mentioned above, also the decay $H \to WW^{(*)} \to l\nu l\nu$ has been studied for the intermediate mass range between 140 and 180 GeV, which does not allow a direct mass reconstruction. For large Higgs masses, the decay modes $H \to ZZ \to ll\nu\nu$ was also considered. The resulting coverage for Higgs masses from 80 GeV to 1 TeV is shown in figure 18, for 100 fb$^{-1}$. As can be seen from this figure, the full mass range for the SM Higgs boson is covered with more than one channel for most masses. In addition, each channel on its own has a significance of more than $5\sigma$.

## 7.2. MSSM Higgs boson

In the Minimal Supersymmetric Standard Model (MSSM), there are five physical Higgs bosons (at least two Higgs doublet fields): three neutral ones ($h$, $H$: CP even and $A$: CP odd) and two charged ones ($H^{\pm}$). The masses and decay branching ratios are determined at tree level by two parameters, which are usually chosen to be: $m_A$ (the mass of the CP odd neutral Higgs) and $\tan\beta$ (the ratio of the vacuum expectation values of the two Higgs doublets).

Assuming that SUSY particles are too heavy to appear in the decays of

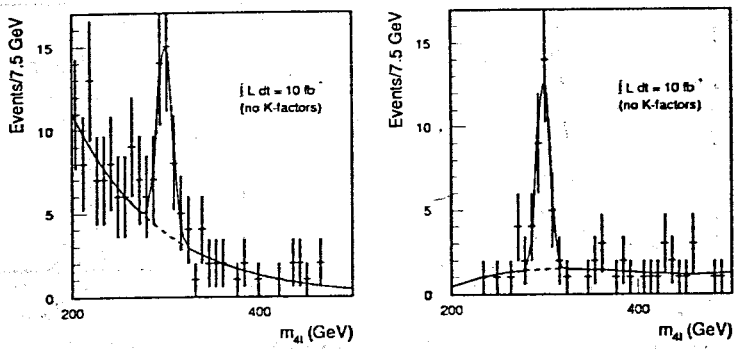


*Figure 16. Four lepton invariant mass distribution with signal of $H \to ZZ \to 4l$ (left: no $p_T^Z$ cut, right: with $p_T^Z$ cut) and background.*

the Higgs bosons, the decay modes are similar to the ones of the SM Higgs and many of the results obtained can easily be converted into discovery limits in terms of $m_A$ and $\tan\beta$. However for certain regions in the parameter space additional decay modes become relevant, some of these are discussed in the following.

### 7.2.1. Decay modes similar to SM Higgs

The values of $m_A$ and $\tan\beta$ influence the production cross-section and the branching ratios for the MSSM Higgs bosons. In figure 19 two examples of the discovery reach (at $5\sigma$) in the ($m_A$,$\tan\beta$) plane are given for the $h$ boson with the decay to $\gamma\gamma$ (left part) or $b\bar{b}$ (right part). The left part also shows the expected $5\sigma$ significance contour for $A \to \gamma\gamma$. From $h \to \gamma\gamma$, the full range in $\tan\beta$ is covered for $m_A > 270$ GeV and 100 fb$^{-1}$. For the same integrated luminosity, the decay $h \to b\bar{b}$ covers all $\tan\beta$ for $m_A > 160$ GeV.

### 7.2.2. $A \to \tau\tau$

For large values of $\tan\beta$ the largest sensitivity can be obtained from $A$ production with the decay $A \to \tau\tau$. The selection requires one leptonic $\tau$ decay and one hadronic $\tau$ decay. The associated production of $b\bar{b}H$ ($b\bar{b}A$) with $A \to \tau\tau$ has also been investigated.

The left part of figure 20 shows the invariant mass distribution of $\tau$ pairs for three values of the mass of the CP odd Higgs boson $A$ ($m_A = 150, 300, 450$ GeV and $\tan\beta = 25$) together with the expected background contribution, which is dominated by $W + jet$ production.



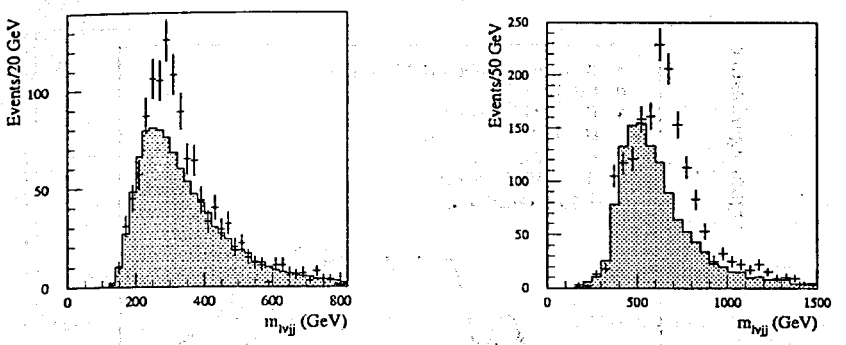


*Figure 17. Invariant mass distribution of $l\nu jj$ final states for signal ($H \to WW$) and background with $m_H = 300$ GeV (left) and $m_H = 600$ GeV (right).*

In the right part of figure 20 the expected jet rejection is shown as a function of the tau identification efficiency for various $p_T$ ranges. The $\tau$ identification efficiency increases (for constant jet rejection) with increasing $p_T$. The selection criteria are based on the shape of the shower in the calorimeter and on the number of tracks matching to the shower.

### 7.2.3. $A \to \mu\mu$

For large values of $\tan\beta$ the decay of $A$ to two muons can be observed. In figure 21 (left part) the expected signal is shown for $\tan\beta = 30$ and $m_A = 300$ GeV, assuming 30 fb$^{-1}$. The shaded histogram indicates the background from $t\bar{t}$ production. The open histogram is the total background, which is dominated by Drell-Yan muon pair production.

### 7.2.4. $A \to t\bar{t}$

For values of $\tan\beta \approx 1$, the branching ratio of $A$ and $H$ to $t\bar{t}$ is close to 100 % above the threshold $m_A, m_H > 2m_t$. In figure 21 (right part) the invariant mass distribution of $t\bar{t}$ pairs is shown, with a signal from the decay $A \to t\bar{t}$ for $m_A = 370$ GeV, $\tan\beta = 1.5$ and 30 fb$^{-1}$. It has been obtained via the decay $A \to t\bar{t} \to W(jj)W(l\nu)b\bar{b}$, requiring the full reconstruction of both $t$ quark decays. For this value of $m_A$, a significance of 8.2 is obtained.

For Higgs masses larger than 500 GeV, the observability (w.r.t. the $t\bar{t}$ continuum) is suppressed due to interferences between the signal and background amplitudes.

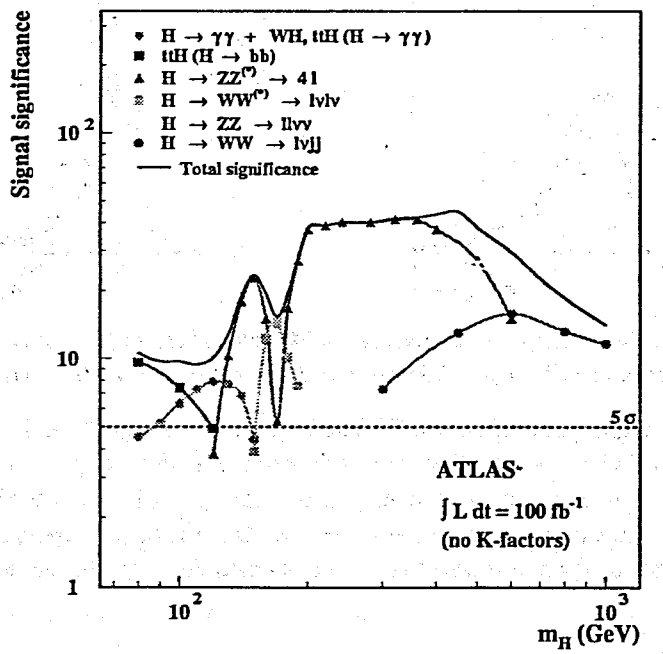


*Figure 18. Expected significance for the SM Higgs boson.*

### 7.2.5. $H \to hh$ with $h \to b\bar{b}$

The observation of this channel would imply the simultaneous discovery of two Higgs bosons. The challenge is to detect a final state with four $b$-quark jets having relatively low transverse momenta. The present $p_T$ thresholds at the second level trigger are much higher than desirable for the offline analysis. The use of a $b$-tagging algorithm at this trigger level could allow for lower tresholds, while keeping the output rate reasonably low.

In the left part of figure 22 the reconstructed invariant mass of a $b\bar{b}$ pair is shown (for $m_h = 80$ GeV), the right part of this figure shows the $b\bar{b}b\bar{b}$ invariant mass (for $m_H = 300$ GeV).

### 7.2.6. $H^+ \to cs$

In case the charged Higgs is lighter than the top quark, it can be produced in the decay of the top ($t \to H^+b$). The search for the $H^+$ can be done via $t\bar{t}$ production with the decay to $H^+(cs)bW(l\nu)\bar{b}$. Selection



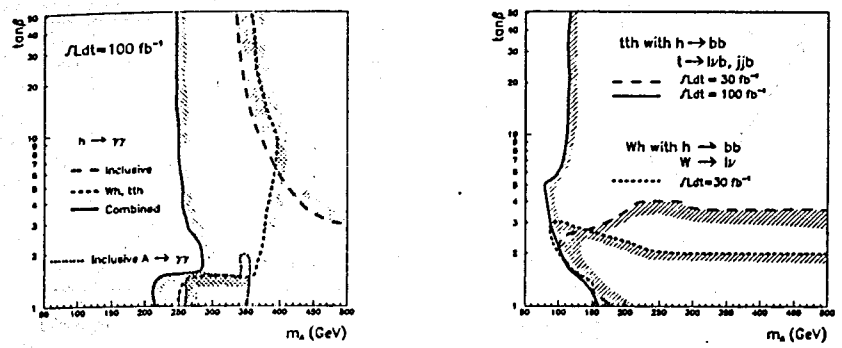


*Figure 19. $5\sigma$ discovery contours in the ($m_A$,$\tan\beta$) plane for the decay $h \to \gamma\gamma$ and $A \to \gamma\gamma$ (left) and for $h \to b\bar{b}$ (right).*

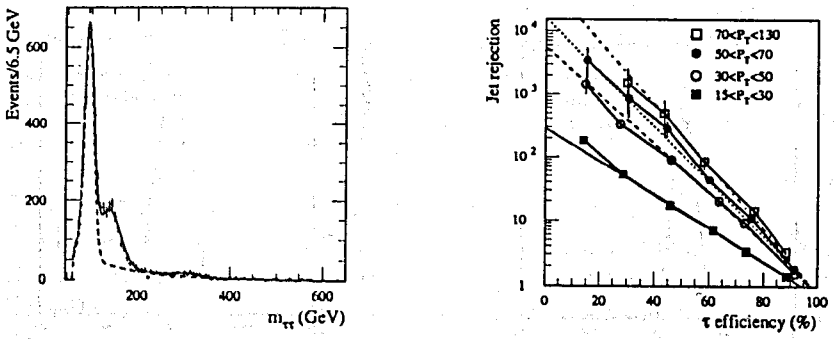


*Figure 20. Tau pair invariant mass distribution with signals for three cases of $A \to \tau\tau$ (left) and jet rejection as a function of the tau efficiency (right).*

requirements include one isolated lepton, two b-tagged jets and two non b-tagged jets, whose invariant mass is searched for a mass peak. Figure 23 shows in the left part the expected signal and background distribution for the case of $m_{H^+} = 130$ GeV and $\tan\beta = 1.5$, where a significance of 4.4 is obtained for 30 fb$^{-1}$.

### 7.2.7. $H^+ \to tb$

If the charged Higgs is heavier than the top quark, it can decay to $tb$. In the right part of figure 23 the distribution of signal and background in the invariant mass of $tb$ is shown for $m_{H^+} = 300$ GeV and $\tan\beta = 1.5$, with a significance of 9.2 obtained for 30 fb$^{-1}$. The selection requires several

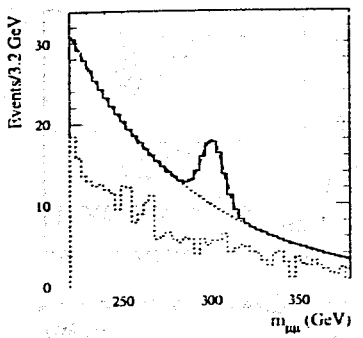


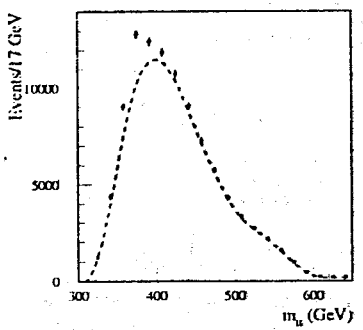


*Figure 21. Dimuon invariant mass distribution for $H/A \to \mu\mu$ and background (left) and $t\bar{t}$ invariant mass distribution with signal from $A \to t\bar{t}$ (right).*

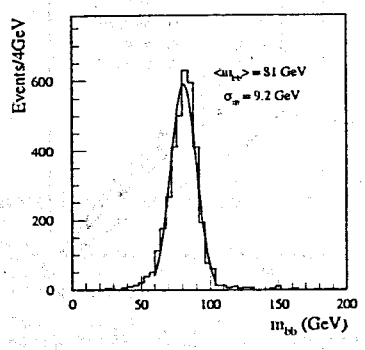


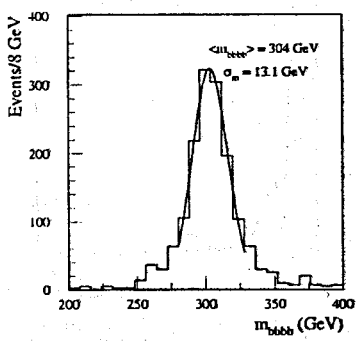


*Figure 22. Reconstructed spectra for $H \to hh$ with $h \to b\bar{b}$. The left part shows $m_{b\bar{b}}$, the right part $m_{b\bar{b}b\bar{b}}$.*

$b$-tagged jets in the final state and at least one reconstructed top quark.

### 7.2.8. Discovery reach

Figure 24 shows the discovery reach ($> 5\sigma$) in the $m_A$ – $\tan\beta$ parameter space for the case of minimal mixing in the stop sector and an integrated luminosity of 300 fb$^{-1}$. The full parameter space is covered and in most cases it should also be possible to distinguish between a SM Higgs and a MSSM Higgs. In addition the expected limits from LEP2 for this scenario are indicated.



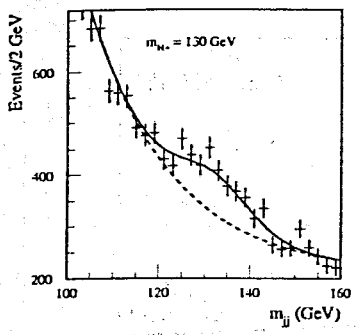


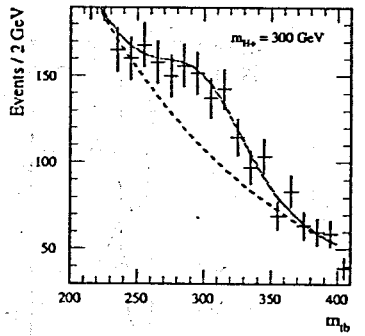


*Figure 23. Reconstructed mass of charged Higgs bosons with decay to cs (left, $m_{H^+} = 130$ GeV) and to tb (right, $m_{H^+} = 300$ GeV). The background is also shown (dashed line).*

## 7.3. Measurement of parameters

Once one (or more) Higgs bosons have been observed, these events will be used to determine the properties (e.g. mass, width, $BR{\cdot}\sigma$) of the Higgs. Combining several decay channels and/or production modes will allow to put constraints on the Higgs couplings. All the numbers given below are based on an integrated luminosity of 300 fb$^{-1}$.

### 7.3.1. Standard Model Higgs boson

The left part of figure 25 shows the expected accuracy on the mass of the SM Higgs, reaching a precision of about $10^{-3}$ for $m_H < 500$ GeV. This accuracy is given by the channels $H \to \gamma\gamma$ and $H \to ZZ \to 4l$. The right part of figure 25 shows the expected accuracy on the width of the Higgs boson. This is expected to be measured to better than $7 \cdot 10^{-2}$ for $m_H < 700$ GeV from the decay $H \to ZZ \to 4l$. A direct width measurement will only be possible for masses larger than 200 GeV, as below this value the natural width of the Higgs is smaller than the experimental mass resolution for Higgs masses.

### 7.3.2. MSSM Higgs bosons

In the left part of figure 26 the expected accuracy on the measurement of the MSSM Higgs masses (for $\tan\beta = 30$) is shown as a function of $m_A$. The mass of the $H$ and $A$ boson should be measured to about 10 % for $m_A > 200$ GeV and that of the $h$ boson to about 1 % for $m_A > 300$ GeV. The right part shows the expected accuracy on $\tan\beta$. It should be possible to reach an accuracy of better than 10 % for $\tan\beta > 7$ from $H/A \to \tau\tau$.

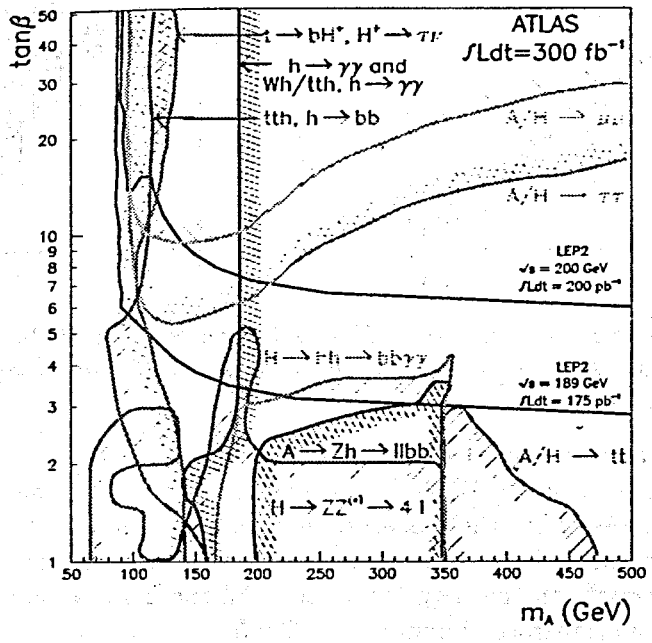


*Figure 24. Discovery reach for the MSSM Higgs boson (for minimal mixing).*

and similar for $\tan\beta > 10$ from $H/A \to \mu\mu$.

### 7.4. Summary

If a Standard Model Higgs boson does exist, it will be discovered by ATLAS after a few years of data taking at low luminosity (for masses from LEP2 limits up to 1 TeV). For most masses, at least two channels can be used. Properties of the Higgs boson can be measured precisely and constraints be put on the couplings.

In case of the MSSM Higgs bosons, the full parameter space will be covered for an integrated luminosity of 100 fb$^{-1}$ and in most cases a distinction between a SM and a MSSM Higgs is possible (if the SUSY mass scale is large and no SUSY particles appear in the Higgs decay). Higgs parameters can be determined also in the MSSM case.



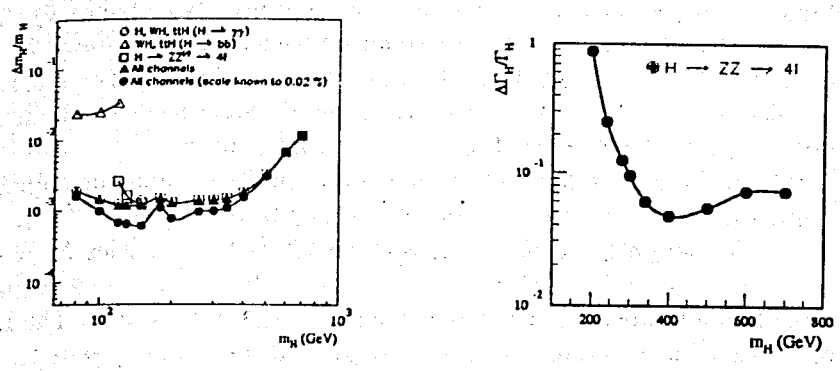


*Figure 25. Expected precision on the SM Higgs mass (left) and width (right).*

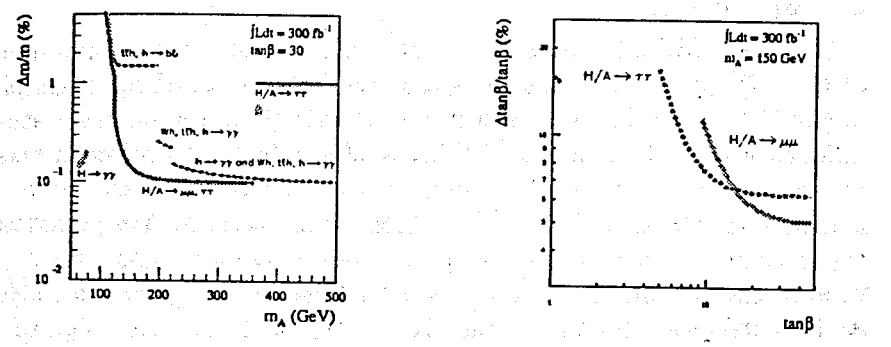


*Figure 26. Expected precision on the measurement of MSSM Higgs masses (left) and $\tan\beta$ (right).*

## 8. Supersymmetry

Supersymmetry proposes an elegant solution to the hierarchy problem, avoiding the necessary fine tuning to cancel divergences in loop corrections to the Higgs mass. Indications for supersymmetry can be obtained from the unification of the three gauge couplings at the GUT scale, which fails in the Standard Model and succeeds in SUSY.

In the Minimial Supersymmetric Standard Model, there is one additional particle for each particle of the Standard Model. There are at least two Higgs doublet fields, yielding five physical Higgs bosons (as mentioned in section 7.2). The SUSY partners of the quarks are the squarks $\tilde{q}$ (spin 0, left- and right-handed), the one of the gluon is the gluino $\tilde{g}$ (spin $\frac{1}{2}$) and

the ones of the leptons (neutrinos) are the sleptons $\tilde{l}$ (sneutrinos $\tilde{\nu}$). The partners of the $W^{\pm}$ and the $H^{\pm}$ mix to form the charginos $\tilde{\chi}_i^{\pm}(i = 1, 2)$, the ones of the $\gamma$, $Z$, $h$, $H$ and $A$ mix to form the neutralinos $\tilde{\chi}_i^0(i = 1, \ldots, 4)$. Since SUSY has to be broken, the most general model leads to about 100 additional parameters describing the soft breaking terms.

Based on the baryon number $B$, the lepton number $L$ and the spin $S$, a new quantum number (R-parity) can be defined as $R_p = (-1)^{3B+L+2S}$. For Standard Model particles $R_p = +1$, whereas for SUSY particles $R_p = -1$. If R-parity is conserved, SUSY particles can only be produced in pairs and the lightest supersymmetric particle (LSP) has to be stable. The LSP is also weakly interacting (for cosmological reasons), which leads to the characteristic signature of large missing transverse energy, as there are at least two LSP's per event.

## 8.1. SUGRA scenarios

To obtain MSSM models with fewer parameters, the assumption of SUGRA (Supergravity) models is that the breaking of SUSY takes place in a hidden sector and is transmitted to the visible sector via gravitational interactions. In the minimal SUGRA model (mSUGRA) common masses for squarks, sleptons and the Higgs bosons and common masses of the gauginos are assumed at the GUT scale. Thus there are five parameters: $m_0$ (a common scalar mass), $m_{1/2}$ (a common fermion mass), $\tan\beta$ (the ratio of the vacuum expectation values of the two Higgs doublet fields), $A_0$ (the trilinear coupling at the GUT scale) and $\mathrm{sgn}\mu$ (the sign of the Higgsino mass parameter).

The actual values of SUSY particle masses (e.g. at the weak scale) are determined by a set of renormalization group equations, which evolve the two common masses $m_0$ and $m_{1/2}$ from the GUT scale to a lower scale. In general the masses of the neutralinos and the gauginos are proportional to $m_{1/2}$, whereas the masses of the squarks, sleptons and sneutrinos are proportional to $\sqrt{m_0^2 + f \cdot m_{1/2}^2}$, with $0.1 < f < 6$.

### 8.1.1. Description of models used

Six points in the mSUGRA parameter space were chosen for detailed studies: points 1 and 2 lead to large squark and gluino masses, point 3 is chosen for comparison with existing accelerators (these should be able to discover this point), point 4 exhibits a strong mixing between gauginos and Higgsinos. Point 5 is motivated by cosmology, as the cold dark matter density due to the LSP is close to the critical one. Finally, point 6 has a large value of $\tan\beta$.

| point | $m_0$ | $m_{1/2}$ | $A_0$ | $\tan\beta$ | $\mathrm{sgn}\mu$ |
|---|---|---|---|---|---|
| 1 | 400 GeV | 400 GeV | 0 | 2 | + |
| 2 | 400 GeV | 400 GeV | 0 | 10 | + |
| 3 | 200 GeV | 100 GeV | 0 | 2 | − |
| 4 | 800 GeV | 200 GeV | 0 | 10 | + |
| 5 | 100 GeV | 300 GeV | 300 GeV. | 2.1 | + |
| 6 | 200 GeV | 200 GeV | 0 | 45 | − |

*Table 1. Parameters of the six mSUGRA models studied.*

In table 1 the values of the five parameters describing the different mSUGRA models are summarized.

### 8.1.2. Discovery reach for mSUGRA scenarios

In figure 27 the discovery reach ($5\sigma$) is shown for various inclusive signatures:

**0l** no leptons, but jets and missing $E_T$,

**1l** one lepton plus jets and missing $E_T$,

**SS** two leptons of the same sign,

**OS** two leptons of opposite sign,

**3l** three leptons plus jets and missing $E_T$,

**2l,0j** two leptons and missing $E_T$, but no jets,

**3l,0j** three leptons and missing $E_T$, but no jets.

Four parameter settings have been used: $\tan\beta = 2$ or $\tan\beta = 10$ and $\mu < 0$ or $\mu > 0$. The reach for discovery from the inclusive signatures extends up to masses between 1 and 2 TeV. Also shown are the locations of the first five mSUGRA points.

An important experimental aspect is the minimisation of fake $E_T^{miss}$ tails. The signature of large missing $E_T$ could be faked by badly measured jets. For $E_T^{miss} > 200$ GeV, a rejection factor of 1000 or more is needed. Figure 28 (left part) compares the $E_T^{miss}$ distribution for fully simulated $Z + jet$ events (dashed line) to the case, where the jet is undetected (full line).

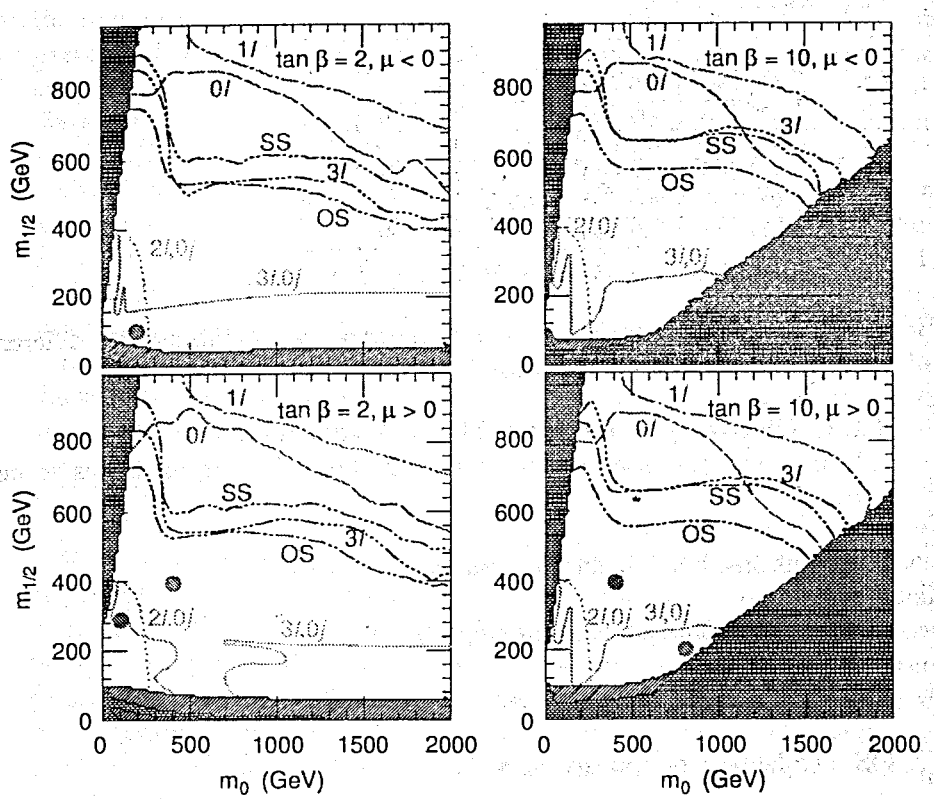


*Figure 27. Discovery reach in the $m_0 - m_{1/2}$ plane for various inclusive signatures (for 10 $fb^{-1}$).*

### 8.1.3. Exclusive measurements

Once a discovery has been made, the next steps are to get information about the mass scale of SUSY and to try to reconstruct decay cascades to obtain further constraints on the fundamental parameters of the theory.

In figure 28 (right part) the distribution in the effective mass $M_{eff} = E_T^{miss} + p_{T,1} + p_{T,2} + p_{T,3} + p_{T,4}$ is shown, where $p_{T,i}$ are the transverse momenta of the four leading jets. As an example, mSUGRA point 5 has been used. A clear excess of events is observed for effective masses above 1 TeV. The different contributions to the background are: $t\bar{t}$ production (closed circles), $W + jet$ production (triangles), $Z + jet$ production (downward triangles) and QCD jet production (squares).

The result of a scan of the mSUGRA parameter space is shown in the



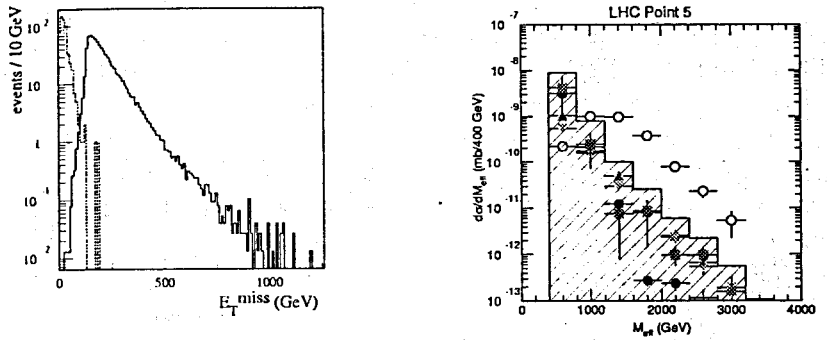


*Figure 28. Expected tails in the $E_T^{miss}$ distribution (left) and distribution of the effective mass $M_{eff}$ for mSUGRA point 5 (right).*

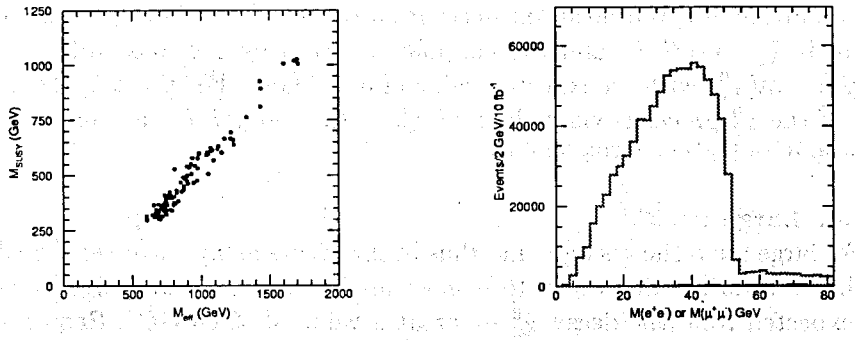


*Figure 29. Correlation between $M_{eff}$ and $M_{SUSY}$ for mSUGRA point 5 (left) and dilepton mass distribution for mSUGRA point 3 (right).*

left part of figure 29. A clear correlation between the observed onset of the deviation from Standard Model background in the $M_{eff}$ distribution and the value $M_{SUSY} = \min(M_{\tilde{g}}, M_{\tilde{q}})$ is observed.

Due to the appearance of two LSP's escaping detection for each event, a direct reconstruction of mass peaks for SUSY particles is not possible. However, endpoints in the distributions of invariant masses of the visible decay products can be used to constrain e.g. mass differences between different SUSY particles.

In figure 29 (right) and figure 30 (left) two examples for the expected distribution of the dilepton invariant mass are given for point 3 and point 5. The background from the Standard Model is in both cases hardly

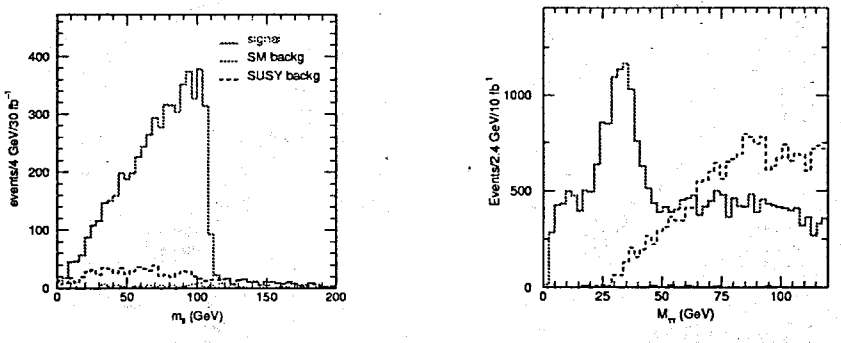


*Figure 30. Dilepton mass distribution for mSUGRA point 5 (left) and Invariant mass of tau pairs for point 6 (right).*

visible, and for point 5 there is some contribution from other SUSY decay cascades (dashed histogram). In both mSUGRA points, clear endpoints in the dilepton invariant mass are observed. For point 3, the decay chain is $\tilde{\chi}_2^0 \rightarrow \tilde{\chi}_1^0 l^+ l^-$ and the endpoint is given by the mass difference $m(\tilde{\chi}_2^0) - m(\tilde{\chi}_1^0)$ with an expected value of 52.47 GeV. For point 5, the decay of the $\tilde{\chi}_2^0$ proceeds via a slepton: $\tilde{\chi}_2^0 \rightarrow \tilde{l}_R^+ l^- \rightarrow \tilde{\chi}_1^0 l^+ l^-$, leading to an expected endpoint at 108.93 GeV.

### 8.1.4. Large $\tan\beta$

For large $\tan\beta$ the $\tilde{t}$ is light and thus in the events many $\tau$'s are expected. If the $\tau\tau$ invariant mass were to be measured directly, a sharp edge would be expected from the decay $\tilde{\chi}_2^0 \rightarrow \tilde{\tau}\tau$ at a value of 59.64 GeV. Requiring both tau's to decay hadronically, the expected invariant mass distribution is shown in the right part of figure 30. The dotted line indicates real $\tau\tau$ pairs, the dashed line shows pairs with one fake $\tau$. The smearing and the shift of the edge are due to the undetected neutrinos.

## 8.2. Gauge mediated Supersymmetry breaking

In contrast to SUGRA scenarios, where the breaking of SUSY occurs at a very large scale and is mediated by gravity, in Gauge Mediated Supersymmetry Breaking models (GMSB) the breaking occurs at a messenger scale much smaller than the Planck scale and is transmitted to the 'real world' via gauge interactions. The LSP is the gravitino $\tilde{G}$ with a mass that can be much smaller than 1 GeV. The next lightest supersymmetric particle (NLSP) can either be the $\tilde{\chi}_1^0$ (decaying to $\tilde{G}\gamma$) or the $\tilde{l}_R$ (decaying to $\tilde{G}l$).



### 8.2.1. Description of model parameters

The parameters describing the GMSB models are: $\tan\beta$, sgn$\mu$, $M_m$ (the messenger scale), $\Lambda = F/M_m$ (where $\sqrt{F}$ is the SUSY breaking scale), $N_5$ (the number of equivalent $5+5$ messenger fields) and $C_{grav}$ (the scale factor for the gravitino mass). The latter parameter influences directly the lifetime of the NLSP, which can either decay close to the interaction point (leading to signatures with missing $E_T$) or be quasi-stable. In table 2 the

| point | $\tan\beta$ | sgn$\mu$ | $\Lambda$ (TeV) | $M_m$ (GeV) | $N_5$ | $C_{grav}$ | NLSP | $(c\tau)_{NLSP}$ |
|---|---|---|---|---|---|---|---|---|
| 1a | 5 | + | 90 | 500 | 1 | 1 | $\tilde{\chi}_1^0$ | 1.2 mm |
| 1b | 5 | + | 90 | 500 | 1 | $10^3$ | $\tilde{\chi}_1^0$ | 1.1 km |
| 2a | 5 | + | 30 | 250 | 3 | 1 | $\tilde{\tau}_1$ | 52 $\mu$m |
| 2b | 5 | + | 30 | 250 | 3 | $5 \cdot 10^3$ | $\tilde{\tau}_1$ | 1 km |

*Table 2. Parameters of the four GMSB models.*

values of the six parameters describing the four different GMSB scenarios used are summarized. Also indicated is the NLSP and its lifetime.

### 8.2.2. GMSB point 1a

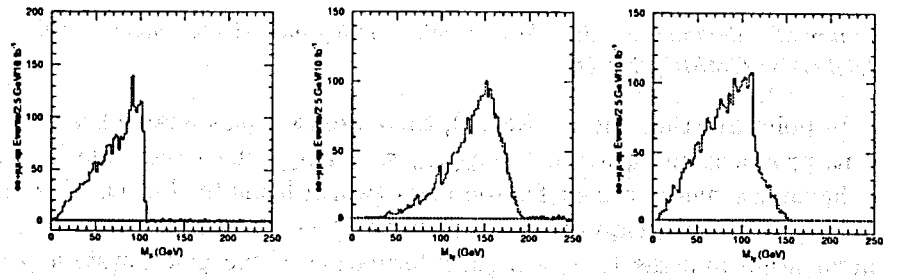

*Figure 31. Flavour subtracted mass distributions for GMSB point 1a of $M_{l^+l^-}$ (left), $M_{l^+l^-\gamma}$ (middle) and $M_{l^\pm\gamma}$ (right).*

In GMSB point 1a, the lifetime of the NLSP (which is the $\tilde{\chi}_1^0$, decaying to $\tilde{G}\gamma$) has a value of $c\tau \approx 1$ mm. In the decay $\tilde{\chi}_2^0 \rightarrow \tilde{l}_R^+ l^- \rightarrow \tilde{\chi}_1^0 l^+ l^- \rightarrow \tilde{G}\gamma l^+ l^-$ four endpoints are expected in the invariant mass distributions of $M_{l^+l^-}$ (at 105.1 GeV), $M_{l^+l^-\gamma}$ (at 189.7 GeV) and $M_{l^\pm\gamma}$ (at 112.7 GeV for the right combination and at 152.6 GeV for the wrong combination). Figure 31 shows these three invariant mass distributions. The leptons $l^+l^-$ must be correlated in flavour, as GMSB models converse flavour. Thus the flavour subtracted mass distributions are shown for dileptons ($e^+e^- + \mu^+\mu^- - e^\pm\mu^\mp$). This removes SUSY and Standard Model background with

two independent lepton decays. The four endpoints mentioned are clearly visible and constrain three masses. Furthermore, after a reconstruction of the $\tilde{G}$ momentum (which is obtained from a $0C$ fit using the three mass constraints in the $\tilde{\chi}_2^0$ decay and resolving two-fold ambiguities through double occurence of the decay in an event), the decays of squarks and gluinos can also be reconstructed in the decay chain $\tilde{q} \to \tilde{g}q \to \tilde{\chi}_2^0 \bar{q}qq$.

### 8.2.3. GMSB point 2b

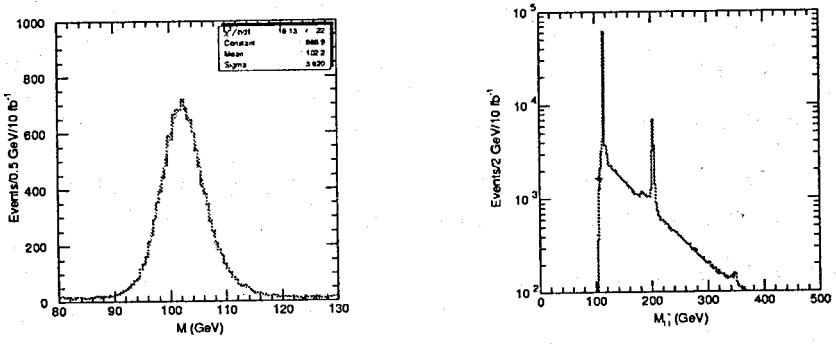


*Figure 32. Slepton mass distribution (left) and lepton – slepton mass distribution (right) for GMSB point 2b.*

In point 2b (the $\tilde{\tau}_1$ is the NSLP), there are two quasi-stable heavy sleptons produced in each event ($c\tau_{slepton} \approx 1$ km), which resemble in their behaviour a muon, except for the mass (which leads to $\beta < 1$). They are produced in the decays of the neutralinos $\tilde{\chi}_i^0 \to \tilde{l}_R^+ l^-$. Using the measured momentum and the time-of-flight information of the muon system (time resolution of $\sigma \approx 0.65$ ns) for the determination of the velocity, the mass of the slepton can be reconstructed. Figure 32 (left part) shows the expected mass distribution obtained from the timing and momentum measurement. Combining the measured slepton with a lepton allows to reconstruct the decays of the neutralinos. In the right part of figure 32 the invariant mass of the slepton-lepton system is shown; clear signals from the $\tilde{\chi}_1^0$, $\tilde{\chi}_2^0$ and $\tilde{\chi}_4^0$ decays are visible.

## 8.3. R-parity violation

If R-parity is not conserved, the signatures for events containing supersymmetric particles change. In the case of baryon number violation, a large number of jets (on average 12) are expected, without significant



missing transverse energy associated to the event. If the lepton number is violated, additional leptons and jets are expected together with missing transverse energy.

### 8.3.1. Baryon number violation via $\tilde{\chi}_1^0 \to qqq$

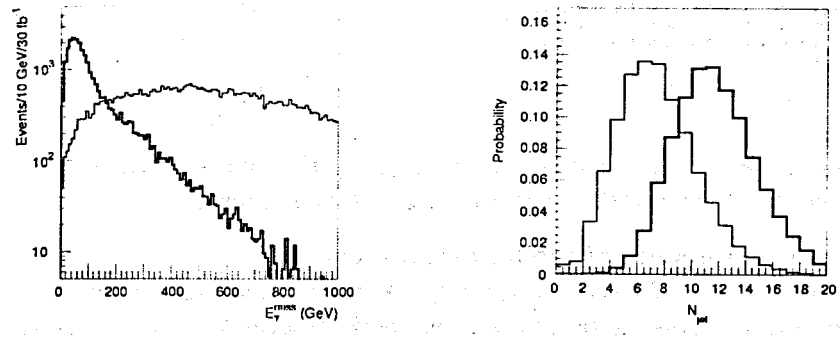


*Figure 33. Distribution of the missing transverse energy $E_T^{miss}$ (left) and of the number $N_{jet}$ of jets (right), comparing $R_p$-violating SUSY (open histogram) to $R_p$-conserving SUSY (shaded histogram).*

In case of baryon number violation, a selection based on a large number of jets alone is not sufficient to suppress efficiently the large QCD background. By demanding at least one lepton in the final state, a better suppression of the Standard Model background is achieved. In the left part of figure 33, the expected distribution of missing transverse energy is shown both for the case of $R_p$ violating SUSY and for $R_p$ conserving supersymmetry (using in both cases the parameters of mSUGRA point 5). The missing $E_T$ signature is much reduced in case of $R_p$ violation. As shown in the right part of figure 33, there are however higher jet multiplicities in case of $R_p$ violation.

### 8.3.2. Lepton number violation via $\tilde{\chi}_1^0 \to l^+ l^- \nu$

An inclusive selection of at least three leptons and missing transverse energy allows (assuming a coupling $\lambda_{123} = 10^{-3}$) to cover a large range of the parameter space $m_0 - m_{1/2}$ with a $5\sigma$ significance, as shown in the left part of figure 34. An indication on the mass scale can be obtained from the effective mass $M_{eff} = \sum_{i=1}^{4} p_{T,i}^{jet} + \sum_{i=1}^{4} p_{T,i}^{lepton} + E_T^{miss}$, using the four leading jets and the four leading leptons. Figure 34 (right part) shows a good correlation between $M_{eff}$ and $M_{SUGRA} = \min(m_{\tilde{g}}, m_{\tilde{q}_R}, m_{\tilde{b}_1}, m_{\tilde{t}_1})$.

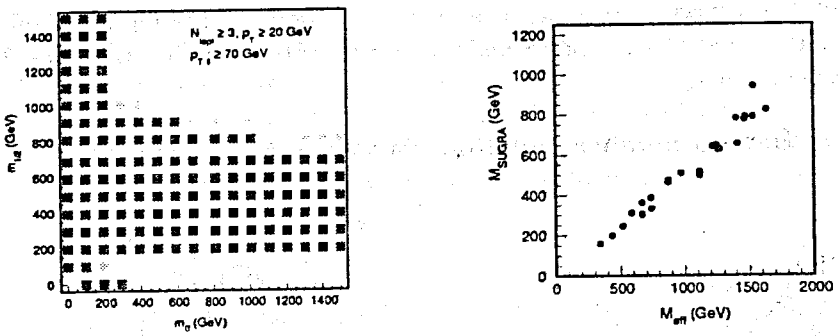


*Figure 34. $5\sigma$ reach in the $m_0 - m_{1/2}$ plane for 10 $fb^{-1}$ in case of lepton number violation (left) and correlation of $M_{SUGRA}$ with $M_{eff}$ (right).*

## 8.4. Measurements of model parameters

Using the (partial) reconstruction of the decay chains of supersymmetric particles as described above, for a given model information on the sparticle masses can be extracted. Using these constraints, a global fit is done to determine the model parameters (this is only possible if the number of parameters is limited).

An initial scan is used to find approximate regions, by weighting each point according to the experimental errors. Next, more points in these regions are scanned until the favoured values of the parameters and their $\pm 1\sigma$ errors are determined for a given integrated luminosity (either 30 $fb^{-1}$ or 300 $fb^{-1}$). Besides the statistical error, systematic uncertainties due to the knowledge of the electromagnetic, the muon and the jet energy scale are taken into account. The light Higgs mass is assumed to be known to $\Delta M_h = \pm 1$ GeV in the case of 30 $fb^{-1}$ and to $\pm 0.2$ GeV for the case of ultimate sensitivity (300 $fb^{-1}$). No errors are used for the theoretical treatment of the sparticle mass calculation.

### 8.4.1. Case of mSUGRA

For the first five mSUGRA points the expected precision is given in table 3. The numbers given correspond to an integrated luminosity of 30 $fb^{-1}$ (numbers in brackets are for the ultimate sensitivity with 300 $fb^{-1}$).

### 8.4.2. Case of GMSB

In the case of GMSB points the expected accuracy is given in table 4 (for 30 $fb^{-1}$, assuming that $m_h$ is known to 3 GeV).

Five measurements (light Higgs mass and four lepton / photon mass



| model | $\delta(m_0)$ | $\delta(m_{1/2})$ | $\delta(\tan\beta)$ |
|---|---|---|---|
| point 1 | $\pm 25(25)$ % | $\pm 2.5(2)$ % | $\pm 4(1)$ % |
| point 2 | $\pm 25(25)$ % | $\pm 2.5(2)$ % | $\pm 20(12)$ % |
| point 3 | $\pm 5(2.5)$ % | $\pm 1(1)$ % | $\pm 2.5(1)$ % |
| point 4 | $\pm 6.3(4.4)$ % | $\pm 2(0.75)$ % | $\pm 20(6)$ % |
| point 5 | $^{+4.1}_{-2.2}(1.3)$ % | $\pm 0.9(0.5)$ % | $\pm 5(2.5)$ % |

*Table 3. Expected accuracy on mSUGRA parameters for various points and for 30 $fb^{-1}$ with $\Delta M_h = \pm 1$ GeV (ultimate sensitivity with 300 $fb^{-1}$) with $\Delta M_h = \pm 0.2$ GeV.*

| model | $\delta(\Lambda)$ | $\delta(M_m)$ | $\delta(\tan\beta)$ | $\delta(N_5)$ |
|---|---|---|---|---|
| 1a | $\pm 2$ % | $\pm 34$ % | 26 % | $\pm 1.4$ % |
| 1b | $\pm 13$ % | upper limit | $^{+54}_{-36}$ % | $\pm 1$ % |
| 2a | $\pm 1.8$ % | $\pm 24$ % | $\pm 20$ % | $\pm 1.7$ % |
| 2b | $\pm 0.9$ % | $\pm 13$ % | $\pm 6$ % | $\pm 0.7$ % |

*Table 4. Expected accuracy on GMSB parameters (30 $fb^{-1}$).*

combinations) can be used to constrain the parameters. The sign of $\mu$ is determined unambigously. The values of $\Lambda$ and $N_5$ are well determined, at high luminosity the errors are dominated by systematic uncertainties. The value of $\tan\beta$ is mostly related to the Higgs mass and its accuracy is determined by the accuracy on the Higgs mass.

The value of $C_{grav}$ is independent of other parameters and will be determined from the lifetime of the NLSP.

## 8.5. Summary

The discovery of supersymmetric particles at the LHC should be easy for masses of up to 1 – 2 TeV. The decay of supersymmetric particles leads to final states containing multiple jets, leptons, heavy flavours and missing transverse energy. The exact composition of these signatures is model and parameter dependent. Studies done within different models (and for different parameter sets) have shown that it should be possible to reconstruct decay cascades (despite the fact that the LSP often escapes detection) by making use of kinematic endpoints. From this information, SUSY particle masses can be determined and thus the SUSY parameter space can be constrained.

## 9. Other searches

### 9.1. Compositeness

Assuming that quarks and leptons are not fundamental particles, but are composite objects, a spectrum of particles with unusual quantum numbers is predicted (like excited quarks and leptoquarks). Compositeness can also be searched for by using inclusive jet production, where an excess of events at the highest transverse energies would be expected in the case of compositeness. Figure 35 shows in the left part the expected relative deviation from the Standard Model expectation for three values of the compositeness scale. For an integrated luminosity of 300 fb$^{-1}$ a lower limit of 40 TeV should be reached.

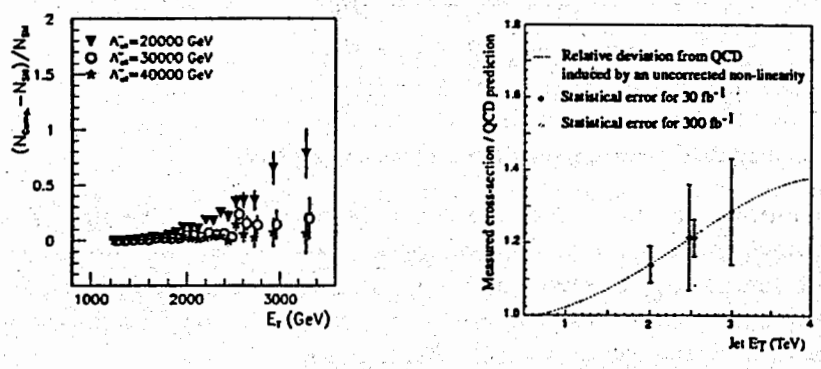


*Figure 35. Relative deviation of the inclusive jet cross-section in case of compositeness ($\Lambda = 20, 30, 40$ TeV) with respect to the one without compositeness (left) and expected deviation due to a miscalibration (right).*

This measurement is however sensitive to the exact knowledge of the jet energy scale. Not understood non-linearities could fake such a signature, and therefore the use of angular distributions provides a cross-check. The right part of figure 35 shows the expected deviation from the QCD prediction due to an uncorrected non-linearity in the calorimeter response, which is significant in comparison with the statistical uncertainties indicated.

### 9.2. Technicolor

Technicolor models invoke dynamical breaking of electroweak symmetry through the existence of 'technifermions' with technicolor charge and strong interactions at high scales. The Goldstone bosons providing the longitudinal degrees of freedom of the $W$ and $Z$ bosons are condensates of



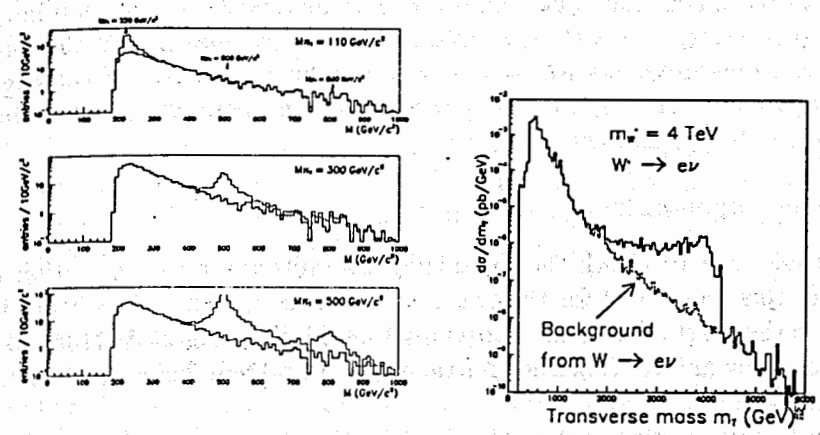


*Figure 36. $WZ$ invariant mass distribution with signal from technirho and background (left) and expected signal in the transverse $e\nu_e$ mass distribution from a heavy $W$ boson (right).*

technіquarks, the so called technipions.

Figure 36 shows in the left part the expected signal for the decay of technirho $\rho_T^{\pm}$ resonances to $W^{\pm}Z$ with a leptonic final state ($l^{\pm}\nu l^{\pm}l^{\mp}$) for various masses of the technirho and the technipion. The shaded histogram indicates the background from $WZ$ production.

### 9.3. New heavy gauge bosons

Extensions of the Standard Model gauge group give rise to new gauge bosons. Figure 36 shows in the right part the expected signal from a $W'$ boson with a mass of 4 TeV in the leptonic decay to an electron and a neutrino. In this case, $W'$ bosons should be observable up to masses of 6 GeV.

## 10. Conclusions

The ATLAS detector is well suited for discovery physics at the LHC, including the search for Higgs bosons and the search for Supersymmetry (and other new physics processes). The expected performance will not only allow discoveries to be made, but also a variety of precision measurements to be performed. Various Standard Model processes can be used to provide new information on parton densities of proton (in yet uncov-

ered kinematical regions), to yield precise measurements of the $W$ boson and the top quark mass and to measure parameters of CP violation in the $B_d$ meson system, as well as oscillations of the $B_s$ meson. Furthermore precision measurements will also be possible for parameters of the Higgs boson(s) and of supersymmetric particles, leading possibly to constraints on the model parameters.


### Acknowledgements

I would like to thank the organizing committee for the invitation to present this report and for the organization of the school at this beautiful place in the south of Belarus. Especially I would like to thank N. Shumeiko, N. Skatchkov and A. Tolkachev for their efforts and help before and during the school.

The results summarized in this contribution have been obtained from the hard work of my colleagues in ATLAS over several years and I would like to acknowledge their efforts leading to [2], which provided the basis for this report.


### REFERENCES


1. ATLAS collaboration,
   Technical Proposal, CERN/LHCC/94-43.
2. ATLAS collaboration,
   Detector and Physics Performance Technical Design Report, CERN/LHCC 99-14 (vol. I) and CERN/LHCC 99-15 (vol. II).
3. E. Gross, 'Searches for new particles', plenary talk at the Intern. Europhysics Conf. on High Energy Physics, July 1999, Tampere, Finland.




# The ATLAS Detecor at the LHC


*R. Leitner, Charles University, Prague*
*for the ATLAS Collaboration*



**Abstract**

The ATLAS experiment has now entered the construction phase for many of its detector components, with a strict schedule to meet the first collisions at the Large Hadron Collider in summer 2005. The main features of the detector are briefly summarized.


## 1 Introduction

The Large Hadron Collider (LHC) [1] is a proton-proton collider with 14 TeV centre of mass energy and design luminosity of $10^{34}$ cm$^{-2}$s$^{-1}$. Beam crossings are 25 ns apart and at design luminosity there are 23 interactions per crossing.

The ATLAS detector concept and its physics potential have been presented in the Technical Proposal[2] about four years ago. Over the last two years detailed descriptions of the detector systems and their performance have been presented in the various Technical Design Reports (TDR)[?]; the complex task of their integration into the overall ATLAS detector has been recently described in the Technical Coordination TDR[11]. The main features of the detector are briefly summarized in following sections. More details can be found in the ATLAS Detector and Physics Performance TDR[12].

## 2 Overall detector concept

A broad spectrum of detailed physics studies led to the overall detector concept presented in the ATLAS Technical Proposal[2]. The basic design criteria of the detector include the following.

- Very good electromagnetic calorimetry for electron and photon identification and measurements, complemented by full-coverage hadronic calorimetry for accurate jet and missing transverse energy ($E_T^{miss}$) measurements;

- High-precision muon momentum measurements, with the capability to guarantee accurate measurements at the highest luminosity using the external muon spectrometer alone;
- Efficient tracking at high luminosity for high-$p_T$ lepton-momentum measurements, electron and photon identification, $\tau$-lepton and heavy-flavour identification, and full event reconstruction capability at lower luminosity;
- Large acceptance in pseudorapidity ($\eta$) with almost full azimuthal angle ($\Phi$) coverage everywhere. The azimuthal angle is measured around the beam axis, whereas pseudorapidity relates to the polar angle ($\theta$) where $\theta$ is the angle from the z direction.
- Triggering and measurements of particles at low-$p_T$ thresholds, providing high efficiencies for most physics processes of interest at LHC.

The overall detector layout is shown in Figure 1. The magnet configuration is based on an inner thin superconducting solenoid surrounding the inner detector cavity, and large superconducting air-core toroids consisting of independent coils arranged with an eight-fold symmetry outside the calorimeters.

The Inner Detector (ID) is contained within a cylinder of length 7 m and a radius of 1.15 m, in a solenoidal magnetic field of 2 T. Pattern recognition, momentum and vertex measurements, and electron identification are achieved with a combination of discrete high-resolution semiconductor pixel and strip detectors in the inner part of the tracking volume, and continuous straw-tube tracking detectors with transition radiation capability in its outer part.

Highly granular liquid-argon (LAr) electromagnetic (EM) sampling calorimetry, with excellent performance in terms of energy and position resolution, covers the pseudorapidity range $|\eta| < 3.2$. In the end-caps, the LAr technology is also used for the hadronic calorimeters, which share the cryostats with the EM end-caps. The same cryostats also house the special LAr forward calorimeters which extend the pseudorapidity coverage to $|\eta| = 4.9$. The LAr calorimetry is contained in a cylinder with an outer radius of 2.25 m and extends longitudinally to $\pm 6.65$ m along the beam axis.

The bulk of the hadronic calorimetry is provided by a novel scintillator-tile calorimeter, which is separated into a large barrel and two smaller



extended barrel cylinders, one on each side of the barrel. The outer radius of the scintillator-tile calorimeter is 4.25 m and its half length is 6.10 m.

The overall calorimeter system provides the very good jet and $E_T^{miss}$ performance of the detector. The total weight of the calorimeter system, including the solenoid flux-return iron yoke which is integrated into the tile calorimeter support structure, is about 4 000 Tons.

The calorimeter is surrounded by the muon spectrometer. The air-core toroid system, with a long barrel and two inserted end-cap magnets, generates a large magnetic field volume with strong bending power within a light and open structure. Multiple-scattering effects are thereby minimised, and excellent muon momentum resolution is achieved with three stations of highprecision tracking chambers. The muon instrumentation also includes as a key component trigger chambers with very fast time response.

The muon spectrometer defines the overall dimensions of the ATLAS detector. The outer chambers of the barrel are at a radius of about 11 m. The half-length of the barrel toroid coils is 12.5 m, and the third layer of the forward muon chambers, mounted on the cavern wall, is located about 23 m from the interaction point. The overall weight of the ATLAS detector is about 7 000 Tons.

The primary goal of the experiment is to operate at high luminosity ($10^{34}$ cm$^{-2}$s$^{-1}$) with a detector that provides as many signatures as possible. The variety of signatures is considered to be important in the harsh environment of the LHC in order to achieve robust and redundant physics measurements with the ability of internal cross-check.

# 3 Magnet system

The ATLAS superconducting magnet system[3] can be seen in Figure 1. It is an arrangement of a central solenoid (CS) providing the Inner Detector with magnetic field, surrounded by a system of three large air-core toroids generating the magnetic field for the muon spectrometer. The overall dimensions of the magnet system are 26 m in length and 20 m in diameter. The two end-cap toroids (ECT) are inserted in the barrel toroid (BT) at each end and line up with the CS. They have a length of 5 m, an outer diameter of 10.7 m and an inner bore of 1.65 m. The CS extends over a length of 5.3 m and has a bore of 2.4 m. The unusual configuration and large size make the magnet system a considerable challenge requiring

careful engineering.

The CS provides a central field of 2 T with a peak magnetic field of 2.6 T at the superconductor itself. The peak magnetic fields on the superconductors in the BT and ECT are 3.9 and 4.1 T respectively. The performance in terms of bending power is characterised by the field integral $\int Bdl$, where B is the azimuthal field component and the integral is taken on a straight line trajectory between the inner and outer radius of the toroids. The BT provides 2 to 6 Tm and the ECT contributes with 4 to 8 Tm in the 0.0-1.3 and 1.6-2.7 pseudorapidity ranges respectively. The bending power is lower in the transition regions where the two magnets overlap ($1.3 < |\eta| < 1.6$).

The position of the CS in front of the EM calorimeter demands a careful minimisation of the material in order to achieve the desired calorimeter performance. As a consequence, the CS and the LAr calorimeter share one common vacuum vessel, thereby eliminating two vacuum walls.

Each of the three toroids consists of eight coils assembled radially and symmetrically around the beam axis. The ECT coil system is rotated by $22.5^o$ with respect to the BT coil system in order to provide radial overlap and to optimise the bending power in the interface regions of both coil systems.

The magnets are indirectly cooled by forced flow of helium at 4.5 K, through tubes welded on the casing of the windings. The cooling power is supplied by a central refrigeration plant located in the side cavern and the services are distributed among the four magnets.

The conductor used in all the coils is a composite that consists of a flat superconducting cable located in the centre of an aluminium stabiliser with rectangular cross section.

# 4 Inner Detector

The layout of the Inner Detector (ID)[4] is shown in Figure 2. It combines high-resolution detectors at the inner radii with continuous tracking elements at the outer radii, all contained in the CS.

The momentum and vertex resolution requirements from physics call for high-precision measurements to be made with fine-granularity detectors, given the very large track density expected at the LHC. Semiconductor tracking detectors, using silicon microstrip (SCT) [4] and pixel [5] technologies offer these features. The highest granularity is achieved around



the vertex region using semi-conductor pixel detectors. The total number of precision layers must be limited because of the material they introduce, and because of their high cost. Typically, three pixel layers and eight strip layers (four space points) are crossed by each track. A large number of tracking points (typically 36 per track) is provided by the straw tube tracker (TRT) [4], which provides continuous track-following with much less material per point and a lower cost. The combination of the two techniques gives very robust pattern recognition and high precision in $\Phi$ and z coordinates. The straw hits at the outer radius contribute significantly to the momentum measurement, since the lower precision per point compared to the silicon is compensated by the large number of measurements and the higher average radius. The relative precision of the different measurements is well matched, so that no single measurement dominates the momentum resolution. This implies that the overall performance is robust. The high density of measurements in the outer part of the tracker is also valuable for the detection of photon conversions and of $V^0$ decays. The latter are an important element in the signature of CP violation in the B system. In addition, the electron identification capabilities of the whole experiment are enhanced by the detection of transition-radiation photons in the xenon-based gas mixture of the straw tubes.

The outer radius of the ID cavity is 115 cm, fixed by the inner dimension of the cryostat containing the LAr EM calorimeter, and the total length is 7 m, limited by the position of the end-cap calorimeters. Mechanically, the ID consists of three units: a barrel part extending over $\pm$ 80 cm, and two identical end-caps covering the rest of the cylindrical cavity. The precision tracking elements are contained within a radius of 56 cm, followed by the continuous tracking, and finally the general support and service region at the outermost radius. In order to give uniform $\eta$-coverage over the full acceptance, the final TRT wheels at high z extend inwards to a lower radius than the other TRT end-cap wheels.

In the barrel region, the high-precision detector layers are arranged on concentric cylinders around the beam axis, while the end-cap detectors are mounted on disks perpendicular to the beam axis. The pixel layers are segmented in R$\Phi$ and z, while the SCT detector uses small angle (40 mrad) stereo strips to measure both coordinates, with one set of strips in each layer measuring $\Phi$. The barrel TRT straws are parallel to the beam direction. All the end-cap tracking elements are located in planes perpendicular to the beam axis. The strip detectors have one set of strips

running radially and a set of stereo strips at an angle of 40 mrad. The continuous tracking consists of radial straws arranged into wheels.

The pixel system contains a total of 140 milion detector elements, each 50 $\mu$m in the R$\Phi$ direction and about 300 $\mu$m in z. The SCT detector contains 61 m$^2$ of silicon detectors, with 6.2 milion readout channels. The spatial resolution is 16 $\mu$m in R$\Phi$ and 580 $\mu$m in z. The TRT detector consists of 320 thousand straws, the resolution in R$\Phi$ is 170 $\mu$m per straw.

The layout provides full tracking coverage over $|\eta|$ <2.5, including impact parameter measurements and vertexing for heavy-flavour and $\tau$ tagging. The secondary vertex measurement performance is enhanced by the innermost layer of pixels, at a radius of about 4 cm, as close as is practical to the beam pipe. The lifetime of such a detector will be limited by radiation damage, and may need replacement after a few years, the exact time depending on the luminosity profile. A large amount of interesting physics can be done with this detector during the initial lower-luminosity running, especially in the B sector, but physics studies have demonstrated the value of good b-tagging performance during all phases of the LHC operation, for example in the case of Higgs and supersymmetry searches. It is therefore considered very important that this innermost pixel layer (or B-layer) can be replaced to maintain the highest possible performance throughout the experiment's lifetime. The mechanical design of the pixel system allows the possibility of replacing the B-layer.

# 5 Calorimeters

A view of the ATLAS calorimeters [6] is presented in Figure 3. The calorimetry consists of an electromagnetic (EM) calorimeter covering the pseudorapidity region $|\eta|$ <3.2, a hadronic barrel calorimeter covering $|\eta|$ <1.7, hadronic end-cap calorimeters covering 1.5< $|\eta|$ <3.2, and forward calorimeters covering 3.1< $|\eta|$ <4.9.

The EM calorimeter is a lead/liquid-argon (LAr) detector with accordion geometry [7]. Over the pseudorapidity range $|\eta|$ <1.8, it is preceded by a presampler detector, installed immediately behind the cryostat cold wall, and used to correct for the energy lost in the material (ID, cryostats, coil) upstream of the calorimeter.

The hadronic barrel calorimeter is a cylinder divided into three sections: the central barrel and two identical extended barrels. It is based on a sampling technique with plastic scintillator plates (tiles) embedded in an



iron absorber [8]. At larger pseudorapidities, where higher radiation resistance is needed, the intrinsically radiation-hard LAr technology is used for all the calorimeters [7]: the hadronic end-cap calorimeter, a copper LAr detector with parallel-plate geometry, and the forward calorimeter, a dense LAr calorimeter with rod-shaped electrodes in a tungsten matrix.

## 5.1 Electromagnetic calorimeter

The Electromagnetic calorimeter (EM) [7] is divided into a barrel part ($|\eta|$ <1.475) and two end-caps (1.375< $|\eta|$ <3.2). The barrel calorimeter consists of two identical half-barrels, separated by a small gap (6 mm) at z=0. Each end-cap calorimeter is mechanically divided into two coaxial wheels: an outer wheel covering the region 1.375< $|\eta|$ <2.5, and an inner wheel covering the region 2.5< $|\eta|$ <3.2.

The EM calorimeter is a lead LAr detector with accordion-shaped Kapton electrodes and lead absorber plates over its full coverage. The accordion geometry provides complete $\Phi$ symmetry without azimuthal cracks. The lead thickness in the absorber plates has been optimised as a function of $\eta$ in terms of EM calorimeter performance in energy resolution. The LAr gap has a constant thickness of 2.1 mm in the barrel. In the end-cap, the shape of the Kapton electrodes and lead converter plates is more complicated, because the amplitude of the accordion waves increases with radius. The absorbers have constant thickness, and therefore the LAr gap also increases with radius. The total thickness of the EM calorimeter is >24 radiation lengths ($X_0$) in the barrel and >26 $X_0$ in the end-caps.

Over the region devoted to precision physics ($|\eta|$ <2.5), the EM calorimeter is segmented into three longitudinal sections. The strip section, which has a constant thickness of 6 $X_0$ (upstream material included) as a function of $\eta$, is equipped with narrow strips with a pitch of $\sim$4 mm in the $\eta$ direction. This section acts as a 'preshower' detector, enhancing particle identification ($\gamma/\pi^0$, e/$\pi$ separation, etc.) and providing a precise position measurement in $\eta$. The middle section is transversally segmented into square towers of size $\Delta\eta$x$\Delta\Phi$=0.025x0.025 ($\sim$4x4 cm$^2$ at $\eta$=0). The total calorimeter thickness up to the end of the second section is >24 $X_0$, tapered with increasing rapidity (this includes also the upstream material). The back section has a granularity of 0.05 in $\eta$ and a thickness varying between 2 $X_0$ and 12 $X_0$. For $|\eta| \geq$2.5, i.e. for the end-cap inner wheel, the calorimeter is segmented in two longitudinal sections and has a coarser

lateral granularity than for the rest of the acceptance. This is sufficient to satisfy the physics requirements (reconstruction of jets and measurement of $E_T^{miss}$). The calorimeter cells point towards the interaction region over the complete $\eta$-coverage. The total number of channels is ~190 000.

## 5.2 Hadronic calorimeters

The ATLAS hadronic calorimeters cover the range $|\eta| < 4.9$ using different techniques best suited for the widely varying requirements and radiation environment over the large $\eta$-range. Over the range $|\eta| < 1.7$, the iron scintillating-tile technique is used for the barrel and extended barrel tile calorimeters and for partially instrumenting the gap between them with the intermediate tile calorimeter (ITC). This gap provides space for cables and services from the innermost detectors. Over the range $1.5 < |\eta| < 4.9$, LAr calorimeters were chosen: the hadronic end-cap calorimeter (HEC) extends to $|\eta| < 3.2$, while the range $3.1 < |\eta| < 4.9$ is covered by the highdensity forward calorimeter (FCAL). Both the HEC and the FCAL are integrated in the same cryostat as that housing the EM end-caps.

An important parameter in the design of the hadronic calorimeter is its thickness: it has to provide good containment for hadronic showers and reduce punch-through into the muon system to a minimum. The total thickness is 11 interaction lengths ($\lambda_{int}$) at $\eta$=0, including about $1.5\lambda_{int}$ from the outer support, which has been shown both by measurements and simulation to be sufficient to reduce the punch-through well below the irreducible level of prompt or decay muons. Close to $10\lambda_{int}$ of active calorimeter are adequate to provide good resolution for high energy jets. Together with the large $\eta$-coverage, this will also guarantee a good $E_T^{miss}$ measurement, which is important for many physics signatures and in particular for SUSY particle searches.

The large hadronic barrel calorimeter (**Tile Calorimeter**)[8] is a sampling calorimeter using iron as the absorber and scintillating tiles as the active material. The tiles are placed radially and staggered in depth. The structure is periodic along z. The tiles are 3 mm thick and the total thickness of the iron plates in one period is 14 mm. Two sides of the scintillating tiles are read out by wavelength shifting (WLS) fibres into two separate photomultipliers (PMTs). The tile calorimeter is composed of one barrel and two extended barrels. Radially the tile calorimeter extends from an inner radius of 2.28 m to an outer radius of 4.25 m. It is longitudinally segmented in three layers, approximately 1.4, 4.0 and 1.8 interaction lengths thick at $\eta$= 0. Azimuthally, the barrel and extended barrels are divided into 64 modules. In $\eta$, the readout cells, built by grouping fibres into PMTs, are 'pseudo-projective' towards the interaction region. The resulting granularity is $\Delta\eta \times \Delta\Phi$=0.1x0.1 (0.2x0.1 in the last layer). The total number of channels is about 10 000. The calorimeter is placed behind the EM calorimeter (~1.2 $\lambda_{int}$)and the solenoid coil. The total thickness at the outer edge of the tile-instrumented region is 9.2 $\lambda_{int}$ at $\eta$=0.

Each **Hadronic Endcap Calorimeter**[7] consists of two independent wheels, of outer radius 2.03 m. The upstream wheel is built out of 25 mm copper plates, while the cheaper other one, farther from the interaction point, uses 50 mm plates. In both wheels, the 8.5 mm gap between consecutive copper plates is equipped with three parallel electrodes, splitting the gap into four drift spaces of about 1.8 mm. The readout electrode is the central one, which is a three layer printed circuit, as in the EM calorimeter. The two layer printed circuits on either side serve only as high-voltage carriers. This electrode structure forms an 'electrostatic transformer' (EST) with an EST ratio of two. Such a scheme has the same behaviour as a double gap of 4 mm, but without the drawbacks associated with very high voltage (typically 4 kV instead of 2 kV), and ion build up in larger gaps.

The **Liquid-argon forward calorimeter (FCAL)** [7] is a particularly challenging detector owing to the high level of radiation it has to cope with. In ATLAS, the forward calorimeter is integrated into the end-cap cryostat, with a front face at about 4.7 m from the interaction point. The FCAL consists of three sections: the first one is made of copper, while the other two are made out of tungsten. In each section the calorimeter consists of a metal matrix with regularly spaced longitudinal channels filled with concentric rods and tubes. The rods are at positive high voltage while the tubes and matrix are grounded. The LAr in the gap between is the sensitive medium. This geometry allows for an excellent control of the gaps which are as small as 250 $\mu$m in the first section. In terms of electronics and readout, four rods are ganged on the detector, and the signal is carried out by polyimide insulated coaxial cables. The number of channels is 3 584 for the total of both sides.

# 6 Muon spectrometer

The conceptual layout of the muon spectrometer [9] is visible in Figure 4. It is based on the magnetic deflection of muon tracks in the large superconducting air-core toroid magnets, instrumented with separate trigger and high-precision tracking chambers. Over the range $|\eta| \leq 1.0$, magnetic bending is provided by the large barrel toroid. For $1.4 \leq |\eta| \leq 2.7$, muon tracks are bent by two smaller end-cap magnets inserted into both ends of the barrel toroid. Over $1.0 \leq |\eta| \leq 1.4$, usually referred to as the transition region, magnetic deflection is provided by a combination of barrel and end-cap fields. This magnet configuration provides a field that is mostly orthogonal to the muon trajectories, while minimising the degradation of resolution due to multiple scattering.

The anticipated high level of particle fluxes has had a major impact on the choice and design of the spectrometer instrumentation, affecting required performance parameters such as rate capability, granularity, ageing properties and radiation hardness. Trigger and reconstruction algorithms have been optimised to cope with the difficult background conditions resulting from penetrating primary collision products and from radiation backgrounds, mostly neutrons and photons in the 1 MeV range, produced from secondary interactions in the calorimeters, shielding material, beam pipe and LHC machine elements.

In the barrel region, tracks are measured in chambers arranged in three cylindrical layers ('stations') around the beam axis; in the transition and end-cap regions, the chambers are installed vertically, also in three stations. Over most of the $\eta$-range, a precision measurement of the track coordinates in the principal bending direction of the magnetic field is provided by **Monitored Drift Tubes** (MDTs). The basic detection elements of the MDT chambers [9] are aluminium tubes of 30 mm diameter and 400 $\mu$m wall thickness, with a 50 $\mu$m diameter central W-Re wire. The chosen working point provides for a non-linear space-time relation with a maximum drift time of ~700 ns, a small Lorentz angle, and excellent ageing properties. The single-wire resolution is ~80 $\mu$m.

At large pseudorapidities and close to the interaction point, **Cathode Strip Chambers** (CSCs) with higher granularity are used in the innermost plane over $2 < |\eta| < 2.7$, to withstand the demanding rate and background conditions. The CSCs [9] are multiwire proportional chambers with cathode strip readout and with a symmetric cell in which the anode-



cathode spacing is equal to the anode wire pitch. The precision coordinate is obtained by measuring the charge induced on the segmented cathode by the avalanche formed on the anode wire.

Optical **alignment systems** have been designed to meet the stringent requirements on the mechanical accuracy and the survey of the precision chambers.

The precision measurement of the muon tracks is made in the R-z projection, in a direction parallel to the bending direction of the magnetic field; the axial coordinate (z) is measured in the barrel and the radial coordinate (R) in the transition and end-cap regions. The MDTs provide a single-wire resolution of ~80 $\mu$m when operated at high gas pressure (3 bar) together with robust and reliable operation thanks to the mechanical isolation of each sense wire from its neighbours. The construction of prototypes has demonstrated that the MDTs can be built to the required mechanical accuracy of ~30 $\mu$m.

The trigger system covers the pseudorapidity range $|\eta| \leq 2.4$. **Resistive Plate Chambers** (RPCs) are used in the barrel and **Thin Gap Chambers** (TGCs) in the end-cap regions.

The RPC [9] is a gaseous detector providing a typical space-time resolution of 1 cm x 1 ns with digital readout. The basic RPC unit is a narrow gas gap formed by two parallel resistive bakelite plates, separated by insulating spacers. The primary ionisation electrons are multiplied into avalanches by a high, uniform electric field of typically 4.5 kV/mm. Amplification in avalanche mode produces pulses of typically 0.5 pC.

The TGCs [9] are similar in design to multiwire proportional chambers, with the difference that the anode wire pitch is larger than the cathode-anode distance. Signals from the anode wires, arranged parallel to the MDT wires, provide the trigger information together with readout strips arranged orthogonal to the wires. These readout strips are also used to measure the second coordinate.

The trigger chambers for the ATLAS muon spectrometer serve a threefold purpose:

* bunch crossing identification, requiring a time resolution better than the LHC bunch spacing of 25 ns;
* a trigger with well-defined pT cut-offs in moderate magnetic fields, requiring a granularity of the order of 1 cm;
* measurement of the second coordinate in a direction orthogonal to that measured by the precision chambers, with a typical resolution of 5-10

mm.

The overall layout of the muon chambers in the ATLAS detector is shown in Figure 4, which indicates the different regions in which the four chamber technologies described above are employed. The chambers are arranged such that particles from the interaction point traverse three stations of chambers. The positions of these stations are optimised for essentially full coverage and momentum resolution. In the barrel, particles are measured near the inner and outer field boundaries, and inside the field volume, in order to determine the momentum from the sagitta of the trajectory. In the end-cap regions, for $|\eta| > 1.4$, the magnet cryostats do not allow the positioning of chambers inside the field volume. Instead, the chambers are arranged to determine the momentum with the best possible resolution from a point-angle measurement (this is also the case in the barrel region in the vicinity of the coils). The trigger function in the barrel is provided by three stations of RPCs. They are located on both sides of the middle MDT station, and directly inside the outer MDT station. In the end-caps, the trigger is provided by three stations of TGCs located near the middle MDT station.

# References


[1] 'LHC White Book', CERN/AC/93-03; 'LHC Conceptual Design Report', CERN/AC/95-05.

[2] ATLAS Collaboration, Technical Proposal for a General Purpose pp Experiment at the Large Hadron Collider at CERN, CERN/LHCC/94-43, LHCC/P2, 15 December 1994.

[3] ATLAS Collaboration, Magnet System Technical Design Report, CERN/LHCC/97-18, 30 April 1997.
ATLAS Collaboration, Central Solenoid Technical Design Report, CERN/LHCC/97-21, 30 April 1997.
ATLAS Collaboration, End-Cap Toroids Technical Design Report, CERN/LHCC/97-20, 30 April 1997.
ATLAS Collaboration, Barrel Toroid Technical Design Report, CERN/LHCC/97-19, 30 April 1997.

[4] ATLAS Collaboration, Inner Detector Technical Design Report, Volume 1 and 2, CERN/LHCC/97-17, 30 April 1997.





[5] ATLAS Collaboration, Pixel Detector Technical Design Report, CERN/LHCC/98-13, 31 May 1998.

[6] ATLAS Collaboration, Calorimeter Performance Technical Design Report, CERN/LHCC/96-40, 15 December 1996.

[7] ATLAS Collaboration, Liquid Argon Calorimeter Technical Design Report, CERN/LHCC/96-41, 15 December 1996.

[8] ATLAS Collaboration, Tile Calorimeter Technical Design Report, CERN/LHCC/96-42, 15 December 1996.

[9] ATLAS Collaboration, Muon Spectrometer Technical Design Report, CERN/LHCC/97-22, 31 May 1997.

[10] ATLAS Collaboration, First-Level Trigger Technical Design Report, CERN/LHCC/98-14, 30 June 1998.

[11] ATLAS Collaboration, Technical Coordination Technical Design Report, CERN/LHCC/99-01, 31 January 1999.

[12] ATLAS Collaboration, ATLAS Detector and Physics Performance Technical Design Report, CERN/LHCC/99-14, 25 May 1999.

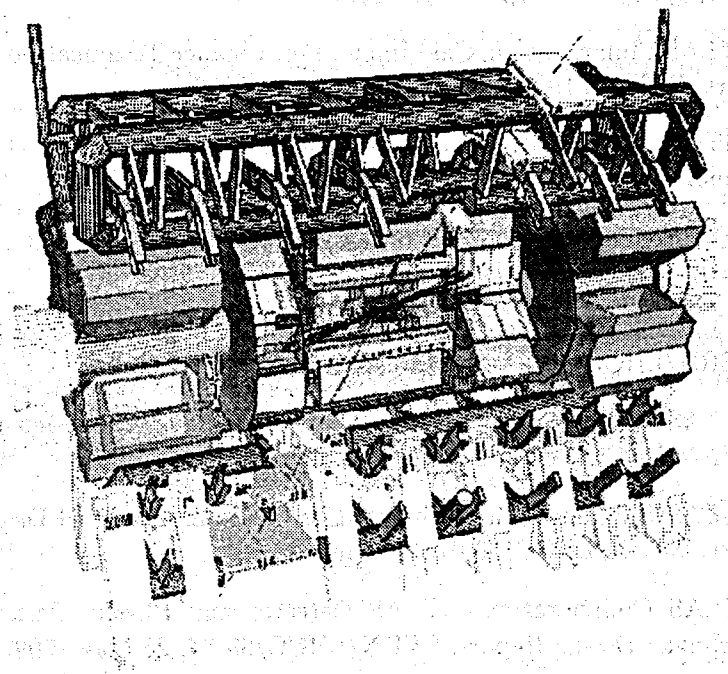

Figure 1: Overall layout of the ATLAS Detector.

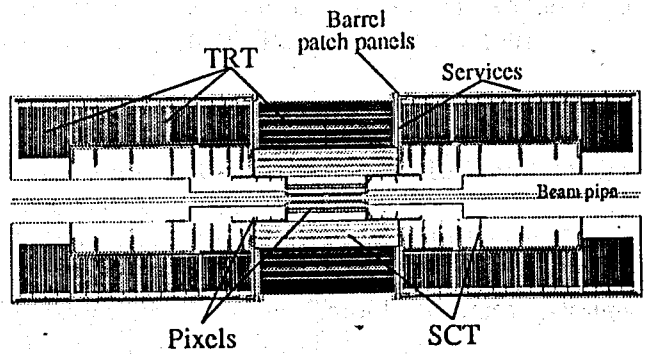


Figure 2: Longitudinal view of the ATLAS Inner Detector.



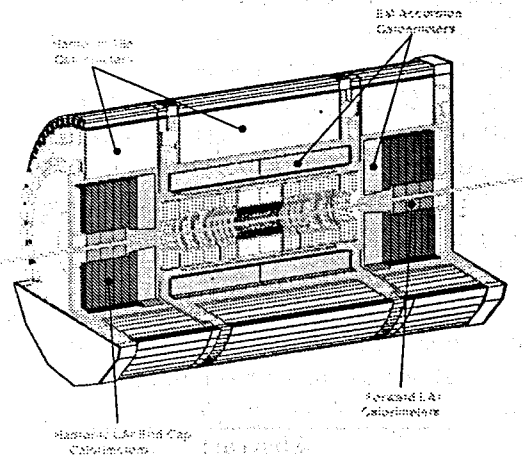

Figure 3: Three-dimensional cutaway view of the ATLAS calorimeters.

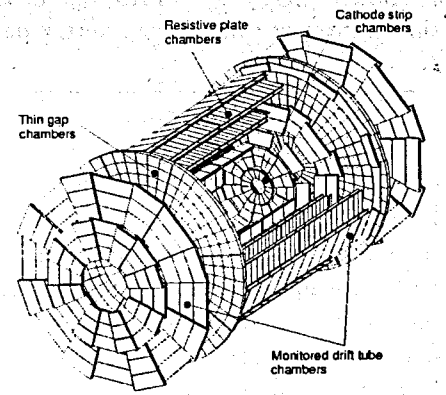


Figure 4: Three dimensional view of the muon spectrometer.

# Silicon Vertex Detectors in HEP and in the Semiconductor Tracker of ATLAS

D. Ferrère
DPNC, Université de Genève
Switzerland

**Abstract**

This contribution is an introduction to the physics and the technology of silicon microstrip particles detectors commonly used today in High Energy Physics (HEP). The intrinsic properties of semiconductor and p-n junction based on silicon are presented. The method of signal detection and the contributions to the spatial resolution of microstrip detectors are discussed. Before describing the Semiconductor Tracker (SCT) in ATLAS, one of the future LHC experiments, the features of some silicon vertex detectors used in HEP are listed.

Presented at the V$^{th}$ International School-Seminar on
**The Actual Problems of Particle Physics**
Belarus, Gomel, July 30 - August 8, 1999



## 1 Introduction

In the 1950s, electron-hole pair production in germanium junctions by $\alpha$-particles [1] was discovered. This was the starting point for the use of semiconductor detectors in nuclear physics for very precise gamma-rays energy measurements from a few keV up to 10MeV [2]. In the 1970s, this detection technique was for the first time used in High Energy Physics (HEP) as telescopes of several layers of silicon detectors for beam monitoring [3].

It was only in the 1980s that this technique was used for the measurement of particle trajectories, when J. Kemmer [4] used the planar process: oxide passivation, photo-engraving and ion implantation, for the production of a large quantity of low leakage current silicon radiation detectors. This technology is commonly used today for the fabrication of single-sided or double-sided strip (or pixel) silicon detectors for the tracking in HEP experiments.

Despite the fact that silicon detectors are still a rather expensive tracker technique, it is still very attractive for several essential features. Using up to 6 inch silicon subsrate wafers of typically 300 $\mu$m thick, desired detector shapes with small geometrical and electrical tolerances can be made. Parallel microstrip detectors with very small pitch, for example 20 $\mu$m can be designed. The close mounting of several layers of silicon detectors allows construction of telescope or vertex detectors. Hit strips with a spatial resolution of 2-3$\mu$m can be easily achieved ensuring a good vertex and impact parameter reconstructions inside the tracker detector. In addition the use of magnetic field allows the identification and the measurement of charged particles with a good momentum resolution.

As described further in this report, suitable front-end electronics to readout Si-detectors, has made also good progress. It is based on the combination of preamplification, shaping and sample and hold. Most progress has been made towards a faster signal processing with a good signal-to-noise ratio which is essential for a good reconstruction efficiency.

The last point, but not the least, is that Si-detectors can be adapted to run in severe radiation environment as required by the LHC experiments. After describing some experiments using the silicon vertex detector in HEP, a report on future module construction of the ATLAS Semiconductor Tracker [5] is presented.

# 2 Principle of the silicon detector and its operation

## 2.1 Semi-conductor properties

The semi-conductor properties are well described in solid states physics books and reference [6] is recommended for those interested to go deeper in the details.

The semi-conductors, distinct from insulators or metals, are crystalline materials with an outer shell atomic levels giving an energy band gap ($E_g$) structure of the order 1 eV for silicon. The energy gap defined between the valence band and the conduction band, known as a "forbidden" region, has no available energy levels. The conduction band, which is the highest band, is the place where electrons are detached from their parent atoms and free to move inside the entire crystalline network. The electrons in the valence band are more tightly bound and remain associated to their respective lattice atoms.

At 0°K, all the electrons are in the valence band and participate to the covalent bonding between the lattice atoms (Figure 1). Then the conductivity of the material is inexistent. At higher temperature, there is enough thermal energy to liberate some electrons to their covalent bonds to go in the conduction band and leave a hole at the original position. The hole mobility in the lattice is much lower than the electron mobility:

- the electron mobility ($\mu_e$) in silicon at 300°K is: 1350 [cm$^2$/Vs];
- the hole mobility ($\mu_e$) in silicon at 300°K is: 480 [cm$^2$/Vs].

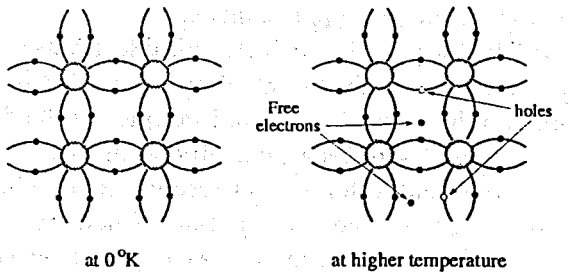


Figure 1: Covalent bonding lattice of silicon at 0°K and at higher temperature.

Electron-hole pairs are constantly being generated by thermal energy



where there are simultaneous recombinations of electrons and holes. Under stable conditions, there is an equilibrium of electron-hole pairs and the concentration $n_i$ of electrons or equally holes at a temperature T, is expressed as:

$$n_i = \sqrt{N_C N_V} exp(\frac{-E_g}{2kT}) = AT^{3/2} exp(\frac{-E_g}{2kT}) \quad (1)$$

where $N_C$ and $N_V$ are the number of states in the conduction band and in the valence band respectively.

## 2.2 Doped semiconductors

The equal numbers of electrons and holes can be changed by introducing a small amount of impurities having one more or one less valence electron in the outer atomic shell. The impurities integrate themselves into the crystal lattice creating an excess of electrons or holes (Figure 2). In this case the material is called 'doped' or 'extrinsic' semiconductor.

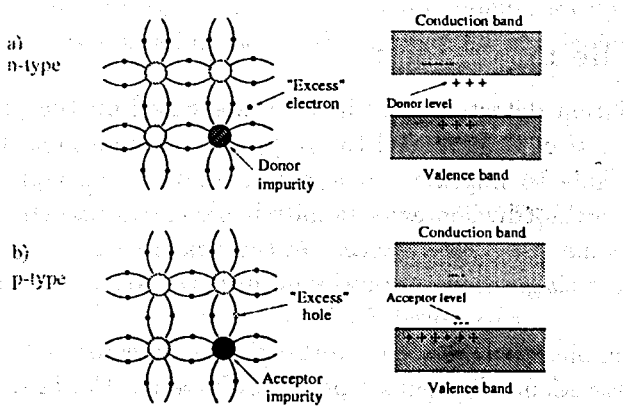


Figure 2: Intrinsic silicon doped with Donor impurities (a) and acceptor impurities (b).

If the impurity is pentavalent, the extra electron creates a discrete energy level in the band gap energy which is very close to the conduction band. So at normal temperature the electron is easily excited into the conduction band, enhancing the conductivity of the material. So the electrons are the majority charge carriers and the semiconductor is called n-type.

If the impurity is trivalent, there is an electron missing to fill the valence band. As a result there is an excess of hole, and a additional state in the band gap energy close to the conduction band is created. In this case the holes are the majority charge carriers and the semiconductor is called p-type.

The non-equal concentration of electrons and holes in extrinsic semiconductor is:

$$np = n_i^2 = AT^3 exp(\frac{-E_g}{kT}) \tag{2}$$

where $n_i$ is the intrinsic concentration. Since the semiconductor is neutral the positive and negative charge concentration is equal: $N_D + p = N_A + n$ where $N_D$ and $N_A$ are the donor and acceptor concentrations. In a n-type material one could notice that $n \sim N_D$.

Heavily doped semiconductor called $n^+$ and $p^+$ type are also used for the electrical contacts of semi-conductors where the impurity concentration in this region can be as high as $10^{20}$ atoms/cm$^3$.

## 2.3 The np junction

The radiation detectors used in HEP are based on the properties of the junction between the n- and the p-type semiconductors. The charge carriers are able to migrate across the junction if the regions are brought together but not by contact and only if the crystalline structure is continuous (see the fabrication process in the next section). So the junction is formed in a single crystal and the impurity content is different at the two sides.

The unbiased junction is working as a detector but with very poor performances and the contact potential is about 1V. In order to improve the properties of the junction, a reverse bias is applied in such way that it conducts only a small current. Applying a positive bias on the n-type contact side (Figure 3) will induce an accumulation of electrons away from the junction and towards the n contact. The same phenomena occurs on the opposite side. A depletion zone is created and is enlarged with the bias. A sensitive volume for radiation detection is therefore created and the electric field generated will help the electrons and holes, generated from the ionisation, to go to their respective attractive contact surfaces.



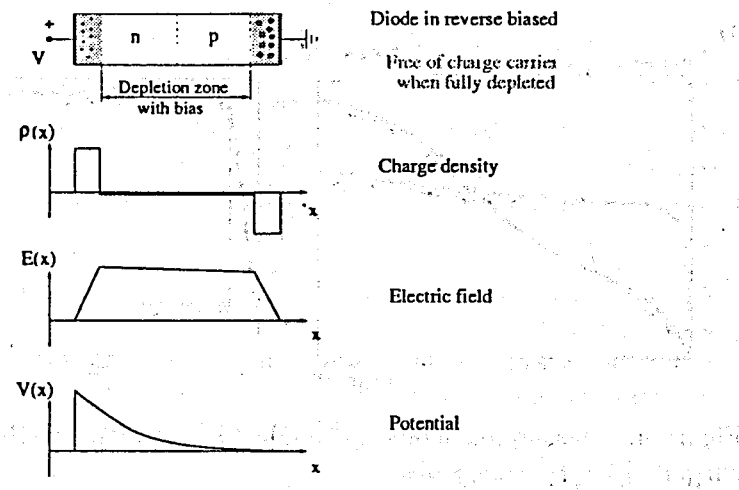


Figure 3: The np semiconductor junction under reverse bias.

The junction is fully depleted when it is completely free of charge carriers. The full depletion voltage, when the p-side doping level is predominant, can be expressed as a function of the thickness of the depletion region by the fourmula:

$$V_{fd} = \frac{\epsilon}{2\epsilon} N_A d^2 = \frac{d^2}{2\epsilon\mu_e\rho} \tag{3}$$

where $\epsilon$ is the dielectric constant for silicon: 1.05 $10^{-10} Fm^{-1}$.

For a planar detector geometry and when the junction is fully depleted the capacitance of the junction of a thickness, d, is similar to planar capacitance and is: $C = \epsilon\frac{A}{d}$ where A is the depletion area.

The total leakage current of the detectors depends of the bulk current, the surface current, and of the quality of the fabrication process [8]. When the full depletion is reached, the bulk current is due to the mobility of the intrinsic silicon carrier and a plateau can even be observed above the depletion value (Figure 4). The depletion value is estimated form the capacitance versus the bias voltage measurement. The expression:

$$1/C^2 = 2\mu\rho V_{Bias}/\epsilon \tag{4}$$

allows the best depletion voltage estimation by fitting the two parts of the curve (Figure 4).

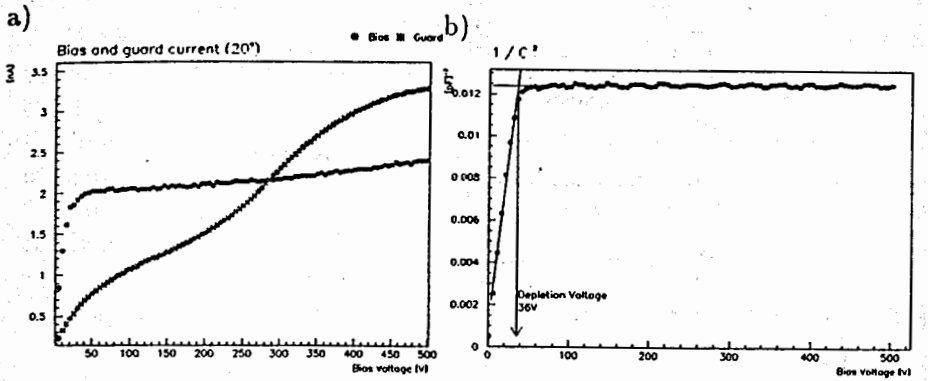


Figure 4: Measurement of a pn diode (5×5 mm²). a) Bias and guard current. b) $1/C^2$ versus bias.

## 2.4 Fabrication of silicon detectors

### 2.4.1 Silicon ingot fabrication

The fabrication of silicon mono-crystal ingots can be made either by the Czochralski method (CZ) or the float zone method (FZ). n-type or p-type ingots can be obtained by adding intentional impurities (or dopant) in the melt. Phosphorus, arsenic or antimony are typical elements for n-type material where for p-type it could be boron, gallium or indium.

The CZ method is currently used for integrated circuits (IC) and with a maximum resistivity of 1 kΩcm. This method consist of pulling a mono-crystal from a silicon melt, starting from a seed crystal with the desired orientation.

The FZ method is more appropriate for silicon detector applications where the resistivity need to be higher and much more uniform. On top of a RF heating coil ring a polycrystalline silicon rod is melted on a seed crystal at lower temperature.

### 2.4.2 The planar process

Standard double-sided polished n-type wafers with a (111) crystal orientation are generally used as the starting material. The successive steps of the planar process [7], performed under a clean room conditions, for a typical single sided $p^+$-strip on n-substrate are as follows (Figure 5):



- An oxide passivation is grown at around 1000°C with a mixture of dry oxygen and Hydrogen chloride.

- an etching step is made using a photographic mask with the opening mase according to the detector design. The mask is created on a quartz plate to ensure thermal stability. The alignment error is normally better than 1 $\mu$m.

- An ion implantation step is performed at room temperature and with a small angle to the (111) orientation to avoid channelling effects. Typically boron is used for the p-type strips and arsenic is used for the backplane n-type layer. After this implantation the wafers are thermally annealed in a dry nitrogen atmosphere.

- A metallisation is then performed on both sides with aluminium which allow to avoid any problem related to the sheet resistance of the implanted layers and to facilitate the external electrical contact.

- The aluminium is then removed from the adjacent strip using an appropriate mask.

- The wafers are finally diced to obtain the required external shape.

Depending of the detector design, some other specific steps are required, for exemple a bias resistor based on polysilicon or implanted techniques, or AC coupling which is obtained using one or more dielectric layers.

An alternative fabrication process, known as gettering technique, has been introduced by S. Holland [8]. This process is fully compatible with conventional IC processing.

# 3 Spatial resolution

When a high energy charge particle is going through a silicon detector fully depleted, an ionisation is created in the bulk. The most probable charge deposited by minimum ionising particles (MIPs) in a typical detector thickness of 300 $\mu$m is 22,000 electron-hole pairs. For a p-in-n detector the holes will drift to the $p^+$-strips and the electrons to the back plane. The incident angle of the particle will influence the number of hit strips.

The silicon microstrip localisation accuracy depends on several effects which can be internal and external:

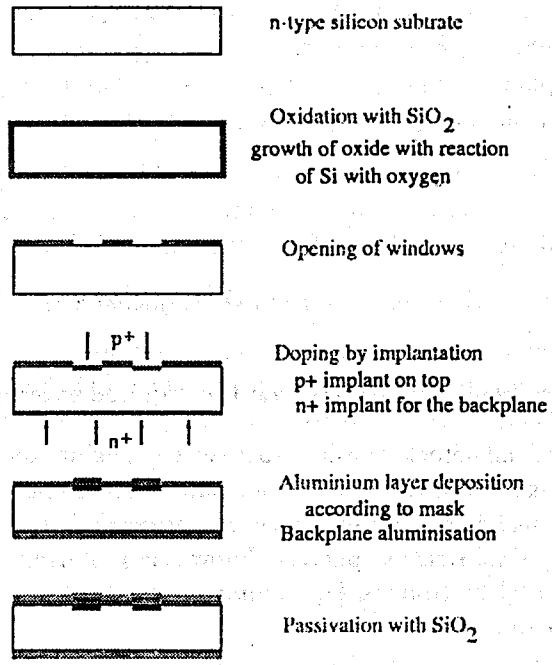


Figure 5: Successive steps of the plannar process technique.



- statistical fluctuations of the energy loss;
- the diffusion of carriers during the drift;
- the design of the strip and readout pitch;
- the electronic noise.

Internal effects such as statistical fluctuations of the energy loss or the diffusion of carriers during the drift, can lead to measurement errors of several micrometers and are described in reference [12].

## 3.1 Design optimisation

When designing a silicon vertex detector, the strip pitch is a very important parameter for optimising the hit resolution. If the pitch is too small and the signal is spread over many strips, it would result in a loss of resolution due to a reduced the signal-to-noise ratio. The lowest readout pitch realized is around 20 $\mu$m. On the other hand the number of readout strips is cost driving and must be taken in consideration in the design.

For a readout strip pitch, d, the intrinsic hit resolution resulting from an uniform distribution of probability is: $\sigma = d/\sqrt{12}$. For events generating signals on two or more strips, the hit position can be measured more precisely either by using the centre of gravity method or by using the actual shape of the charge distribution.

Another design possibility is to have intermediate strips between the readout strips. The charge sharing is then made proportionally on all the strips and the probability to have signal on two readout strips is increased compared to a single strip design. This type of design can consequently results in an improved spatial resolution.

## 3.2 Front-end electronics

The signal-to-noise ratio is a very important parameter and an optimisation can be made only by trying to minimise the equivalent noise charge (ENC) seen by the readout electronics.

The electronics chips are generally designed with preamplifiers followed by shapers and sample-and-hold circuitry. All channels (commonly 128 channels) are readout sequentially thanks to an input and output annalog multiplexing system. Each circuitry has its own maximum readout clock

frequency. The resulting peaking time ($T_p$) of the amplified and shaped analog signal is an essential parameter in the noise contributions.

The noise performance of a readout system can be expressed as [13]:

$$ENC = ENC_{pr} \oplus ENC_{lc} \oplus ENC_{br} \oplus ENC_{ms} \quad (5)$$

where

$$ENC_{pr\ (preamplifier)} = a + b \times C_{load}[pF] \quad (6)$$

Flicker and channel and bulk-resistance transistor noises are the major contributions to the preamplifier noise. $C_{load}$ is the load capacitance seen by input channel and is coming from the capacitance network of a strip to its neighbours and to the backplane. The a and b constant can be evaluated by measuring the noise performance of the chip using passive components for a given peaking time ($T_p$).

$$ENC_{lc\ (leakage\ current)} = \frac{e}{q}\sqrt{\frac{qI_{lc}T_p}{4}} \quad (7)$$

The leakage current contribution is the total leakage current of a module as seen by one channel ($I_{lc}$).

$$ENC_{br\ (bias\ resistor)} = \frac{e}{q}\sqrt{\frac{T_p kT}{2R_p}} \quad (8)$$

In the bias resistor contribution, $R_p$ is the parallel resistor of bias resistor of the detector and feed back resistor of the preamplifier.

$$ENC_{ms\ (metal\ strip)} = \frac{C_{load}e}{q}\sqrt{\frac{R_{ms}kT}{6T_p}} \quad (9)$$

This contribution is due to the metal strip resistance which depends on the width and the thickness of the aluminium strip. This contribution can be dominant for long ladders of silicon (more than 40 cm) depending of the aluminium strip resistivity [14].



# 4 Radiation effects

This aspect of radiation damages in silicon detectors is very important for the new collider experiments in LHC. The devices should be able to operate after 10 years with a total fluence of up to $10^{15}$ 1 MeV equivalent neutrons per square centimetre.

There are bulk and surface damages. The surface damages are caused by accumulation of positive charge at the silicon-oxide interface [15]. But the most studied effects are the bulk damages [16] which are displacements of silicon atoms from lattice sites.

The major known consequences are:

- the decrease of carrier mobility;
- the reduction of charge collection;
- the increase of leakage current which is directly proportional to the fluence ($\Phi$): $\Delta I_{vol}/V = \alpha\Phi$. This proportionality, $\alpha$, is called the damage constant. $\Delta I_{vol}$ is the change of the leakage current normalised to the depletion volume.
- the change of effective dopant concentration which is directly related to the the full depletion voltage. During the irradiation of a n-type substrate material, its effective dopant concentration decreases until the so-called type inversion of the detector bulk. Beyond this inversion, the majority of dopant concentration is of p-type material. So the donor removal and acceptor creation can be expressed as:

$$N_{eff} = N_0 \times e^{-c\Phi} + \beta\Phi \quad (10)$$

where $N_0$ is the initial donor concentration. $\beta$ and c are constants.

Once the irradiation is completed the effective dopant concentration will still evolve, depending on the storage temperature. This dependence has been followed intensively and one of the proposed parametrisation was set by Ziock [17]:

$$V_d = V_Z + V_S \times exp(-t/\tau_S) + V_A \times (1 - exp(-t/\tau_L) \quad (11)$$

with: $\tau_S[days] = 70 \times exp(-0.175T)$

and

$\tau_S[days] = 9140 \times exp(-0.152T)$

where T is the temperature in °C. Respectively $\tau_S$ and $\tau_L$ are the time constants of the short-term beneficial annealing and the long-term reverse annealing. $V_Z$, $V_S$, $V_A$ are constants which are proportional to the fluence and related to the induced damage. $V_Z$ is the fraction of the radiation produced acceptor concentration and gives approximately the minimum value between the beneficial and reverse annealing. $V_S$ is the meta-stable acceptor concentration produced during the irradiation process and $V_A$ is the concentration of damage sites that can become activated acceptor sites due to the anti-annealing.

Examples of the depletion behaviour are shown on the Figure 6 for detectors irradiated at $3\times10^{14}$ p/cm$^2$ and annealed over 21 days at 25 °C.

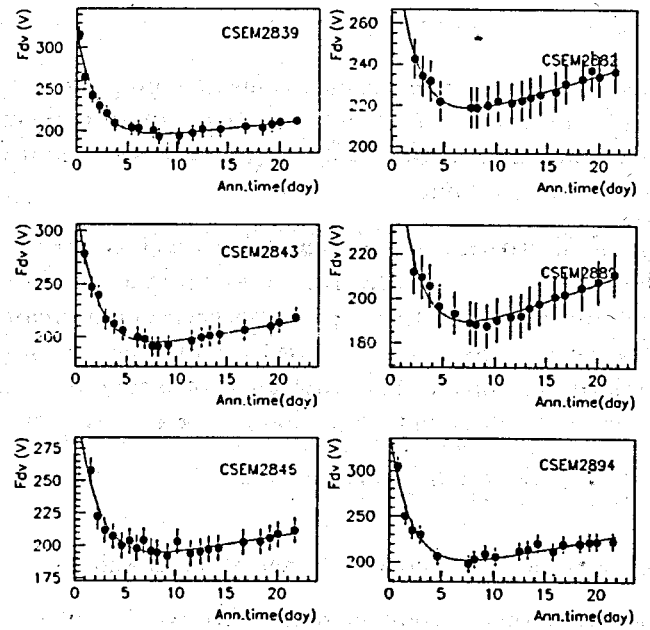


Figure 6: Depletion voltage evolution with annealing days at 25 °C of 6 irradiated p-in-n silicon detector.

The main R&D progresses on radiation effects are in the ROSE Collaboration (RD48) and in the RD39 Collaboration which is developping cryogenic tracking detectors.

The ROSE collaboration has shown very interesting results concerning the oxygenated FZ silicon wafers. The interesting effects observed on diodes [18], after high pion neutron and proton fluences, are the diminution of the number of effective dopant concentration after inversion and a delay of the type inversion (Figure 7). If this effect is confirmed on large p-in-n detectors the immediate application will be to use such materials at the inner-most silicon layers of pixel or microstrips Si-detectors in the LHC experiments.

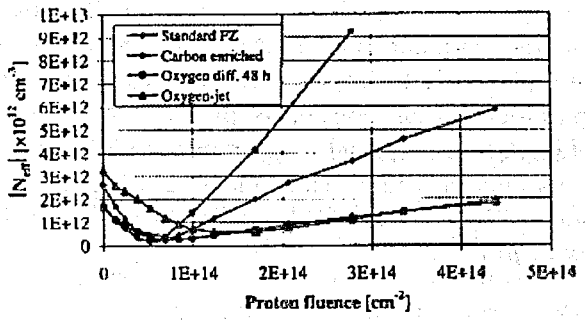


Figure 7: Effective dopant concentration versus the proton fluence [cm$^{-2}$] for different types of substrates (extracted from the results of the ROSE Collaboration).

The advantages of working at cryogenic temperatures, as shown by RD49, are very attractive, but are technically difficult over a large area. The interesting features at low temperature are [19]:

- a diminution of leakage current;
- the recovery of charge collection efficiency due to deep level trapping centres that are frozen;
- a reduction of effective dopant concentration and the possibility to control this in order to minimise the full depletion voltage.

# 5 Some applications in HEP

Silicon microstrip and pixel detectors are commonly used in HEP experiments as a high precision tracker. They are normally constructed near the

interaction region for the collider experiments. The three silicon vertex detectors mentioned here are typical examples: two are collider experiments and one is a space experiment.

## 5.1 The L3 experiment at LEP

During the first 4 years of operation (from 1989 to 1993), L3 used a tracking system based on drift chambers. In 1994 the Silicon Microvertex Detector (SMD) was installed and operational. It consists of 2 double sided layers of microstrip si-detectors made of 0.25 $m^2$ each, at radii of 64 and 79 mm [9]. The goals were primarily to improve the transverse momentum, $P_T$, and the impact parameter resolution for W physics, and secondly to improve the b-quark tagging for potential Higgs detection.

The total number of readout channels is 72576 for an ENC of 1360 $e^-$. The r-$\Phi$ single track resolution of 7 $\mu$m has been achieved where for the r-z plane it is 14 $\mu$m.

## 5.2 CDF at Tevatron

The silicon tracking of CDF is being upgraded [10] for a new run (foreseen between 2000 and 2003) of Tevatron at Fermilab with a luminosity increased by more than one order of magnitude.

One of the main results obtained from the run I is the discovery of the top quark, with the actual combined CDF and D0 mass value of:

$$m_{top} = 174.3 \pm 5.1 GeV$$

The reasons for the upgrade are:

- to improve the top quark cross section and the mass measurement;
- to improve the limits on the Higgs mass search;
- B physics studies for CP violation.

The new CDF silicon tracker is composed of 8 layers of microstrips located at radii between 1.35 and 28.0 cm of the interaction point, and represents 722,432 channels to be read-out.

The features of this new CDF tracker are:



- a precise 3D track impact parameter measurement for: top, B physics, Higgs, SUSY;
- a forward coverage which is improved compared to the silicon tracker of Run I;
- a level 2 trigger (SVT) which reduces the background by roughly 3 orders of magnitude and allow an online identification of the b-quark;
- an improvement of the transverse momentum resolution;
- a high tracking efficiency with good purity.

## 5.3 The Alpha Magnetic Spectrometer (AMS) tracker

This detector, designed to search for antimatter and dark matter in cosmic rays, is scheduled to be installed on the international Space Station Alpha (ISSA) for an operational period of 3 years. Meanwhile, the tracker, equipped with 38% of the total number of silicon sensors, was flown for 10 days on the NASA shuttle flight STS-91 in June 1998 [11]. One of the technological challenges of this flight was the vibration and acceleration hardness of up to 40 g static. Electrically, the tracker performance was unaffected by the launch and operation in space.

Double sided silicon detectors of a total of 5.4 $m^2$ are mounted on 6 layers made of ladders of up to 60cm length and are located in a permanent magnet of 0.15 T. The achieved accuracy is 10 and 30 $\mu$m in the bending and non-bending plane respectively. Thanks to the magnetic field, a momentum resolution of 7% has been obtained in the range of 1-10 GeV/c/n. The readout electronics used has a high dynamic range to allow the measurement of incident particles with an absolute charge of up to 10.

# 6 The ATLAS Semiconductor Tracker (SCT)

The SCT is based on the use of a silicon microstrip detector and it will work with other detector elements to form the inner tracking system of ATLAS [5] to study the charged particles produced by p-p collisions at the CERN LHC. This Inner Detector (ID), enclosed in a solenoid coil producing a field of 2T, is composed of 3 types of tracking system (Figure 8): The Pixel Detector, the SCT, and the Transition Radiation Tracker.

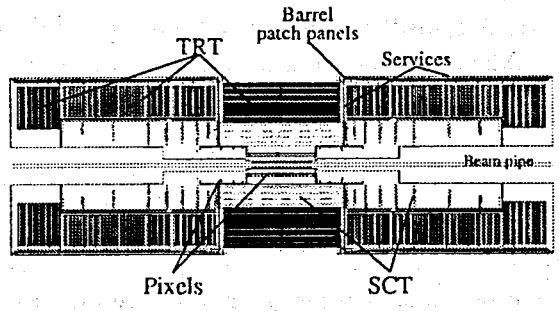


Figure 8: The ATLAS inner detector.

The expected event rate is 23 interactions every 25 ns bunch crossing for a luminosity of $10^{34}$ $cm^{-2}s^{-1}$. Due to the high bunch crossing frequency it is essential that the detectors run with fast front-end electronics and fast signal processing.

About 16,000 silicon detectors, representing a surface of $\sim$ 63 $m^2$, will be mounted on four types of SCT modules: one is the barrel type and there are three forward types for the 9×2 forward wheels. Also six different shapes of silicon wafer of 768 readout strips are required: one rectangular of 64×63.6 $mm^2$ and five wedge types.

## 6.1 The silicon detector features

The ATLAS SCT prototype detector studies are performed according to predefined pre- and post-irradiation specifications. The wedge detectors dedicated for the forward wheels are designed with varying strip pitch between $\sim$ 50 to 90 $\mu$m where for the barrel the pitch is 80 $\mu$m and constant. Each strip is biased via a polysilicon or an implanted resistor to the bias line with the value specified to be in the range of 0.75 and 2.0 MΩ. Additional guard rings are usually designed to set a field potential barrier between the cutting edge and the active sensor area (Figure 9).

As explained previously the features of the detectors are altered by radiation damage with particle fluence. In addition to that, the environmental temperature of the sensors must be low, to limit the total leakage current, and to avoid the rapid variation of the effective dopant concentration during the anti-annealing post-irradiation period. The normal operating temperature sensors will be around -7 °C during the 10 years of operation, excepting the detector maintenance. The unavoidable yearly



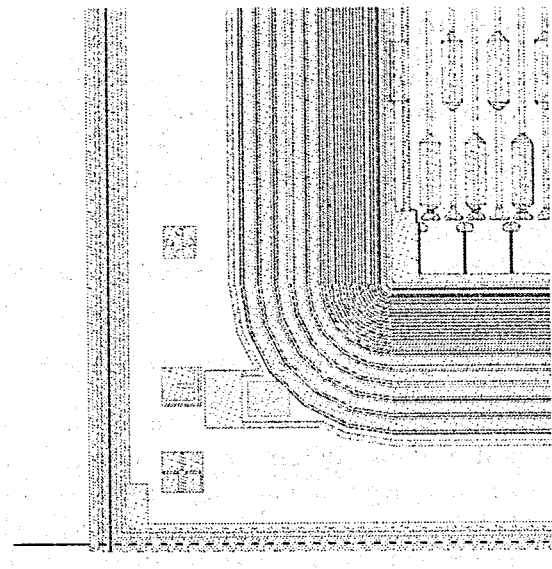

Figure 9: ATLAS silicon detector corner layout.

detector maintenance will impose a warm-up of 2 days at 20 °C and 2 weeks at 17°C. According to the Ziock parametrisation (Formula 11) the maintenance over the full ATLAS operation is equivalent to 21 days at 25 °C. This is used as the official annealing time period for the post-irradiation detector prototype studies.

The use of $p^+$-implanted silicon strip detectors is the technological baseline for SCT compared to the $n^+$-implanted strip which was one of the options [20]. The n-in-n detectors show a better efficiency below the depletion compared to the p-in-n after a significant particle fluence (beyond the type inversion). This is explained by the fact that after the inversion type (section 4), for the $n^+$-strip detectors the depletion region starts from the strip side where for $p^+$-strip detectors the depletion is starting from the backplane. However, it has been showed that for the p-in-n detectors with a lower production cost than with n-in-n, the full efficiency was achieved above 300V for detectors from different manufacturers.

## 6.2 The front-end electronics

The front-end readout electronics, based on a one-bit digital (binary) readout architecture, is responsible for supplying strip hit information. It needs to be close to the silicon strip electrodes to ensure low noise operation. The integrated circuits (IC) readout chips are set on electronics hybrids. Those hybrids have two functionalities:

- electrical: for the power, ground, clocks, control, out-put data, chip links, detector biasing and filtering;

- thermal: a high conductivity is important for the power dissipation.

An optical communication scheme is chosen, because of its low mass and lack of electrical pick-up. Initially a light diode (LED) option was considered, but there is concerned about ageing due to severe radiation. The VCSEL (Vertical Cavity Surface Emitting Laser) technique is now considered.

As described previously the front-end architecture is based on amplification, shaping and discrimination to give hit/no-hit information for each bunch crossing. Based on an extensive development program, two technological options of 128 channels exist. In the first, the total functionalities resides in a single chip based on the DMILL BiCMOS technology. The second option, has the analog part on a single chip (CAFE-M) where the preamplifier, the shaper and the discriminator are realised in a bipolar technology. On this last option the digital part, the ABC pipeline, is realised in a CMOS technology.

The chips must remain operational during 10 years of data taking and a target signal-to-noise (S/N) ratio of 12 is expected at the end of the detector lifetime. The behaviour of S/N with the particle fluence have been simulated and several effects has been taken into account:

- the electrical parameters of the strip detectors such as resistance and inter-strip capacitance;
- the diminution of the charge collection efficiency and the ballistic deficit due to charge collection time;
- the increase of the detector leakage current.

A summary of the chip parameters are listed in Table 1.



| Parameter | Specification |
|---|---|
| Noise | $\leq$ 1500 $e^-$ |
| # Readout channels | 12×128 |
| Efficiency | 99% |
| Noise occupancy | $5\times10^{-4}$ |
| Double pulse resolution | 50ns for 3.5fC |
| Large charge recovery (80fC) | 1$\mu$s for 3.5fC |
| Power dissipation | $\leq$ 3.8 mW/channel |

Table 1: Summary of some chip parameters.

## 6.3 The module construction

Since the physics require a very good accuracy on the readout strip positions the module construction needs to be very precise. This means that the module must achieve a relative XY detector alignment of $\pm$ 4 $\mu$m on one side and $\pm$ 8 $\mu$m between the 2 stereo sides at $\pm$ 20 mradian.

Special materials and particular designs for barrel and forward modules will be used in such a way that the mechanical and thermal performances are optimised. The larger power consumption is coming from the hybrid (roughly 4.5 W) and it is important that the heat transfer between the hybrid and the detectors, normally operating at -7 °C, is minimised in order to avoid the thermal run-away of the module. Two types of module will be produced:

- one for the barrel structure where the electronics is centre-tapped. The detectors are glued to a pyrolitic graphite (TPG) heat spreader and a beryllia baseboard for mechanical rigidity (Figure 10).

- one for the forward wheels where the electronics is end-tapped. The hybrids are mounted at the far-end extremity and joined to a TPG spine to receive the detectors. A special cooling block separating thermally the hybrid and the detectors also serves as mounting point. Another cooling point at the opposite side is used for heat detector dissipation and also for mechanical fixation.

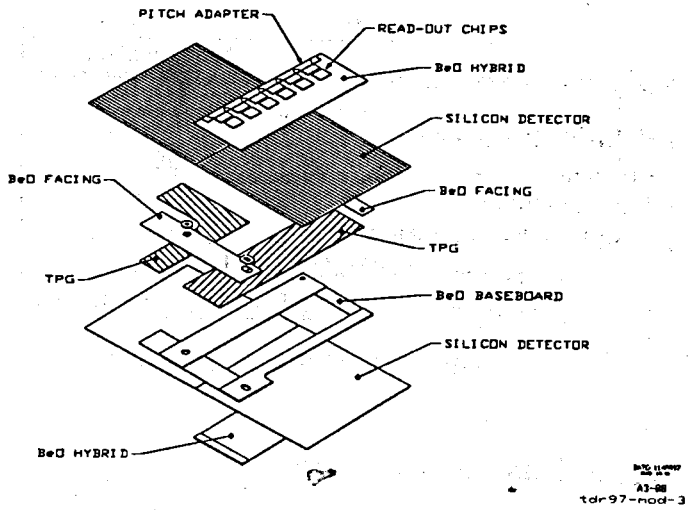


Figure 10: Expended view of the barrel module.

# 7 Conclusions

Precise vertex detection based on silicon microstrip and pixel detectors is a well known technique currently used in HEP. These detectors are also referred as solid state detectors used originally in electronic circuits. A spatial hit resolution of 3 $\mu$m can be achieved by optimising the detector design and using the relevant front-end electronics. Nevertheless, particular attention needs to be paid to the mechanical construction and assembly of the global detector, not losing the detector precision by mis-alignment. The readout chips has been extensively developed for application such as low noise amplification, fast shaping, high dynamic range, severe radiation environment...

As explained in this report, the silicon detectors can operate in high particle fluences (up to $10^{15}$ equivalent 1 MeV neutron/cm$^2$) and the consequences are well known. Some hopes reside in the recent results of the ROSE collaboration concerning the oxygenated FZ Si-substrate to be used for the inner most detector layers.

Despite the rather expensive technique, the silicon detector is a very attractive choice for any charge particle detection in HEP, or for other applications such as medical imaging.



## Acknowledgements

I would like to thank Professor Allan Clark, and Dr. Peter Jenni for encouraging me to present this topics at the Gomel 1999 school seminar on "Actual Problems of Particle Physics".

I would like to thank all my colleagues in the NOMAD and in the ATLAS SCT experiments in the field of silicon detectors, and with whom I could learn most of the specific features of that technique.

Finally I warmly thank all the members of the organising committee of the School-Seminar for their kindness and support during my stay in Gomel.

# References

[1] K.G. McKay, Phys. Rev. 84 (1951) 829.

[2] Glenn F. Knoll, Radiation Detection and Measurement, Second Edition.

[3] G. Bellini et al., Nuclear Instruments and Methods 107 (1973) 85.

[4] J. Kemmer, Nuclear Instruments and Methods 169 (1980) 499-502.

[5] ATLAS Inner Detector Technical Design Report, CERN Internal Report, CERN/LHCC/97-16 and CERN/LHCC/97-17, April 1997.

[6] S.M. Sze, Physics of Semiconductor Devices, Second Edition.

[7] J. Kemmer, P. Burger, R. Henck, E. Heijne, IEEE Transactions on Nuclear Science 29 (1982) 733-737.

[8] S. Holland, Nuclear Instruments and Methods A 275 (1989) 537-541.

[9] M. Acciarri et al., The L3 Silicon Microvertex Detector, Nucl. Instrum. Methods Phys. Res., A 351 (1994) 300-312.

[10] A. Sill, CDF Run II Silicon Tracking Projects, presented at Vertex99 Workshop, Texel, Netherlands.

[11] W.J. Burger, The Alpha Magnetic Spectrometer Silicon Tracker, Nucl. Instrum. Methods Phys. Res. A 435 (1999) 202-214.

[12] A. Peisert, Silicon Microstrip Detectors, Delphi intenal note 92-143.

[13] G. Barichello et al., Performance of long modules of silicon microstrip detectors, Nucl. Instrum. Methods Phys. Res. A 413 (1998) 17-30.

[14] D. Ferrère, Development of a Silicon Tracker for Neutino Physics, Nuclear Physics B, 61B (1998) 187-194.

[15] T.P. Ma, P. Dressendorfer, Ionisation radiation effects in MOS devices and circuits, Publ Wiley, New York, (1996).

[16] B. Dezillie, PhD thesis, CERN and Univerity Joseph Fourier - Grnoble 1, September 25th 1997.

[17] H.J. Ziock et al., Nucl. Instrum. Methods A 342 (1994) 96.

[18] A. Ruzin et al., Radiation effects in silicon detectors processed on carbon and oxygen rich substrates, ROSE/TN/99-5.

[19] P. Collins et al., Cryogenic Operation of Silicon Detectors, Preprint submitted to Elsevier.

[20] P. Allport at al., ATLAS irradiation studies of n-in-n and p-in-n silicon microstrip detectors, Nucl. Instrum. Methods Phys. Res. A 435 (1999) 74-79.



# TRIGGERING in CMS

H. Rohringer

*Institute for High Energy Physics, Vienna, Austria*

**Abstract**

In high energy physics experiments at LHC triggering is a crucial part of the experimental setup to reach the goal of studying interesting physics. We give basic general considerations for triggering, we show the strategies , which CMS has developed both in hardware and software and we explain in some details the muon and calorimeter algorithms foreseen at the moment. As the trigger system is an integral part of the data acquisition system we will explain also some of its details.

# 1 Introduction

The experiments running under LHC conditions face several problems. The date rate will be far higher as was common until today - every 25 Nanoseconds we will have around 30 collisions -, we envisage a high radiative environment, the information gained from the detectors is enormous and the energy regime is completely new and we can only make educated guesses on what will happen. We expect that interesting collisions and the occurence of new objects will be rather rare and hidden in a big bulk of 'conventional ' and understood processes. Storing these data is physically not possible and also the capacity of computing systems available now is by far not sufficient to find and filter interesting objects. Therefore a **trigger** system should decide which data are kept for later processing. Unfortunately the decision time available is rather restricted as data have to be stored during this time and storage space is also limited, so complicated computations are not feasible.

The **CMS trigger system** will work in stages and is heavily pipelined and parallelized. Fast decisions will be taken mainly by **programmable hardware**- where only simple algorithms can be applied. This **'first level trigger system '** uses only data from the **muon** and **calorimeter-systems** and will decide wether data from different detectors will be read out and are therefore usable further on or not. Then in stages ' **higher level triggers'** - which in contrast are based on computercalculations - we will gradually use more data - eg from the tracker - to make decisions.

# 2 Introduction

In fig 1 we show a picture of a simulated Higgs event embedded in an ' underlying event ' as observed by the **tracker** system of the CMS detector , where we have restricted the displayed tracks to those having a $p_T$ bigger than 2 GeV/c. As the signal for Higgs are 4 muons, we restrict ourselves now to tracks with $p_T > 25$ GeV/c and are then confronted with more clean conditions which are characteristic for this event type. We could therefore take this condition clearly for **triggering purposes.**

Taking this example we define as the **purpose** of a **'TRIGGER'** the **SELECTION** of data/events with specific properties ( in our case 4 muons with more than 25 GeV/c) which are then written to a storage medium.

The trigger conditions are guided by **physics reasons, detector requirements, data acquisition(DAQ) boundary conditons, event rates** and the **computing time available until a decision is taken.**

Our **aims** are to **reduce** from the **40 Mhz data rate of LHC to 100 Khz** in the **first level trigger system** within **3.2 microseconds.** Gradually the following stages will reduce to 1 Khz and then finally to 100 hz on an output medium.

# 3 CMS-DETECTOR

First we show the CMS - detector in fig 2. But at the moment it is **NOTFEASIBLE** to use all parts of the detector for triggering purposes. The main restriction is the amount of data available - which should be kept small. In tab 1 we give the number of channels forseen in the



## Higgs decay in 4 μ (+30 minimum bias events)

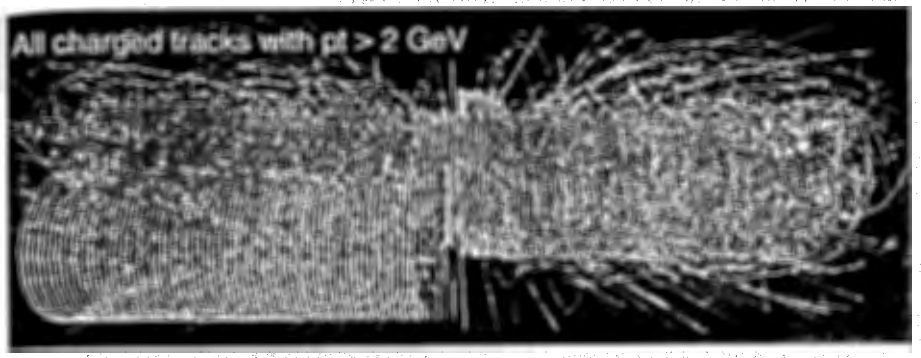


The next step needs to search for a wide range of massive objects. The hadron colliders can provide the exploratory physics with high constituent √s and with high luminosity, but at the expense of clean experimental conditions

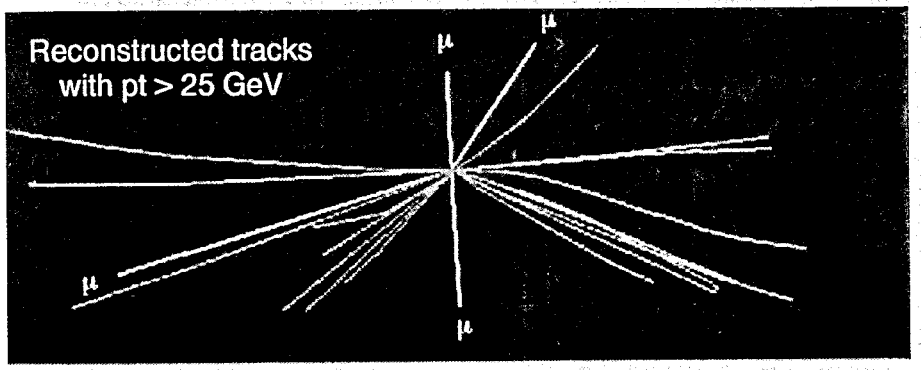


Figure 1: HIGGS DECAY into 4 muons with back ground events

CMS detector. Clearly the tracker part is rather heavy. Therefore we restrict ourselves for the **fast decisions only to the muon and calorimeter system.**

Table 1: Average sub–detector event size at nominal luminosity of $10^{34}\ cm^{-2}\ s^{-1}$.

| Subdetector | No of channels | Occupancy [ % ] | Event size (kByte) |
|---|---|---|---|
| Pixel | 80 000 000 | 0.01 | 100 |
| Inner Tracker | 16 000 000 | 3 | 700 |
| Preshower | 512 000 | 10 | 100 |
| Calorimeters | 250 000 | 10 | 50 |
| Muons | 1 000 000 | 0.1 | 10 |
| Trigger | 10 000 | 100 | 10 |

# 4 Trigger quality requirements

We require **fast decisions** because of the high rate, **no latency** ( at no instant the system should be unable to take or analyse data because of some bottleneck or unavailability of components), **selectivity** ( a given condition should be fullfilled without 'smearing' and 'overlap' to neigbouring conditions - ( eg a trigger of 60 GeV/c should not also comprise tracks < 60 GeV/c)

Certainly we need **high efficiency**- which is the ratio of reconstructed and produced objects. **Purity** should guarantee to get what one likes to get ( a single gamma trigger should not also have a admixture of hadrons ). The **capability** of the system to cope with the data supplied is a matter of thoughtful considerations as well as the **flexibility** to be adaptable to unforseen situations. Of course **cost** ( 47 Million SFR are allocated to the trigger system at the moment) and **modularity** of the system for easy exchange in the case of failure or different functionality are essential. All the software and hardware components have to be designed in this respect.

We also refer to the CMS expression **'latency'** in another context. It denotes also the time between the availability of data in the detector and the result of calculations for triggerpurposes with them. So the 3:2 $\mu$ sec for the triggerdecision would also be called 'latency'.

# 5 Typical events - HIGGS search

In fig 3 we show typical decay modes of the HIGGS - where LHC should be a real discoverer - and the detector components involved.

# 6 Simulation software

## 6.1 Triggersimulation

Designing trigger functions needs rather big simulation efforts.They comprise simulation of the **trigger algorithms** and the **hardware functionality**. The triggeralgorithms are tested on various sets of simulated data under considerations of detector specifica and the possibilities of only partial functionality of the system. This should be close to the hardware reality, though some features - like parallelism - cannot really be simulated.



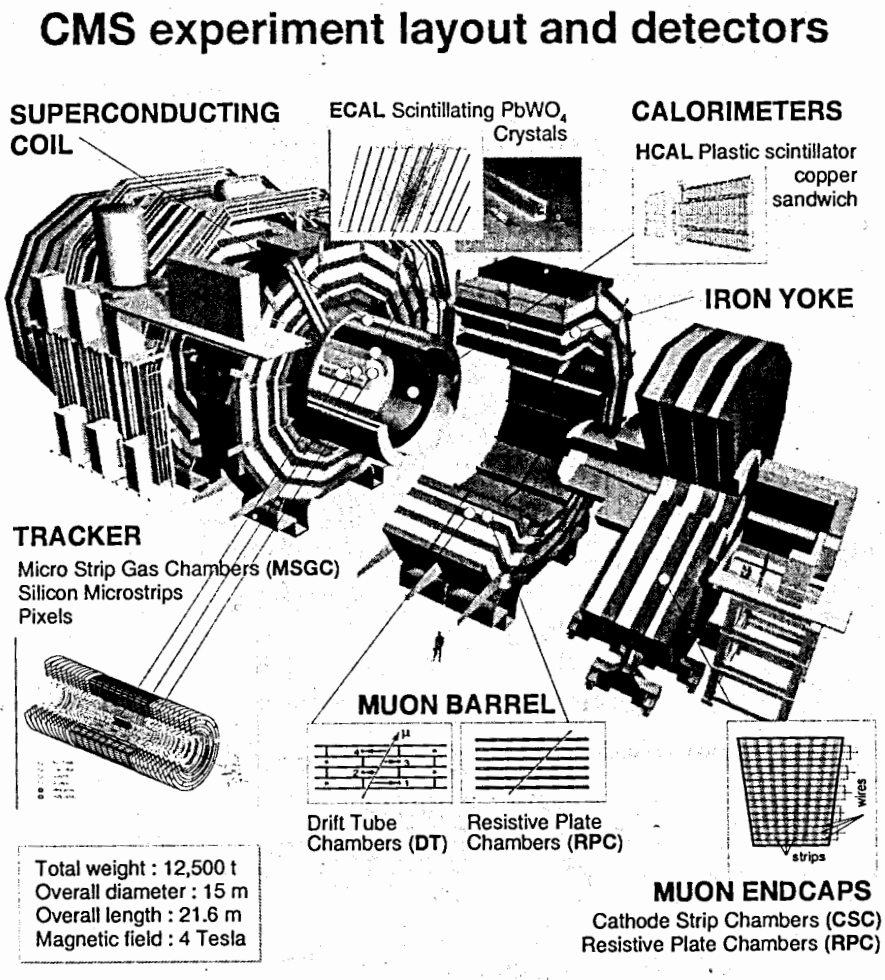


Figure 2: CMS Detector and data output

## Higgs to 2 photons ($M_H$ < 140 GeV)

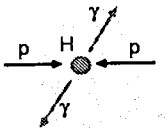


$H^0 \rightarrow \gamma\gamma$ is the most promising channel if $M_H$ is in the range 80 – 140 GeV. The high performance $PbWO_4$ crystal electromagnetic calorimeter in CMS has been optimized for this search. The $\gamma\gamma$ mass resolution at $M_{\gamma\gamma} \sim 100$ GeV is better than 1%, resulting in a S/B of ≈1/20

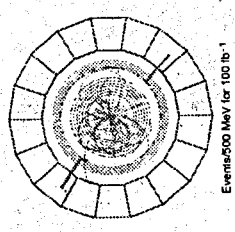

$M_{Higgs}$ = 100 GeV

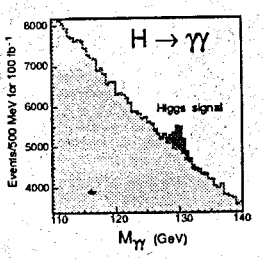


## Higgs to 2 leptons+2 jets ($M_H$ > 500 GeV)

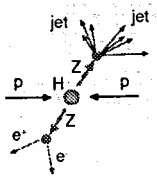


For the highest $M_{VV}$ in the range 0.5 - 1 TeV, the promising channels for one year at high luminosity are $H^0 \rightarrow ZZ \rightarrow \ell^+\ell^-\nu\nu$, $H^0 \rightarrow ZZ \rightarrow \ell^+\ell^-$ jj and $H^0 \rightarrow W^+W^- \rightarrow \ell^\pm\nu$ jj. Detection relies on leptons, jets and missing transverse energy ($E_T^{miss}$), for which the hadronic calorimeter (HCAL) performance is very important

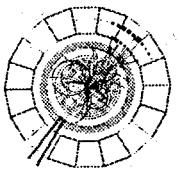

$M_{Higgs}$ = 800 GeV

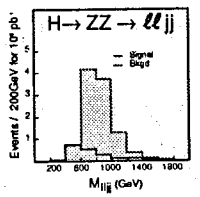


Figure 3: Higgs decaymodes seen in the CMS Detector



## Higgs to 4 leptons (140 < $M_H$< 700 GeV)

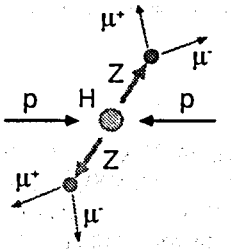


In the $M_H$ range 130 - 700 GeV the most promising channel is $H^0 \rightarrow ZZ^* \rightarrow 2\ell^+ 2\ell^-$ or $H^0 \rightarrow ZZ \rightarrow 2\ell^+ 2\ell^-$. The detection relies on the excellent performance of the muon chambers, the tracker and the electromagnetic calorimeter.
For $M_H \leq 170$ GeV a mass resolution of ~1 GeV should be achieved with the combination of the 4 Tesla magnetic field and the high resolution of the crystal calorimeter

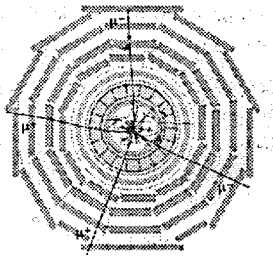

$M_{Higgs}$ = 150 GeV

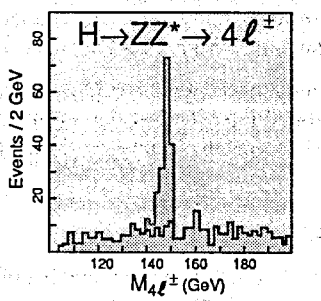


Figure 4: Higgs decaymodes seen in the CMS Detector cont

Hardware simulation is useful and needed before actual (expensive) building of moduls. Certain programs like VHDL test the hardware functionality, feasibility and validity of the design in respect to timing, connectors, size, speed, dataexchange, overflow, size of layout etc of the hardware elements of the implemented algorithms. Both the hardware and software simulations need to be cross checked for hidden errors.

## 6.2 Detectorsimulation

The simulation of the detector behaviour in CMS is based on **GEANT** . The CMS specific parts are put together under a fortran based program package called **CMSIM** . This allows to study in detail the response of the various detectorparts if a particle crosses, gives the information on hits and the expected electronic signals together with noise and other background. This package has grown enormously in size and is therefore now replaced by a more flexible system based on modern softwaretools like Object oriented programming under C++ and the usage of commercial databases. Drawback is the rather slow performance of these systems.

To study detection aspects of physics processes,acceptance,efficiency,response and the ratio of signal to background a specific **fast simulation tool** has been developed based on a parametrization of the detectorelements, which has steadily to be cross checked to the CMSIM simulation.

# 7 Triggerstrategy

CMS has decided to use only a small number of simple objects for triggering purposes on the **lowest ( first ) level**, where decisions have to be taken within 3.2 $\mu$ seconds. Therefore for **each type of detectors** only at most **four objects** of **'highest rank'** will be selected from the **'LOCAL (eg detectorbased) triggersystems'**. The triggerobjects are characterized by a few values called **TRIGGERPRIMITIVs** like position and bending angle of a track at a point in the muon chambers, or $\eta$ value and transverse energy of a calorimetercell containing a jet.

These objects are

- 4 muons of highest $p_t$ from the muon system
- 4 (non) isolated electrons/$\gamma$s from the electromagnetic calorimeter
- 4 jets of highest $E_t$

We adopt a **REGIONAL TRIGGER** concept , whereby the same algorithmic function works **fast** and **parallel** on different data of regional detector parts. The 'local regions' come from the geometry of the construction. As an example we take the **muon chambers** which are organized in 12 $\phi$ segments in 5 'wheels' in beam direction. Each of the $\phi$ segments is associated with a trigger processor. Similarly for the **calorimeters** we have a processor for a 4*4 tower region as a basic 'local region'.

But we abstain from rather timeconsuming data exchange of neighbouring regions and compare and combine such data only in a later stage of the triggerchain.



Important features of our triggersystem are therefore **parallel processing** and in addition we rely on heavy **pipelining**. This means that the trigger data are **NOT STATIC** in some memories, but they constantly **move** with the LHC clockcycle of 40 Mhz, so that **functional units** can perform their tasks consecutively on the data in motion.

In the **GLOBAL TRIGGER** system we can set threshold conditions on these objects ( like $p_t$ cuts), require common conditions on different objects (eg 2 muons and 4 jets ) and set relations between objects ( eg 2 opposite sign muons with an angle of 180 degrees) to select certain physics channels.

## 7.1 Triggerhierarchies

Because of the complexity **triggerdecisions** are taken in **steps** which we call **levels**. The reason of this level scheme is the necessity of **preselections** and **strong data** reduction to store data for offline physics analysis.

- **LEVEL 1 TRIGGER : FAST HARDWARE LOGIC**

  The aim is, to have after a **latency** of **128 bunchcrossings = 3.2 $\mu$ sec a decision** , wether to take data from the event buffers or not for further processing

  This stage uses algorithms which perform only 'basic' operations like

  - logical and/or
  - add and multiply
  - comparison of values from trigger objects
  - comparison of values from trigger objects with precalculated tables
  - only **integer arithmetic** , no floating numbers, no exponential functions, no square roots etc

  Designing trigger algorithms also require to **think in hardware terms** of the system. Therefore certain measurement values like angles are not given in floating point numbers but instead they appear in units with certain precision eg number of bits. Each bit is normally realized by a wire - which needs consideration of cost and complexity of connections. This means a compromise to the size of datawords , which should be kept as small as possible with the guarantee of sufficient precision.

  Ex : after 128 bunchcrossings we know, wether 2 opposite sign $\mu$ both with $p_t > 50$ GeV/c and 2 jets with transverse $E_t > 200$ GeV/c have been in the event or not.

  Several decisions from the **'local triggers'** are combined in the **'global trigger'**. These conditions are programmable and set from outside by **phycisists** and decide on the type of events which will be taken from the event buffers for further analysis in higher trigger levels.

  **LEVEL 1 TRIGGER algorithm have reached the stage to be READY for HARDWARE implementation and testing.**

- **LEVEL 2 TRIGGERs**: also called **HIGHER LEVEL TRIGGERS**

- start calculating gradually on full data of the detectors - not only on Triggerprimitives - with computerfarms
- include and combine information from more detectors ( like the trackersystem )
- try to reach selection criteria for interesting events
- introduce algorithms to get rid of unwanted events to reduce the data which have to be stored for further analysis '
  like
  * reduction of single jet and electron rate
  * filtering of events containing b quarks with electron signals
  * get rid of $\mu$ from $\pi$ decays or $\gamma$s from $\pi^0$
  * select certain channels like 2 muons and jets in opposite hemispheres ( for Higgs..)

This triggering level is heavily interconnected with the DAQ system, because data from the detector buffers are put together to full events. This process - called **switching** - has still rate problems as sufficiently capable hardware is yet not available. Therefore smaller data pieces are transferred consecutively in 'levels' and calculated, and intermediate decisions are taken, but book keeping necessity is rather high. A lot more R & D and experience is required in this triggering stages.

# 8 Physics channels and Triggerobjects

We have previously shown typical decay modes of the Higgs as they will appear in the CMS detector.

Higgs == > 2 $\gamma$s

Higgs == > 4 leptons

Higgs == > 2 leptons + 2 jets

## 8.1 Detectors used for Triggering

The **MUONS** will be triggered by

- Drift tubes (DT)
- Resistive Plate Chambers (RPC)
- Cathode Strip Chambers (CSC)

These detectors are grouped in **STATIONS**

The **ELECTRONS/$\gamma$s** will be triggered by

- Electromagnetic Calorimeter (ECAL) consisting of



  - 80 000 crystals $PbWO_4$ niobium and lanthan doped
  - weight 90 tons, partially produced in Russia & GUS
  - traversing particels produce em showers, with the light collected in avalanche diodes
  - granularity 0.0175 $\phi$ * 0.0175 $\eta$
  - face front 22 * 22 $mm^{**2}$
  - grouped in regional towers of 5 * 5 crystals

The **JETS/HADRONS** will be triggered in the HADRON CALORIMETER **(HCAL)** consisting of

- 17 sampling layers to analyse the shower shape produced by particles traversing Cu-Zn absorbers
- showers produce light in plastic scintillators
- light is collected in hybrid photodiodes (HPD)
- granularity 0.0875 $\phi$ (=1°) * 0.0875 $\eta$ in the **BARREL** region
- grouped in single hadron towers matching ecal towers and 4*4 tower jet groups
- Cu absorbers with embedded quartz fibers insensitive to neutrons in **FORWARD** regions

## 8.2 Triggerregions

Since we have a solenoidal Magnetic Field of 4 TESLA our symmetry is choosen to be in $\eta$ and $\phi$.

We define certain **TRIGGER REGIONS** of the detector

- **BARREL**
  - for muons 0. < / $\eta$ / < 0.8
  - for calor 0. < / $\eta$ / < 1.3
- **ENDCAP**
  - for muons 1.2 < / $\eta$ / < 2.6
  - for calor 1.3 < / $\eta$ / < 3.0
- **FORWARD** for calor up to / $\eta$ / = 5.0

## 8.3 Trigger Latency and Time Delay

With **trigger latency** we denote now the **time length** which the trigger needs until a **final decision.** It is bound to **128 bunchcrossings or 3.2** $\mu$ sec. This comes from the **number of events** that can be **stored** in the front end buffers of the different detector and would be bigger with an increased buffer size.

The storage capacity is for

| | |
|---|---|
| PIXEL | 12 - 64 events |
| TRACKER | 6 events |
| ECAL | 16 events |
| HCAL | 22 events |
| CSC | 85 events |

Nevertheless **every 25 nsec a trigger decision is taken** - but the result is available **only** after a **latency** ( time delay ) of 128 bunchcrossings.

As we have a **strict time budget** careful timing is needed for the algorithms, since we have unavoidable time consuming processes in the system.

As an example we show the **time budget for the DT trigger system.**

| | |
|---|---|
| data transfer 120 m from detector to counting house | 58 BX |
| data transfer back ('readout signal') +resynchronising | 15 BX |
| drift time in Drifttubes | 16 BX |
| **LEVEL 1 LOCAL PROCESSING** | 9 BX |
| **MUON TRACK FINDER** | 17 BX |
| **GLOBAL TRIGGER** | 14 BX |

Clearly the 'system overhead' is much bigger than the time for running trigger algorithms.

# 9 TRIDAS - the TRIGGER and DATA ACQUISITION SYSTEM of CMS

We have described the basic structure and strategy of the CMS triggersystems. But it is essential, to understand how data flow inside the system.

Basically the detectors produce per bunchcrossing **two sets of data** seperately.

- the 'full' data used for reconstruction
- the 'trigger ' data consisting of 'triggerprimitivs' for event selection



In fig 5 we illustrate schematically , how the front end electronic works to get from electronic signals in a DRIFT TUBE a HIT POSITION. This would be the full data.

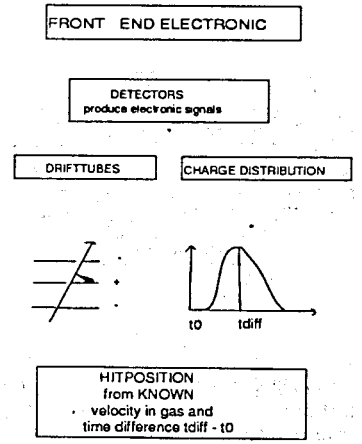


Figure 5: Front end data processing - from signal to hits

On the other hand trigger primitivs are generated , which are also HIT POSITIONS, but in a more coarse and faster way. As we trigger on particles coming from the collision vertex or decaying nearby we use correlations between hits required for tracks coming from the collision vertex.

The trigger data are passed through the LEVEL 1 triggersystem until a decision is taken. The 'full' data rest during this decision time in buffers of the **FRONT END SYSTEM** in a specifically **formatted** way.

If the LEVEL 1 triggersystem **decides** to take the event, the **full data** are moved to **read out units** with dual port memories - which allow a filling of data from one side and a fetching from the other side by the next process step.

Read out units just hold small portions of detector data of one event - these parts have to be gathered together. This process of **event building** is initiated by the Higher Level Trigger system, which fetches these parts gradually from the readout units and puts them physically together via a **switching network.** The **FILTERING PROCESS** starts, eg algorithms running on **computer farms** try to seperate uninteresting events even using only a small amount of the full event data - which now include also trackerdata - , reveal **signal events** and reduce the data produced in the collisions to a manageable rate of 100 Hz for permanent storage.

As trigger and data acquisiton systems **(DAQ)** are closely connected we also speak of the **CMS TRIDAS SYSTEM .** In fig 6 the **hard ware structure** and in fig 7 the **data flow** in the system is shown as it was described above.

At the moment there is a bottle neck in the **switching process.** There we have to connect several nodes ( readoutunits ) with nodes holding complete data of an event. In fig 8 we show

# CMS data acquisition basic structure

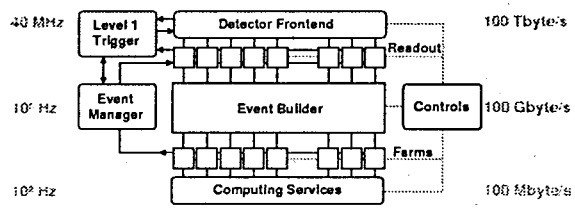


| | |
|---|---|
| Collision rate | 40 MHz |
| Level-1 Maximum trigger rate | 100 kHz |
| Average event size | ≈ 1 Mbyte |
| No. of In-Out units (200-5000 byte/event) | 1000 |
| Event builder (512-512 switch) bandwidth | ≈ 500 Gbit/s |
| Event filter computing power | ≈ 5 $10^6$ MIPS |
| Data production | ≈ Tbyte/day |
| No. of readout crates | ≈ 250 |
| No. of electronics boards | ≈ 10000 |

Figure 6: Hardware structure of the CMS DAQ system



# CMS trigger and data acquisition

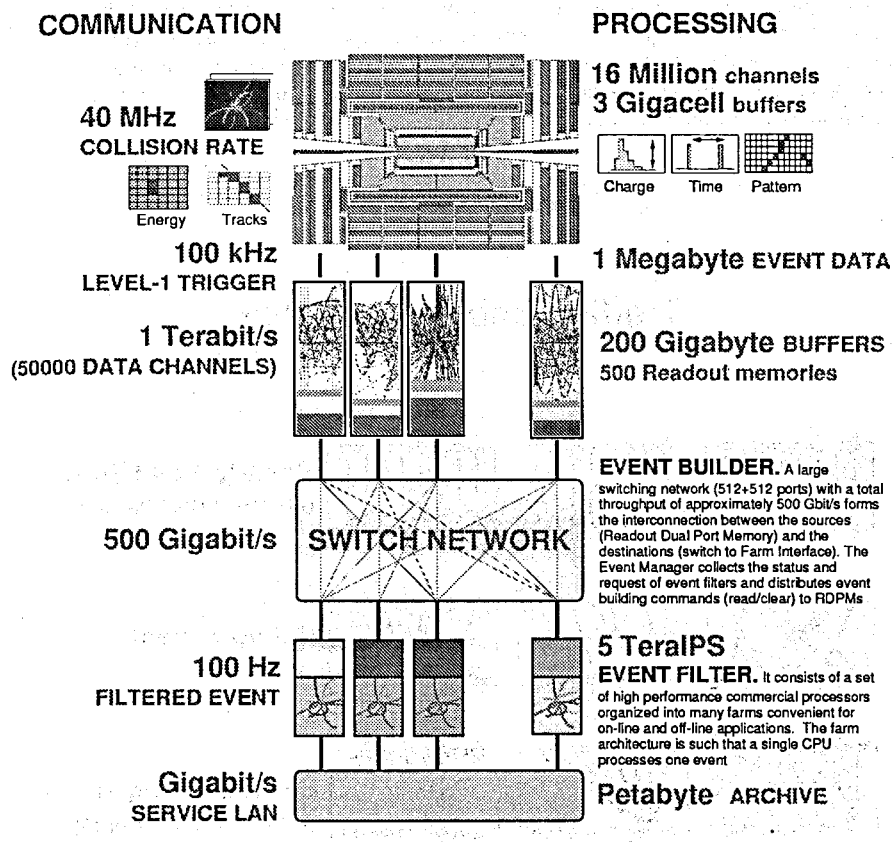


Figure 7: DATAFLOW in the CMS DAQ System

Tera : $10^{12}$; Peta $10^{15}$; IPS : Instruction Per Second; LAN : Local Area Network

several possibilities to connect nodes and the respective traffic lines. If we always connect fixed points or distribute data only from one point, the 'switching' system is fast. If we switch crosswise timing problems arise. At the moment systems of 8 * 8 nodes are tested with the capability of 120 MB/sec. But 1000 * 1000 nodes are foreseen. Several models of data flow are under investigation as to avoid overfloding of the HLT computing devices. At the moment also computing and filtering is tried in steps, where only a small part of data of an event is used for calculations and gradually more data are included and events rejected. This process on the other hand requires big administratitive overhead by an **event manager** to keep record which data are already transferred or waiting.

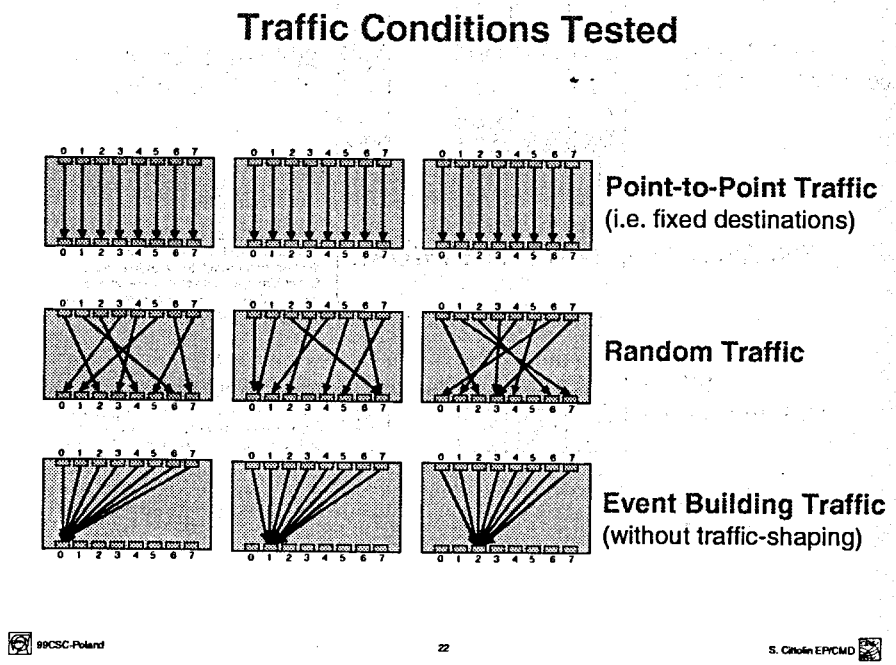


Figure 8: SWITCHING PROCESSES



# 10 LOCAL TRIGGERS of the FIRST LEVEL TRIGGERING SYSTEM

Having described general triggering considerations we outline the **functionality** of the **TWO MAIN COMPONENTS** of the CMS LEVEL 1 TRIGGERING system - the **MUON and CALORIMETER TRIGGERSYSTEM**

## 10.1 MUON TRIGGERSYSTEM

As muons (should) have a very **clean signature** and are therefore 'easy' to identify they have been chosen as triggerobjects. They are a good signal for interesting physics objects, especially with high $p_T$.

As seen from the collision point the muon system is the outmost detector system of CMS. The iron yoke together with the ECAL and HCAL should shield primary hadrons and electrons/$\gamma$s from the muon system. Nevertheless hadrons can 'punchthrough ' to the muon system with a certain probality, which has been studied some time ago. Some problems also arise since muons can stimulate electromagnetic showers in the iron giving fake triggers.

The **task** of the **MUON TRIGGERSYSTEM** is

- to reconstruct muon tracks fast, but coarsly
- measure their $p_t$, $\eta$ and $\phi$
- provide bunch crossing identification
- prepare trigger output to be able to
  - set thresholds and correlations
  - support the elimination of b,c decays at high luminosities
  - reduce high rates of uninteresting events
  - work with the calorimeter system for muon identification
  - enhance together with the tracking system the $p_t$ resolution

The main **sources of muons** and the **CMS detector response** are shown in fig 9. A $p_t$ **threshold** of around **30 GeV/c** is necessary to reach a **design rate** of less than **100 KHZ**. On the other hand muons need a $p_t$ **of at least 6 GeV/c** to even reach the muon system.

## 10.2 Components of the MUON TRIGGERSYSTEM

The MUON TRIGGERSYSTEM uses 3 **different detectortypes** working independently. The layout of the system is shown in fig 10.

This design has been chosen for redundancy reasons - as a non working or not efficient trigger could spoil the experiment. We will see, that this strategy improves the overall efficiency quite drastically when the data are combined in the **global muon trigger** .

## Muon Sources

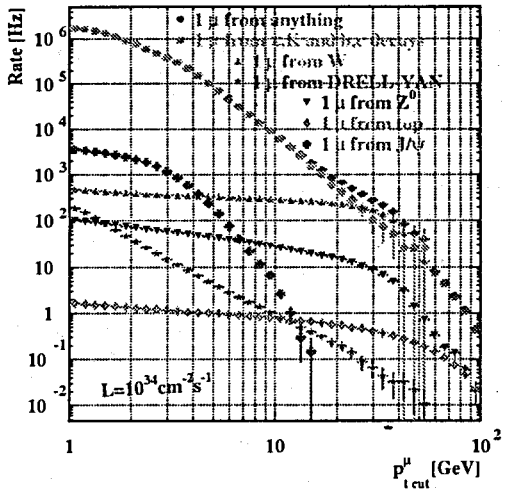


The rate is dominated by π,K decays up to 4 GeV and by b-,c-quark decays from 4 to 25 GeV.

The trigger rate can be adjusted by moving the threshold in a wide range of $p_t$ without loosing much efficiency for heavier objects.

Two muon event rates are 2 orders of magnitude lower.

## Muon Trigger rates

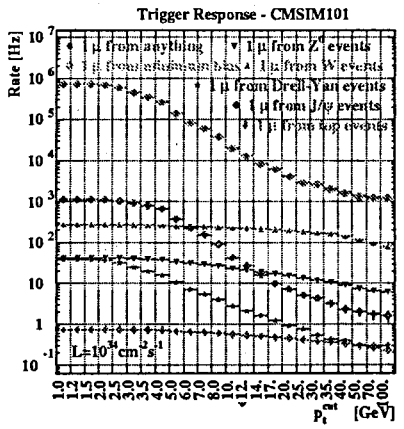


Figure 9: TRIGGER RATES and TRIGGER RESPONSE



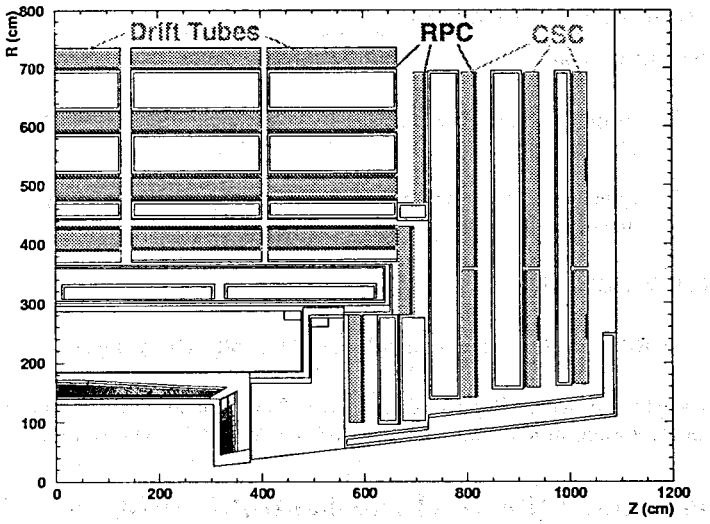


Figure 10: Layout of the muon trigger system

The trigger data come from the

**BARREL region**

- Drifttubes and RPCs radially organised in 4 stations ( = 4 HITS) interspersed in the iron yoke
- segmented in the bending $\phi$ direction in 12 sectors and along the beam axis ($\eta$ ) in 5 wheels

**FORWARD region**

- RPCs and CSCs in 3 stations ( = 3 HITS ) segmented in $\eta$ and $\phi$

The RPC hardware will provide trigger data faster than the Drifttubes and CSCs.The algorithms for track reconstruction are basically different for RPC and Drifttubes/CSCs .

## 10.3 REQUIREMENTS for the MUON TRIGGER SYSTEM

The basic requirements for the muon trigger system comprise

- no latency - eg no dead time loss
- high geometrical coverage and efficiency up to $|\eta| < 2.4$
- good multimuon resolution
- suppression of 'ghost triggers' due to the left-right ambiguity and spurious hits in the DT/CSC system and the ambiguity of patterns in the RPC system
- good and constant $p_t$ resolution of the whole $p_t$ range
- sharp turn on curves for trigger selectivity
- rate restriction to < 15 Khz at high luminosity at Level 1 as a safety margin from the nominal required restriction to 100 Khz equally distributed to the muon and calorimeter system

## 10.4 Structure of the MUON TRIGGER SYSTEM

In fig 11 we show the information and logical structure of the muon triggersystem. Hits from the RPC, DT and CSC are converted to **TRIGGEROBJECTS** like $p_t$, $\phi$ , $\eta$ and a 'quality'.

The DT and CSC systems will provide parts of tracks ( tracksegments) from their local detectors - eg the muonstations - which are grouped to detector regions - and are gathered together to form tracks. Each of the three systems will deliver independently after some filtering processes at **most four tracks.** The **global muon trigger** reduce them to give as **TRIGGER OUTPUT** from the **MUON TRIGGER SYSTEM** not more than **4 tracks and their parameters** serving as input for the **GLOBAL TRIGGER DECISION.**



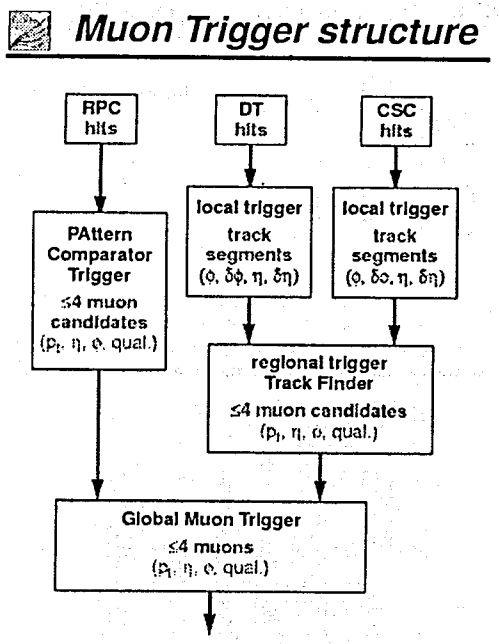


Figure 11: Logical layout of the muon trigger system

### 10.4.1 RPC TRIGGERSYSTEM

In the RPC system the strategy of track reconstruction is based on patternrecognition of hits in the RPC strips. Real hitpatterns are compared with precompiled patterns from simulated tracks stored in look up tables . Valid patterns are selected and the corresponding $\phi$ and $p_t$ values assigned ( fig 12)

### 10.4.2 DT and CSC TRIGGERSYSTEMs

The CSC and DT trigger systems work with a different reconstruction method. Both systems have to cope with inherent ambiguities of the detector data. In fig 13 we see that for the DT system a muon station is comprised of 2 Superlayers (SL) of 4 DT planes each. A particle passing through initiates charges in the DT gas which reach the signalwires in the DT cells. It is not clear from the hit position, wether a particle passed by on the left or right side of the signalwire. But with a 'meantimer' technique using 3 or 4 hits from 1 SL to form a track and assuming the collision point as trackorigin we can restrict these uncertainties. If one can in addition correlate track parts in both SL of a muon station a reconstructed track is rather

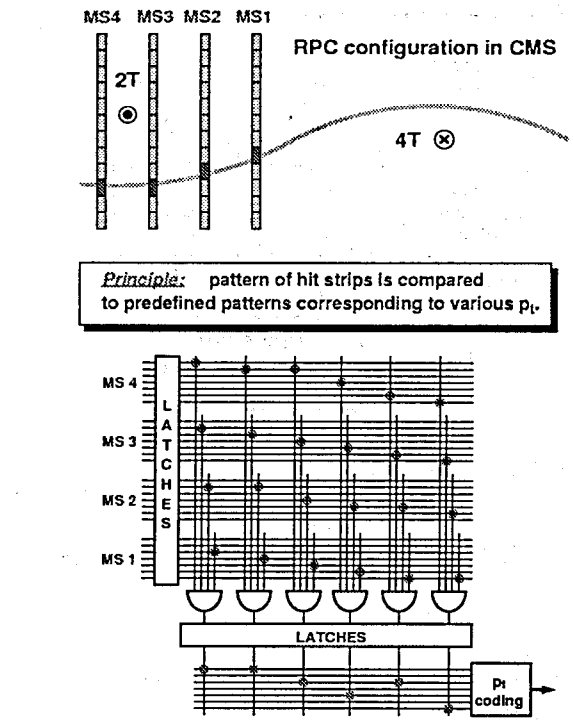


Figure 12: RPC TRIGGER LOGIC



credible. Despite combinatorics we allow only two track candidates per station. The DT system works in the bending plane ($\phi$).

The CSC system has its chambers normal to the beamdirection. Here charges produced in the chamber gas drift to cathode strips for the $\phi$ coordinate, but also to wires for $\eta$ information to have good space resolution in a changing magnetfield in this detectorpart. One CSC chamber has 6 layers and at least 3 hits are required for track reconstruction. The hit location is calculated by 'comparators' of 3 adjacent strips.

Both systems will provide the position and in addition the trackdirection $\phi_b$ ( from some track-points).

TRACKFINDING

These **'locally'** found hits are **'assembled'** to tracks in a certainn $\phi$ **region** - 30 degrees for the DT (fig 14). From the known position $\phi$ and the bending angle $\phi_b$ an **extrapolated hitposition** in the next station can be calculated via lookup tables and compared with a real hitposition found there.

All valid extrapolations between 2 stations are put together to form track candidates which are filtered down to at most 2 tracks per 'region'.

Finally a $p_t$ value is assigned from the $\phi$ differences between hits of different stations.

For the CSCs a rather precise $\eta$ value exists, which can be found for the DT by using the third coordinate of a muon station.

The technical realisation has been studied by a hardware ( VHDL) simulation, were these described tasks are simulated for parallel electronic components.

### 10.4.3 Global Muon Trigger

The global muon trigger will select the **four best - highest $p_t$ - muons** from the complementary barrel DT/RPC and CSC/RPC forward muon system. But the DT and RPC systems of the barrel have comparable efficiencies only for $/\eta/ < 0.8$. In this region we can combine the data of both systems by comparing the muon candidates found by the respective detectors in $\eta$ and $\phi$ to identify the same muons in both systems via a weighting procedure and to select the best muons which are present only in one system.

The effect is a substantial increase of the global efficiency and a smoothing of losses in the $\phi$ and $\eta$ coordinate ( fig 16 and fig 15).

The losses in $\eta$ around 0.2, 0.6 and 0.9 come from the detector construction in beam direction ( 3 parts) and the regular 'holes' every 30 degrees in $\phi$ from the construction of the muon chambers in 12 parts .

A specific problem is the overlap region between barrel and forward, where only a combination of the respective detectors can provide sufficient efficiency. The efficiency of the barrel muon system drops for $/\eta/ > 0.9$ because for tracks with a bigger incident angle not enough detector hits are available. Therefore the data of 2 muon stations (ME13 and ME22 ) in the forward CSC system are included into the barrel system and vice versa to cover sufficiently the region $0.8 < /\eta/ < 1.3$ .

Here a rather difficult data exchange on the hardwarelevel is necessary. Main consideration are dataformats and timing problems and the necessity to avoid 'double ' muon reconstruction by the barrel and forward muon trigger systems.

The geometrical situation is shown in fig 17. Then we show, how the efficiency in $\eta$ would behave if we

- use the barrel and fw muon system with no additional exchanged information from the complementary system
- with data exchange between the 2 complementary systems
- if 1 chamber from CSC would not be added

## 10.5 CALORIMETER TRIGGER

The calorimeter trigger should identify and measure

- total and missing transverse energy $E_t$, $E_t^{miss}$, AND the components $E_x$, $E_y$
- $E_t$ of electron/$\gamma$s
- $E_t$ of single hadrons
- $E_t$ of jets
- $E_t$ of $\tau$ jets

for $|\eta| < 3$ with a desirable extension to $|\eta| < 4.5$ to increase the $E_t$ resolution.

In addition we measure '**isolation** ' of a hadron or electron/$\gamma$ - eg look if there is no other particle activity in its near neighborhood. A b quark and W decay could therefore be discriminated. **Minimum ionisation** - eg an energy deposit compatible with a minimum ionising particle - is checked and combined with the data from the muon trigger system on the level of the global trigger to support muon identification.

The whole calorimeter is scanned for 'activities' - **'quiet' regions** are marked with a specific bit.

For triggering purposes ECAL and HCAL are segmented into common 54 $\eta$ * 72 $\phi$ **'TRIGGER TOWERS'** of 0.087 $\eta$ * 0.087 $\phi$ units as basic triggering regions ( fig 18). **Finegraining** is provided since a HCAL TOWER coincides with 4*4 ECAL TOWERS.

### 10.5.1 Electron/Jet finding algorithm

The final identification algorithms are not fixed at the moment yet, but we show two possibilities in fig 19.

**Electron/$\gamma$s** are found with a sliding window technique, where a grid of 3 * 3 towers around a central tower searches over the whole ECAL surface for a maximum. The sum of the ECAL



transverse energy of a 'central tower' and the maximum of four neighbours around it inside the grid is checked against $E_t$ cutoff values to find a 'HIT' and avoid leakage losses. To discriminate against hadrons/jets the longitudinal shower shape in the corresponding HCAL towers and the ratio of deposited HCAL to ECAL $E_t$ must be small . Also the transverse shower size in ECAL has to be narrow - it has to be contained in a double strip of ECAL TOWERS of 0.034 $\eta$ * 0.087 $\phi$ units.

**Jet finding** is performed in rather big grids to avoid leakage and underestimation of jet $E_t$. Various algorithms are under test. The latest developement concerns a search for a 'HIT', where the $E_t$ of a 4 * 4 region of trigger towers is summed in all possible combinations and compared within a 12 * 12 tower region to find a maximum.

**Single hadrons and $\tau$ decays** ( either to electrons or hadrons with a narrow energy deposit) are found by a combination of ECAL and HCAL response.

### 10.5.2 Rates and Efficiencies

In fig 20 we show the triggerrates for **electrons/$\gamma$s** depending on a triggerthreshold in $E_t$. The curves show the effect of the trigger on ratereduction and the purity of the sample by applying several cuts.

In the same figure are **Jet triggerrates** also depending on $E_t$ thresholds for multiple jets .

The aim to reach triggerrates less than 100 KHz lead to rather **high** $E_t$ thresholds.

The **selectivity** of triggers is demonstrated with **turn on ( efficiency)** curves for electrons and jets in fig 21.

**Electrons** from **topdecays** need at least 40 GeV/c to be detected with 100 % efficiency.

The **turn on curves for jets** show the efficiency to find a jet above a fixed $E_t$ versus the triggered $E_t$ calculated back on generation level. The ideal curves should be stepfunctions, instead the curves are smeared.

For search of **new neutral particles** the $E_t$ **efficiency** is essential. We see in the same figure that full efficiency is only reached for a generated $E_t$ greater than 200 GeV/c.

## 10.6 GLOBAL TRIGGER

The **local muon and calorimeter** trigger systems provide only **'triggerprimitivs'** to identify and measure muons, electrons/$\gamma$s and jets. But the **selectivity** of the trigger and the **rate reductions** are performed by the **'global trigger'**, where certain conditions are set to filter 'interesting' events. It is the ultimate part of the LEVEL 1 TRIGGER and an **accept signal** starts the data transfer from the readoutunits to the HLT system. Clearly physics simulations have been done to study efficient trigger conditions for Higgses, SUSY particles etc.

On the other hand the reduction of muon, electron and jet rates are an important task to handle the produced data of the experiment and avoid overflows in the system.

Technically the global trigger needs to

- synchronize the data of the calorimeter and muon systems as they arrive at different times

- put the physical units of the data of the different systems into the same units. Sometimes they are not even in a linear scale
- provide the possibility of a flexible algorithms scheme which can be used and changed easily

In total **128 TRIGGER ALGORITHMS** are foreseen, out of which **64** are for pure physics purposes and 64 for calibrations and technical checks.

All 64 TRIGGERALGORITHMS run in PARALLEL, but it is possible - via a mask - to use all or only part of them to create a 'LEVEL 1 TRIGGER accept'.

A **TRIGGERALGORITHM** is composed of a

- **logical OR of up to 8 general AND conditions**

An **AND** condition is a **logical AND of several particle AND conditions.**

A **particle AND condition** relates to a condition of a member inside a **particle group** of at most

- 4 (isolated) electrons/$\gamma$s
- 4 (isolated) jets
- 4 (isolated) MUONS

and a check of total $E_t$ and missing $E_t$ of the event

a **particle AND condition** consists of

- single particle conditions
  - $p_t$, $E_t$ thresholds , $\eta$ and $\phi$ windows
  - for muons conditions on QUIET, minimum ionising and quality bits
- correlation conditions : angle differences between 2 particels, sign patterns

As an **EXAMPLE** we take **H ==> $Z^*$ $Z^*$ ==> 2 $\mu$ 2 jets**

We require :

- 2 opposite sign isolated and minimum ionising $\mu$ with $p_t > 40$ GeV/c
- 2 jets with $E_t > 40$ GeV/c
- $\phi$ angle difference of the $\mu > 60^0$
- $\phi$ angle difference of the jets $> 60^0$



Finally the trigger should **reduce rates.** We aim for 100 Khz, but because of simulation uncertainties we assume a nominal rate of only 30 Khz. They are split equally on the muon and calorimeter system.

In fig 22 we show a realistic example which treshholds can be set so that ultimately we reach this goal by requiring more and more stringent conditions.

# 11 Acknowledgments

I am grateful for the invitation to GOMEL SCHOOL 1999 and enjoyed the stay in pleasant surroundings very much. I also like to thank all people who permitted to borrow transparencies.

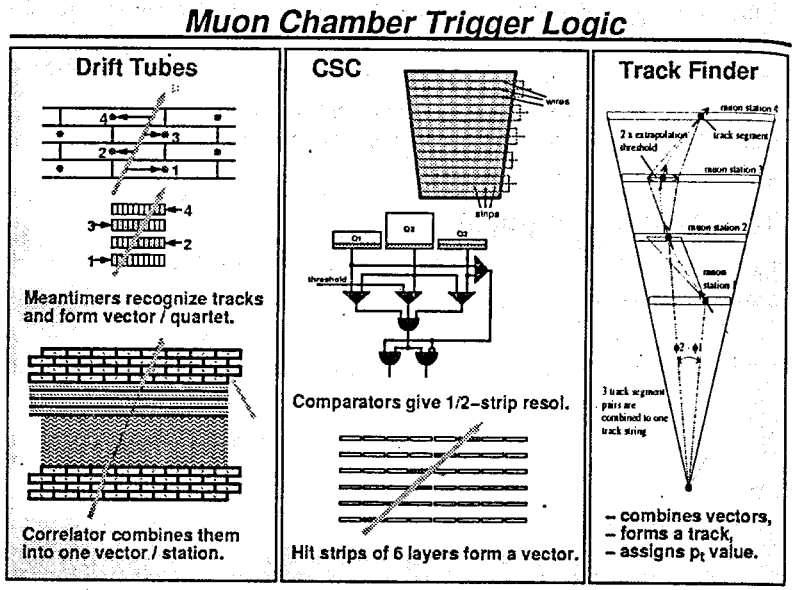


Figure 13: DT and CSC chamber trigger logic



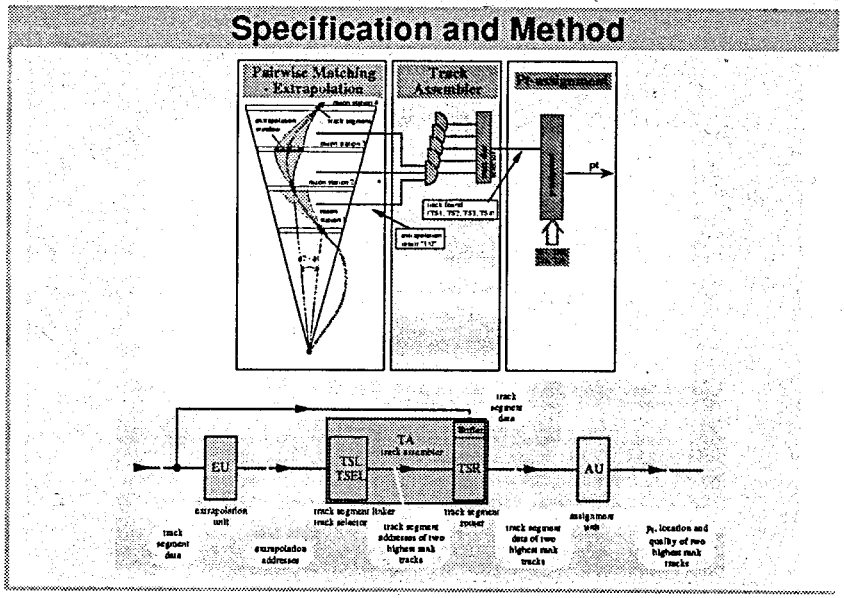


Figure 14: DT TRACKFINDER LAYOUT

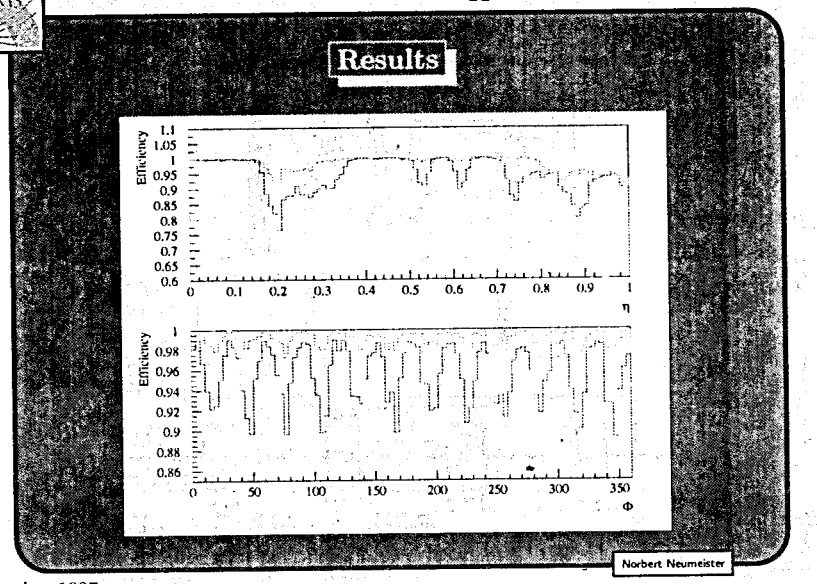




Figure 15: Efficiency of the DT, RPC and Global trigger in $\eta$ and $\phi$



Figure 16: Efficiency of the DT, RPC and Global trigger for 1 $\mu$



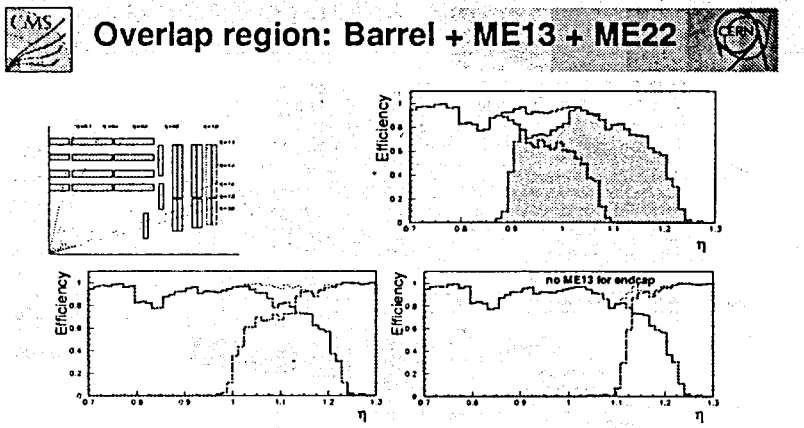




Figure 17: Efficiency for OVERLAP REGIONS of the muon trigger system

# Calorimeter Trigger Geometry

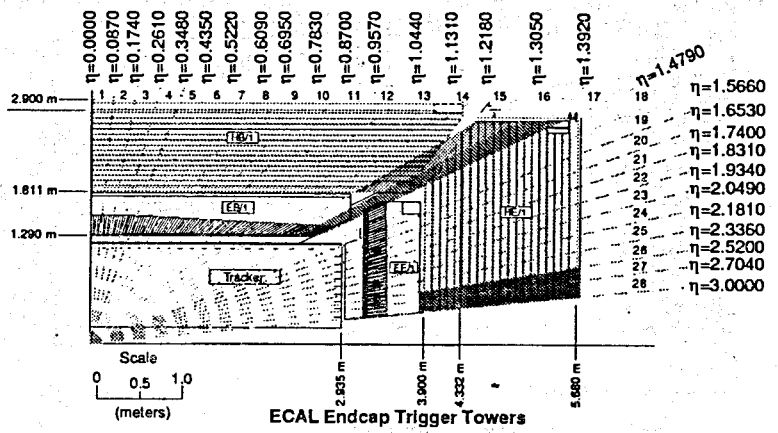


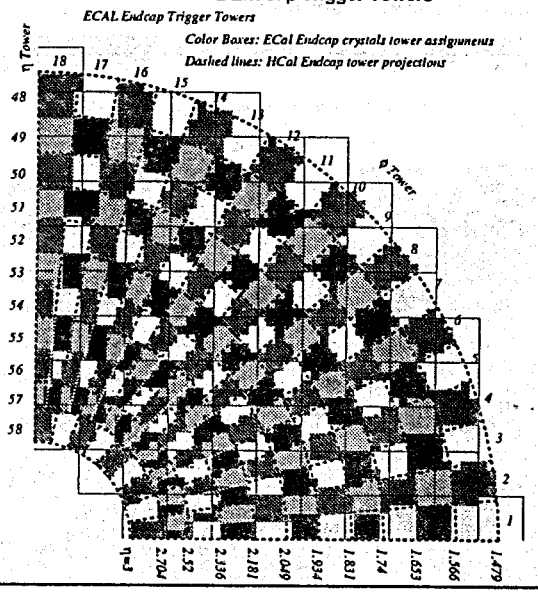




Figure 18: Calorimeter layout in $\eta$ and interdependence of ECAL and HCAL geometry



# Electron-Photon Algorithm

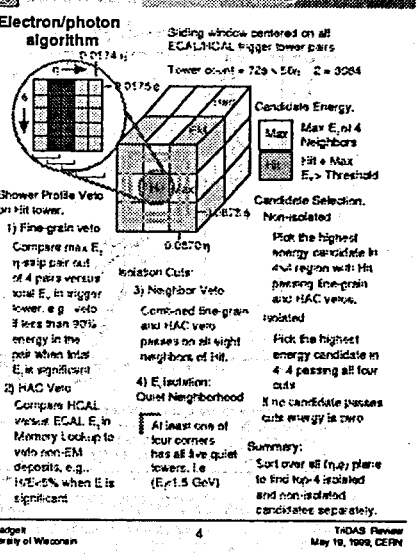




# Jet, Missing $E_T$ Algorithms

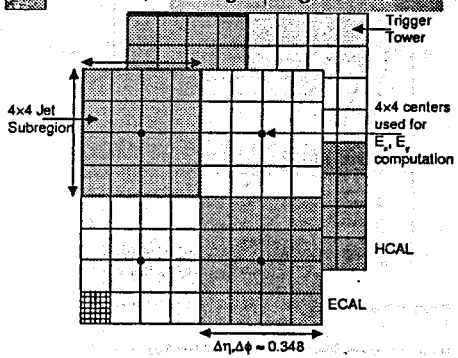


- Jet $E_T$ is given by the sum of ECAL and HCAL trigger tower $E_T$ in a non-overlapping 4x4 subregion
- Jet candidates are sorted to find highest energy jets
- Jet trigger is caused by core of the physical jet. This allows for jet counting without the problems of dealing with multiple jets overlapping in large regions
- $E_x$ and $E_y$ are obtained by a memory lookup using the 4x4 $E_T$
- Signed $E_x$ and $E_y$ sums over the entire calorimeter are made to calculate missing $E_T$



Figure 19: Electron/$\gamma$ and Jetfinding algorithms in ECAL and HCAL

## High Luminosity Rate

Electron/photon trigger rates

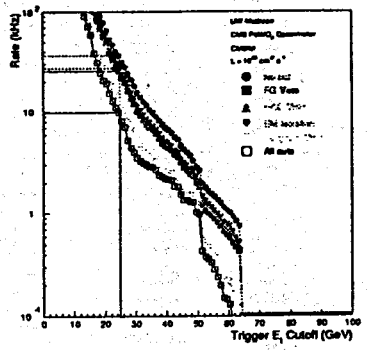


Integrated rate above $E_T$ cut is plotted versus $E_T$ cut.
All four, i.e., finegrain veto, HAC veto, neighbor veto and neighbor $E_T$ veto, cuts are included.
For 25 GeV $E_T$ cut, CMSIM/Pythia QCD rate is 10 kHz.

## Jet trigger rates

Incremental jet trigger rates

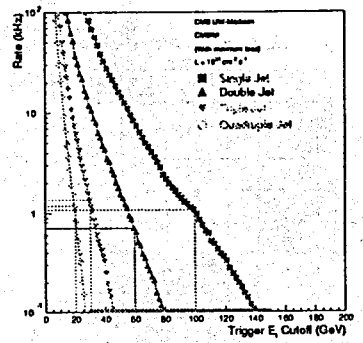


Integrated trigger rate above the trigger $E_T$ cutoff is plotted versus the $E_T$ cutoff

Multijet rates are incrementally over lower multiplicity triggers.

Figure 20: Electron and jet triggerrates



## Electron and Jet efficiencies

Electron/photon algorithm isolec efficiency

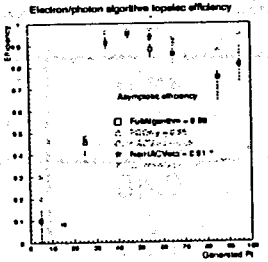


Electron trigger efficiency plotted versus electron $P_T$

Top decays to electron + X

Efficiency of individual cuts and the full algorithm

Efficiencies the same as obtained using CMSIM 111

OCD jet efficiency - 4x4 algorithm

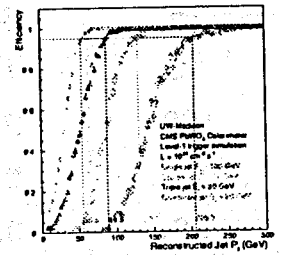


Jet trigger efficiency plotted versus particle level reconstructed jet $P_T$

Cumulative efficiency for multi-jet triggers plotted versus smallest of the reconstructed jet $P_T$

## Missing $E_T$ efficiency

Missing $E_T$ Trigger at $L = 10^{34}$ cm$^{-2}$ s$^{-1}$

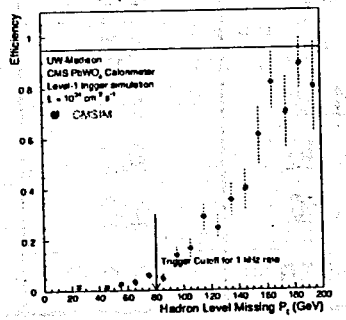


ISAEUS ℓ events - plotted versus generated hadron level missing $E_T$

Figure 21: Triggerefficiencies for electrons, jets and missing e

# Trigger rates at $L=10^{34}$

| trigger type | threshold [GeV] | rate [kHz] | cumulative rate [kHz] |
|---|---|---|---|
| $\Sigma E_t$ | 400 | 0.48 | 0.48 |
| $E_t^{miss}$ | 80 | 1.29 | 1.70 |
| e | 25 | 6.84 | 8.34 |
| e e | 12 | 1.45 | 9.52 |
| j | 100 | 2.06 | 10.7 |
| j j | 60 | 2.17 | 11.6 |
| j j j | 30 | 3.16 | 13.3 |
| j j j j | 20 | 2.96 | 14.3 |
| e j | 12, 50 | 1.35 | 14.9 |
| $\mu$ | 20 | 7.8 | 7.8 |
| $\mu\,\mu$ | 4 | 1.6 | 9.2 |
| $\mu$ e | 4, 8 | 5.5 | 14.4 |
| $\mu$ j | 4, 40 | 0.3 | 14.4 |
| $\mu\ E_t^{miss}$ | 4, 60 | 1.0 | 15.3 |
| $\mu\ \Sigma E_t$ | 4, 250 | 0.2 | 15.3 |

underlined numbers — this study (preliminary results)

Figure 22: Triggersettings and cumulative triggerrates



# Recognition of hard diffractive events with CMS

S.A. Chatrchyan, M.G. Hayrapetyan, S.V. Shmatov
*Joint Institute for Nuclear Research*
*Dubna, Russia.*
L.L. Jenkovszky
*Bogolyubov Institute for Theoretical Physics*
*Kiev, Ukraine*

## Abstract

Studies of hard diffraction in proton and nuclear interactions with CMS is considered. The basic characteristics of these processes and possible detection methods are discussed.

## Introduction.

There exists a wide class of diffractive interactions which differ from the simple elastic scattering or the diffractive excitation of interacting particles. These are events where one or both colliding particles are dissociated or quasi-elastically scattered as well as the production of a "*Central Cluster*" (CC). They are the hard diffractive dissociation or hard Pomeron exchange processes [1] and are characterized by the following properties: a) the beam remnants have a large longitudinal momentum ($x_F \gtrsim 0.9$); b) the bulk of the initial hadron energy is ejected in a narrow volume, "diffractive cone"; c) pseudorapidity interval with an extremely low multiplicity ("rapidity gaps") is observed. Rapidity gaps (RG) are due to the exchange of colorless objects such as photon, gauge bosons and, in particular, the Pomeron [2].

The pronounced features of these diffractive interactions were observed in DIS events [3, 4], jets and $W^{\pm}$ production [5, 6]. The fraction of such events was found to be $\sim 6 \div 7\%$ of $ep$ [4] and $\sim 1\%$ of $p\bar{p}$ interactions [5].

A detailed analysis of the data has shown that hard Pomeron exchange can account for the measurements.

## General structure of hard diffractive events.

In order to study the structure of hard single and double Pomeron exchange processes (SPE and DPE), we have generated $10^6$ events in $pp$, $CaCa$ and $PbPb$ collisions. The general phase space boundaries were determined by the conditions:

$$20\ GeV \leq M_{HS} \leq 200\ GeV, \qquad |Y_{HS}| < 4\,, \tag{1}$$

where $M_{HS}$ is the invariant mass of the produced hard scattering system HS and $|Y_{HS}|$ are the pseudorapidities of the hard system constituents. Also, the additional cutoff in the energy of the detected HS constituents was used:

$$E_{HS} > E_{cut} \geq 40\ GeV, \qquad (2)$$

where $E_{HS}$ is the energy of one of the HS constituents.

In Fig. 1 the specific pseudorapidity distributions of SPE and DPE events in the scattering of protons and $Ca$ and $Pb$ ions are shown.

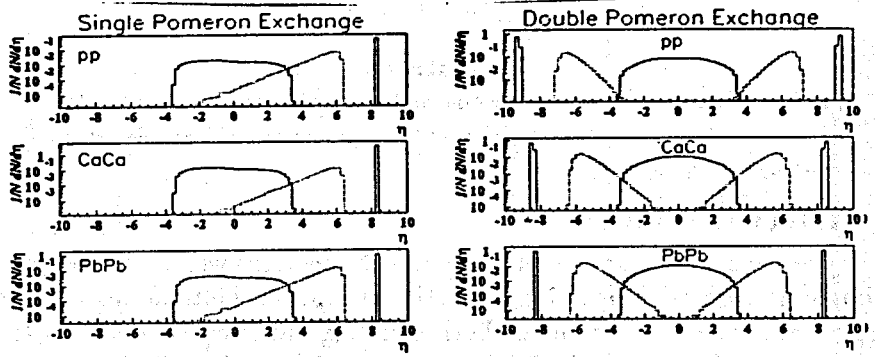


Figure 1. Pseudorapidity distribution of SPE and DPE process participants in $pp$, $CaCa$ and $PbPb$ interactions.

The sharp peaks from the beam remnants are observed at $|\eta| \gtrsim 8$ (solid curves at large pseudorapidities) and become narrower as $A$ increases. Hard system (HS) is produced in the central area $|\eta| \lesssim 4$ (solid curves in the center). The boundaries of area occupied by the central cluster are depicted by dashed curves. Finally, the distance between $Y_{edge}$ the edge of the central cluster and the nearest scattered projectile is a Rapidity Gap.

Due to large acceptance of the CMS, the CC will be covered by detector completly and measurements would be carried out with great accuracy.

## Selection of hard diffractive events.

The selection of diffractive events proceeds in two steps. Large impact parameter, $b \simeq 2R_A$, is triggered on by requiring that the energy measured in the HF calorimeter cells is not higher than a given value $E_{cell}(b)$ [7]. The next step would be one or more of the following methods.

**A. - Define the position of the RG inner edge, $Y_{edge} \equiv \eta_{edge}$, by using "Roman pot" calorimeters or with TOTEM detector.**

For $pp$ interactions, the edge of the rapidity gap is placed at large values of rapidity $Y_{edge} \gtrsim 6.4$, 6.8. In nuclear collisions such as $Pb$, the nuclear



interaction still remains so strong that even at impact parameters $b \simeq 2R_A$, the edge of the gap cannot be determined.

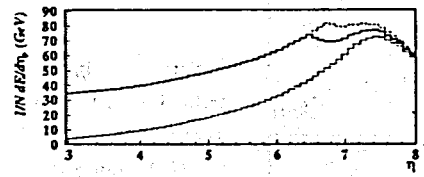


Figure 2. Energy, deposited in calorimeter cells in $pp$ hard (dotted line) and diffractive (dashed line is with applying (1) and solid line is with applying (2) conditions) interactions.

Figure 3. Same as in Fig. 2, but for $CaCa$: (a) $min.bias$ and (b) peripheral $b \simeq 2R_{Ca}$ interactions.

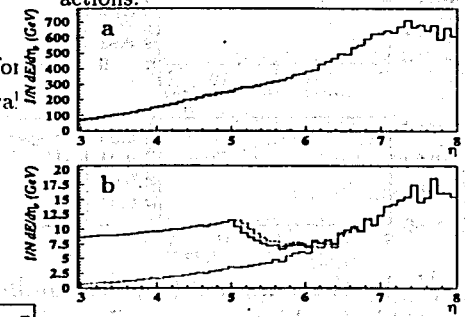


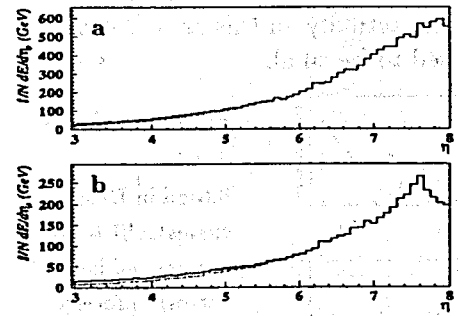


Figure 4. Same as in Fig. 3, but for $PbPb$ interactions.

At larger impact parameters the cross section of Pomeron - induced processes falls sharply. Thus intermediate mass nuclei are preferable for such events.

**B. - Require the central cluster to be separated by large rapidity gaps from the rest of the hadronic final states, protons or products of their dissiciation, the $\eta_{max}$ distribution.**

Each event is assigned a value of $\eta_{max}$ defined as the pseudorapidity of the energy deposit in the calorimeter above some limiting value closest to the appropriate projectile direction. The distribution of $\eta_{max}$ for processes with Pomerons (solid lines) is compared to the expectations for the production of the inelastic hadronic finel states (dashed lines) on Fig. 5. A excess of events with large rapidity gaps will be observed in CMS Barrel.

**C. - Identify the diffractive events as the excess of events filling**

the small mass region $M_{CC}$, in the inclusive $\ln(M_{CC})$ distribution.

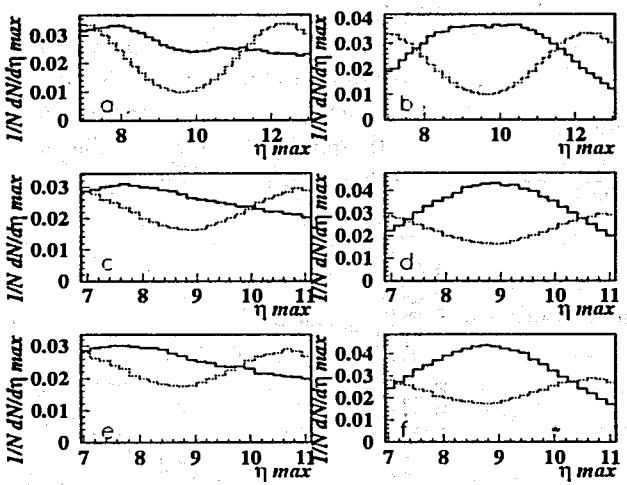


Figure 5. $\eta_{max}$ distribution of the energy above 20 GeV deposited in the calorimeter in SPE (a,c,e) and DPE (b,d,f) processes for $pp$ (a,b), $CaCa$ (c,d) and $PbPb$ (e,f) interactions.

Under the condition (1), the number of events with small $M_{CC}$ is suppressed in hard interactions. Therefore, actually, in this area "hard" background to diffractive events is expected to be small.

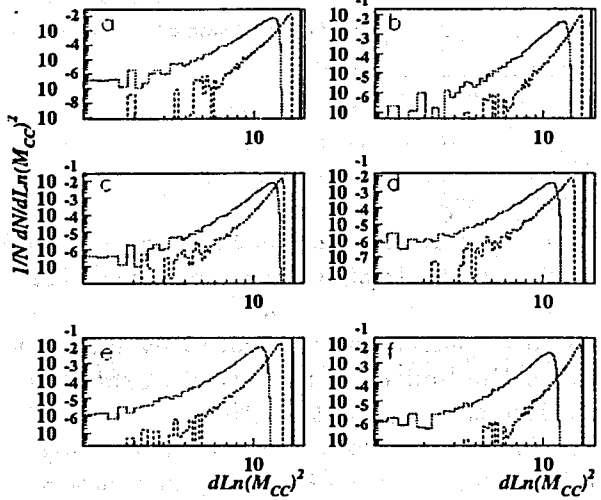


Figure 6. $d\ln(M^2_{CC})$ distribution in DPE (dotted curves), SPE (dashed curves) and hard (solid curves) processes for $pp$ (a,b), $CaCa$ (c,d) and $PbPb$ (e,f) interactions, without (a,c,e) and with (b,d,f) cut off (2). Here, $M_{CC}$ is an invariant mass of CC.

The contribution of DPE is greater than SPE contribution at small $M_{CC}$. Additional cutoff (2) increases the difference between the contributions of SPE and DPE processes (compare a,c,e and b,d,f on Fig. 6).

**D. - Detect the Hard System in the central region.**

A study of the pseudorapidity distributions of heavy quark-antiquark



pairs produced in DPE processes [8], has shown the following. Firstly in the overwhelming majority of cases, the $Q\bar{Q}$ pairs are produced in the area of pseudorapidity covered by the central part of the CMS detector $|\eta| \lesssim 2.5$ (see Fig. 7), namely, in that place of the installation, which has the highest resolution power. Thus the ratio of diffractively produced $Q\bar{Q}$-pairs to hard produced ones reaches its maxima at zero pseudorapidities of both quark and antiquark.

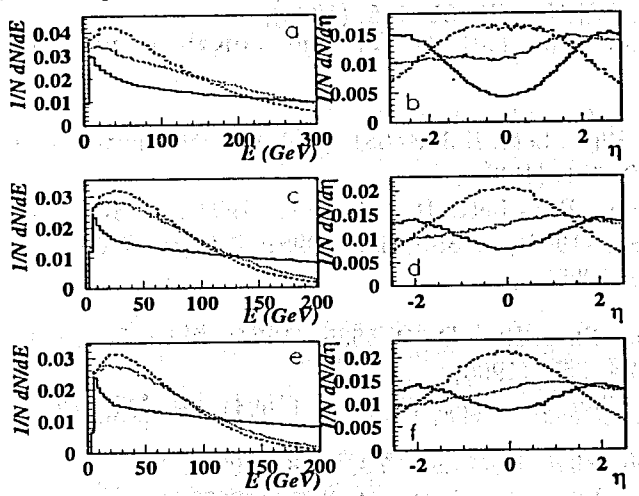


Figure 7. Energy (a,c,e) and pseudorapidity (b,d,f) distribution of HS constituents in $pp$ (a,b), $CaCa$ (c,d) and $PbPb$ (e,f) collisions (for $Q\bar{Q}$ production). Solid curve is for hard scattering, dotted one is for SPE and dashed curve is for DPE.

## Conclusion.

The understanding of strong interactions is incomplete without inclusion of soft and hard diffractive processes. More precise results are needed to improve the understanding of the nature and structure of the Pomeron and distinguish between different theoretical models. There is a rich physics that can be accessed by CMS. The conjugation of TOTEM with CMS will greatly augment the results of these studies.

Finally, we wish to thank the Organizing Committee for the warm hospitality in Gomel.

## References

[1] A.Donnachie, P.Landshoff, Nucl. Phys. B **303**, 634, (1988);
J.D.Bjorken, Int. Jour. Mod. Phys. A **7**, 4189, (1992);
G.Ingelman, P.Schlein, Phys. Lett. B **152**, 256, (1985).

[2] Y.Dokshitzer, V.Khoze, S.Troyan, in *Physics in Collision VI, Proceedings, Chicago, Illinois, 1986*, edited by M.Derrick (World Scientific, Singapore, 1987), 365; Yad. Fiz. **46**, 1220, (1987).

[3] L.Baksay, *et al.* , Phys. Lett. B **61**, 89, (1976);
H. DeKerret *et al.* , Phys. Lett. B **68**, 385, (1977);
R.Waldi *et al.* , Z. Phys. C **18**, 301,(1983);
T.Akesson *et al.* , CERN - EP /85 -115, (1985);
UA8 Collaboration, Phys. Lett. B **211**, 239, (1988); B **297**, 417, (1992).

[4] H1 Collaboration, Phys. Lett. B **348**, 681, (1995); Nucl. Phys. B **429**, 477, (1995); B **439**, 471, (1995);
ZEUS Collaboration, Phys.Lett. B **315**, 481, (1993); B **332**, 228, (1994); B **338**, 483, (1994); B **369**, 55, (1996); Z.Phys. C **65**, 379, (1995); C **68**, 569, (1995).

[5] CDF Collaboration, Phys. Rev. D **50**, 5535, (1994); Phys. Rev. Lett. **69**, 3704, (1992); **74**, 855, (1995);
D0 Collaboration, Phys. Rev. Lett **72**, 2332, (1994); **76**, 734, (1996).

[6] CDF Collaboration, Phys. Rev. Lett. **78**, 2698, (1997);
CDF Collaboration, Phys. Rev. Lett. **79**, 2636, (1997).

[7] V.Kartvelishvily, R.Kvatadze, CMS note 1999/015.

[8] N.M.Agababyan, S.A.Chatrchyan, M.G.Hayrapetyan *et al.* , JINR Rapid Communications, No 5- [91] -98, 47, (1998);
N.M.Agababyan, S.A.Chatrchyan, A.S.Galoyan *et al.* , JINR E2-98-136, (1998); NUCL-TH/9807019;
S.A.Chatrchyan, P.I.Zarubin , in *First CMS Heavy Ion Workshop, Lyon, France, (1996)*; CMS Document 96-122, (1996); in *Second CMS Heavy Ion Workshop, Dubna, Russia, (1997)*; CMS Document 97-011, 291, (1997).



# Electron-pion Ration and $e/h$ for Electromagnetic Compartment of a Combined Calorimeter

**Y.A. Kulchitsky, M.V. Kuzmin**
*Institute of Physics, National Academy of Sciences, Minsk, Belarus*
*& JINR, Dubna, Russia*

**V.B. Vinogradov**
*JINR, Dubna, Russia*

**Abstract**

The method of extraction of the $e/h$ ratio, the degree of non-compensation, of the electromagnetic compartment of the combined calorimeter is suggested. The $e/h$ ratio of $1.74 \pm 0.04$ has been determined on the basis of the 1996 combined calorimeter test beam data. This value agrees with the prediction that $e/h > 1.7$ for this electromagnetic calorimeter.

## 1 Introduction

The existing calorimetric complexes (CDF, D0, H1 etc.) as well as the the future huge ones (ATLAS [1], CMS etc.) at the CERN Large Hadron Collider (LHC) are the combined calorimeters with the electromagnetic and hadronic compartments. For the energy reconstruction and description of the longitudinal development of a hadronic shower it is necessary to know the $e/h$ ratios, the degree of non-compensation, of these calorimeters. As to the ATLAS Tile barrel calorimeter there is the detailed information about the $e/h$ ratio presented in [2], [3], [4], [5], [6]. But as to the liquid argon electromagnetic calorimeter such information practically absent.

The aim of the present work is to develop the method and to determine the value of the $e/h$ ratio of the LAr electromagnetic compartment.

This work has been performed on the basis of the 1996 combined test beam data [7]. Data were taken on the H8 beam of the CERN SPS, with pion and electron beams of 10, 20, 40, 50, 80, 100, 150 and 300 GeV/c.

# 2 The Combined Prototype Calorimeter

The future ATLAS experiment [1] will include in the central ("barrel") region a calorimeter system composed of two separate units: the liquid argon electromagnetic calorimeter (LAr) [8] and the tile iron-scintillating hadronic calorimeter (Tile) [5].

For detailed understanding of performance of the future ATLAS combined calorimeter the combined calorimeter prototype setup has been made consisting of the LAr electromagnetic calorimeter prototype inside the cryostat and downstream the Tile calorimeter prototype as shown in Fig. 1.

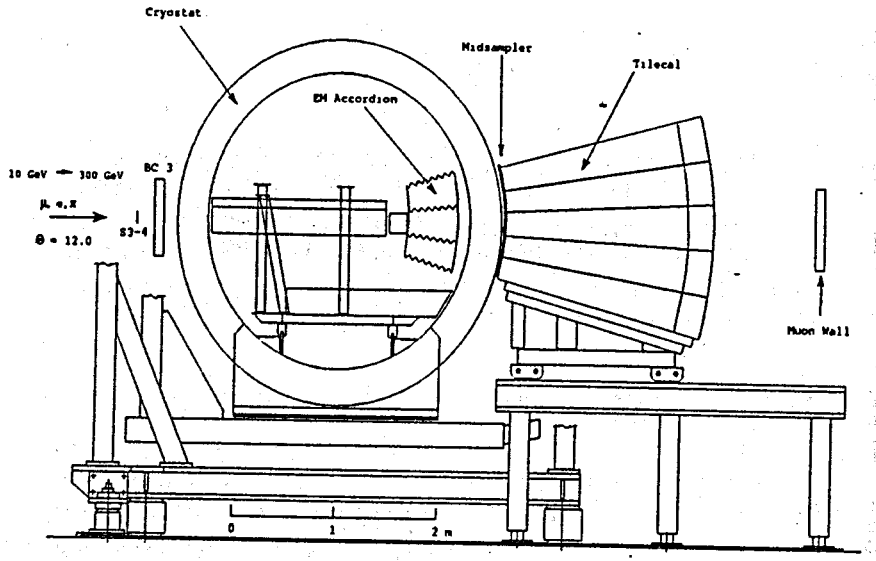


Figure 1: Test beam setup for the ATLAS combined prototype calorimeter.

The dead material between the two calorimeters was about 2.2 $X_0$ or 0.28 $\lambda_I^\pi$. Early showers in the liquid argon were kept to a minimum by placing the light foam material in the cryostat upstream of the calorimeter.

The two calorimeters have been placed with their central axes at an angle to the beam of 12°. At this angle the two calorimeters have an active thickness of 10.3 $\lambda_I$.

Between the active part of the LAr and the Tile detectors a layer of scintillator was installed, called the midsampler. The midsampler consists



of five scintillators, 20 × 100 cm$^2$ each, fastened directly to the front face of the Tile modules. The scintillator is 1 cm thick.

Beam quality and geometry were monitored with a set of beam wire chambers BC1, BC2, BC3 and trigger hodoscopes placed upstream of the LAr cryostat.

To detect punchthrough particles and to measure the effect of longitudinal leakage a "muon wall" consisting of 10 scintillator counters (each 2 cm thick) was located behind the calorimeters at a distance of about 1 metre.

## 2.1 The Electromagnetic Liquid Argon Calorimeter

The electromagnetic LAr calorimeter prototype consists of a stack of three azimuthal modules, each one spanning 9° in azimuth and extending over 2 m along the Z direction. The calorimeter structure is defined by 2.2 mm thick steel-plated lead absorbers, folded to an accordion shape and separated by 3.8 mm gaps, filled with liquid argon. The signals are collected by Kapton electrodes located in the gaps. The calorimeter extends from an inner radius of 131.5 cm to an outer radius of 182.6 cm, representing (at $\eta = 0$) a total of 25 radiation lengths ($X_0$), or 1.22 interaction lengths ($\lambda_I$) for protons. The calorimeter is longitudinally segmented into three compartments of 9 $X_0$, 9 $X_0$ and 7 $X_0$, respectively. More details about this prototype can be found in [1], [9].

In front of the EM calorimeter a presampler was mounted. The active depth of liquid argon in the presampler is 10 mm and the strip spacing is 3.9 mm.

The cryostat has a cylindrical form with 2 m internal diameter, filled with liquid argon, and is made out of a 8 mm thick inner stainless-steel vessel, isolated by 30 cm of low-density foam (Rohacell), itself protected by a 1.2 mm thick aluminum outer wall.

## 2.2 The Hadronic Tile Calorimeter

The hadronic Tile calorimeter is a sampling device using steel as the absorber and scintillating tiles as the active material [5]. The innovative feature of the design is the orientation of the tiles which are placed in planes perpendicular to the Z direction [10]. For a better sampling homogeneity the 3 mm thick scintillators are staggered in the radial direction. The tiles

are separated along Z by 14 mm of steel, giving a steel/scintillator volume ratio of 4.7. Wavelength shifting fibers (WLS) running radially collect light from the tiles at both of their open edges. The hadron calorimeter prototype consists of an azimuthal stack of five modules. Each module covers $2\pi/64$ in azimuth and extends 1 m along the Z direction, such that the front face covers $100 \times 20$ cm$^2$. The radial depth, from an inner radius of 200 cm to an outer radius of 380 cm, accounts for 8.9 $\lambda$ at $\eta = 0$ (80.5 $X_0$). Read-out cells are defined by grouping together a bundle of fibers into one photomultiplier (PMT). Each of the 100 cells is read out by two PMTs and is fully projective in azimuth (with $\Delta\phi = 2\pi/64 \approx 0.1$), while the segmentation along the Z axis is made by grouping fibers into read-out cells spanning $\Delta Z = 20$ cm ($\Delta\eta \approx 0.1$) and is therefore not projective Each module is read out in four longitudinal segments (corresponding to about 1.5, 2, 2.5 and 3 $\lambda_I$ at $\eta = 0$). More details of this prototype can be found in [1], [2].

# 3 Event Selection

We applied some similar to [7] cuts to eliminate the non-single track pion events, the beam halo, the events with an interaction before LAr calorimeter, the events with the longitudinal leakage, the electron and muon events. The set of cuts is the following:

- the single-track pion events were selected by requiring the pulse height of the beam scintillation counters and the energy released in the presampler of the electromagnetic calorimeter to be compatible with that for a single particle;
- the beam halo events were removed with appropriate cuts on the horizontal and vertical positions of the incoming track impact point and the space angle with respect to the beam axis as measured with the beam chambers;
- the electron events were removed by the requirement that the energy deposited in the LAr calorimeter is less than 90 % of the beam energy;
- a cut on the total energy rejects incoming muon;



- the events with the obvious longitudinal leakage were removed by requiring of no signal from the punchthrough particles in the muon walls;
- to select the events with the hadronic shower origins in the first sampling of the LAr calorimeter; events with the energy depositions in this sampling compatible with that of a single minimum ionization particle were rejected;
- to select the events with the well developed hadronic showers energy depositions were required to be more than 10 % of the beam energy in the electromagnetic calorimeter and less than 70 % in the hadronic calorimeter.

# 4 The $e/h$ ratio of the LAr Electromagnetic Compartment

The response, $R_h$, of a calorimeter to a hadronic shower is the sum of the contributions from the electromagnetic, $E_e$, and hadronic, $E_h$, parts of the incident energy [11]

$$E = E_e + E_h \ , \tag{1}$$

$$R_h = e \cdot E_e + h \cdot E_h = e \cdot E \cdot (f_{\pi^o} + (h/e) \cdot (1 - f_{\pi^o})) \ , \tag{2}$$

where $e$ ($h$) is the energy independent coefficient of transformation of the electromagnetic (pure hadronic, low-energy hadronic activity) energy to response, $f_{\pi^o} = E_e/E$ is the fraction of electromagnetic energy. From this

$$E = \frac{e}{\pi} \cdot \frac{1}{e} \cdot R_h \ , \tag{3}$$

where

$$\frac{e}{\pi} = \frac{e/h}{1 + (e/h - 1) f_{\pi^o}} \ . \tag{4}$$

In the case of the combined calorimeter the incident beam energy, $E_{beam}$, is deposited into the LAr compartment, $E_{LAr}$, into Tilecal compartment, $E_{Tile}$, and into the dead material between the LAr and Tile calorimeters, $E_{dm}$,

$$E_{beam} = E_{LAr} + E_{Tile} + E_{dm} \ . \tag{5}$$

Using relation (3) the following expression has been obtained:

$$E_{beam} = c_{LAr} \cdot \left(\frac{e}{\pi}\right)_{LAr} \cdot R_{LAr} + c_{Tile} \cdot \left(\frac{e}{\pi}\right)_{Tile} \cdot R_{Tile} + E_{dm} \ , \qquad (6)$$

where $c_{LAr} = 1/e_{LAr}$ and $c_{Tile} = 1/e_{Tile}$. From this expression the value of the $(e/\pi)_{LAr}$ ratio can be obtained

$$\left(\frac{e}{\pi}\right)_{LAr} = \frac{E_{beam} - E_{Tile} - E_{dm}}{c_{LAr} \cdot R_{LAr}} \ , \qquad (7)$$

where

$$E_{Tile} = c_{Tile} \cdot \left(\frac{e}{\pi}\right)_{Tile} \cdot R_{Tile} \qquad (8)$$

is the energy released in the Tile calorimeter.

The $(e/h)_{LAr}$ ratio and

$$f_{\pi^o,LAr} = k_{LAr} \cdot lnE_{beam} \qquad (9)$$

can be inferred from the energy dependent $(e/\pi)_{LAr}$ ratios:

$$\left(\frac{e}{\pi}\right)_{LAr} = \frac{(e/h)_{LAr}}{1 + ((e/h)_{LAr} - 1)f_{\pi^o,LAr}} \ . \qquad (10)$$

We used the value $(e/h)_{Tile} = 1.3$ [4] and the following expression for the electromagnetic fraction of a hadronic shower in the Tilecal calorimeter

$$f_{\pi^o,Tile} = k_{Tile} \cdot lnE_{Tile}. \qquad (11)$$

with $k_{Tile} = 0.11$ [12], [13].

For the $c_{LAr}$ constant the value of 1.1, obtained in [14], [7], was used.

The algorithm for finding the $c_{Tile}$ and $c_{dm}$ constants will be considered in the next section.

# 5 The $c_{Tile}$ Constant

For the determining of the $c_{Tile}$ constant the following procedure was applied. We selected the events which start to shower only in the hadronic calorimeter. To select these events the energies deposited in each sampling of the LAr calorimeter and in the midsampler are required to be compatible



with that of a beam particle. We used the following expression for the normalized hadronic response [11]

$$\frac{R^c_{Tile}}{E_{beam}} = \frac{c_{Tile}}{(e/h)_{Tile}}\left(1 + \left(\left(\frac{e}{h}\right)_{Tile} - 1\right) \cdot (f\pi^0)_{Tile}\right) \ , \qquad (12)$$

where

$$R^c_{Tile} = R_{Tile} + \frac{c_{LAr}}{c_{Tile}} \cdot R_{LAr} \qquad (13)$$

is the Tile calorimeter response corrected on the energy loss in the LAr calorimeter, $f_{\pi^0,Tile}$ is determined by the formula (11).

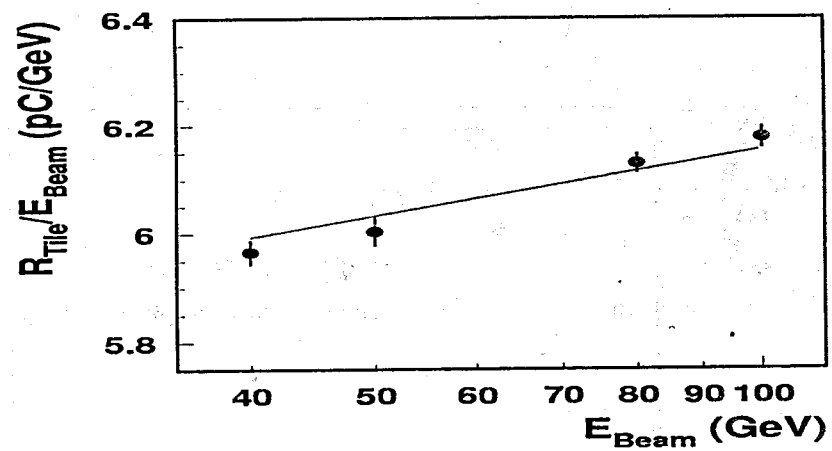


Figure 2: The corrected $R_{Tile}$ response as a function of the beam energy.

The values of $R^c_{Tile}$ are shown in Fig. 2 together with the fitting line. The obtained value of $c_{Tile}$ is equal to $0.145 \pm 0.002$.

# 6 The Energy Loss in the Dead Material

Special attention has been devoted to understanding of the energy loss in the dead material placed between the active part of the LAr and

the Tile detectors. The term, which accounts for the energy loss in the dead material between the LAr and Tile calorimeters, $E_{dm}$, is taken to be proportional to the geometrical mean of the energy released in the last electromagnetic compartment ($E_{LAr,3}$) and the first hadronic compartment ($E_{Tile,1}$)

$$E_{dm} = c_{dm} \cdot \sqrt{E_{LAr,3} \cdot E_{Tile,1}} \qquad (14)$$

similar to [7], [15]. The validity of this approximation has been tested by the Monte Carlo simulation and by the study of the correlation between the energy released in the midsampler and the cryostat energy deposition [7], [16], [17]. We used the value of $c_{dm} = 0.31$. This value has been obtained on the basis of the results of the Monte Carlo simulation performed by I. Efthymiopoulos [18].

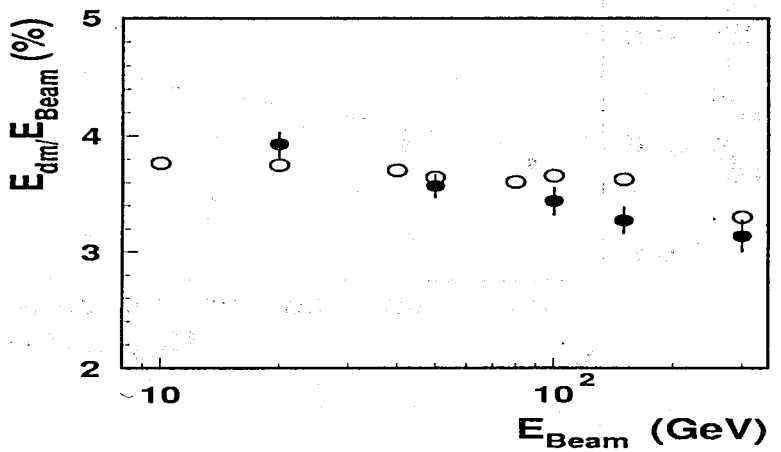


Figure 3: The comparison between the Monte Carlo simulation (solid circles) and the calculated values (open circles) for the average relative energy losses in the dead material, $E_{dm}/E_{beam}$, as a function of the beam energy.

These Monte Carlo (Fluka) results (solid circles) are shown in Fig. 3 together with the values (open circles) obtained by using the expression (14). The reasonable agreement is observed. The average energy loss in



the dead material is equal to about 3.7%. The typical distribution of the energy losses in the dead material between the LAr and Tile calorimeters for the real events at the beam energy of 50 $GeV$, obtained by using Eq. 14, is shown in Fig. 4.

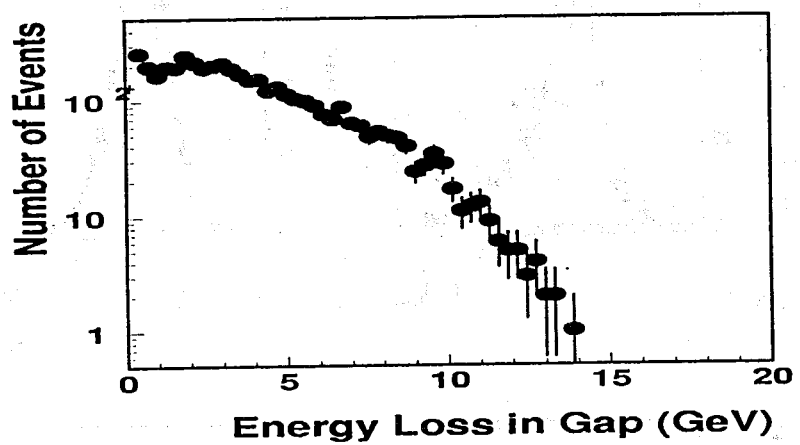


Figure 4: The distribution of energy loss in the dead material for 50 $GeV$ pion beam.

# 7 The $(e/\pi)_{LAr}$ and $(e/h)_{LAr}$ Ratios.

Figs. 5 and 6 show the distributions of the $(e/\pi)_{LAr}$ ratio derived by formula (7) for different energies.

The mean values of these distributions are given in Table 1 and shown in Fig. 7 as a function of the beam energy.

The fit of this distribution by the expression (10) yields $(e/h)_{LAr} = 1.74 \pm 0.04$ and $k_{LAr} = 0.108 \pm 0.004$ ($\chi^2/NDF = 0.93$). For the fixed value of the parameter $k_{LAr} = 0.11$ [12] the result is $(e/h)_{LAr} = 1.77 \pm 0.02$ ($\chi^2/NDF = 0.86$). The quoted errors are the statistical ones obtained

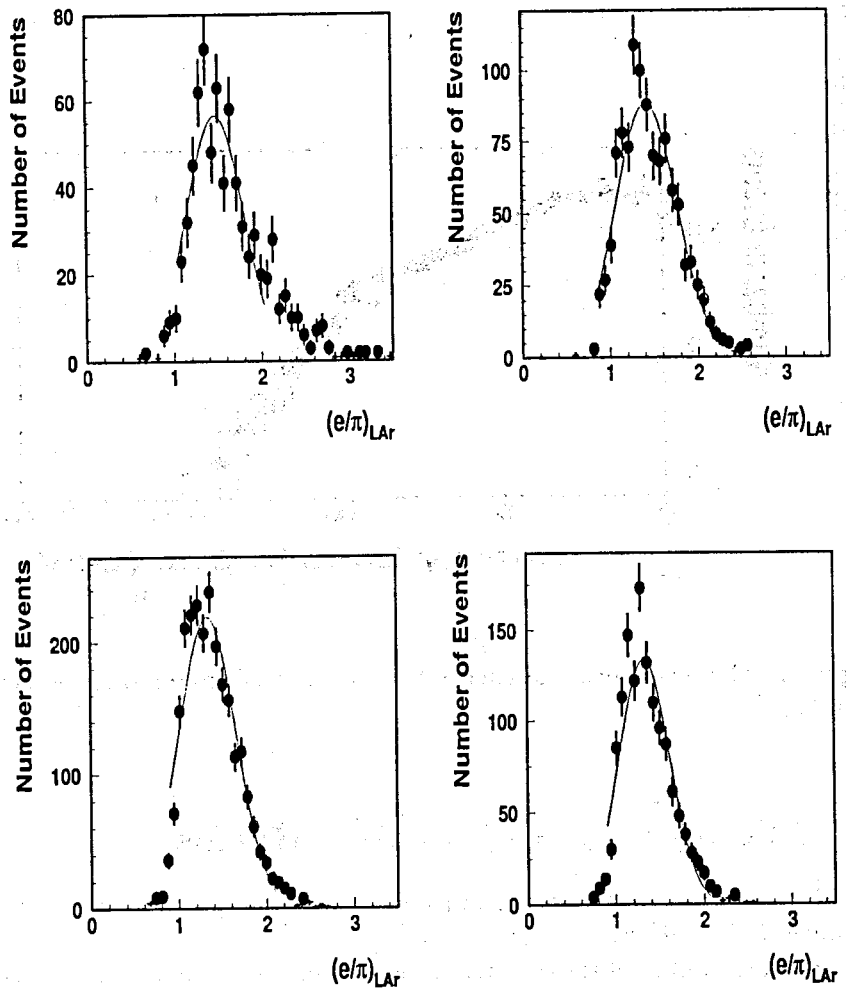


Figure 5: The distributions of the $(\tilde{e}/\pi)_{LAr}$ ratio for $E_{beam}$ = 10, 40 GeV (left column, up to down) and $E_{beam}$ = 20, 50 GeV (right column, up to down).



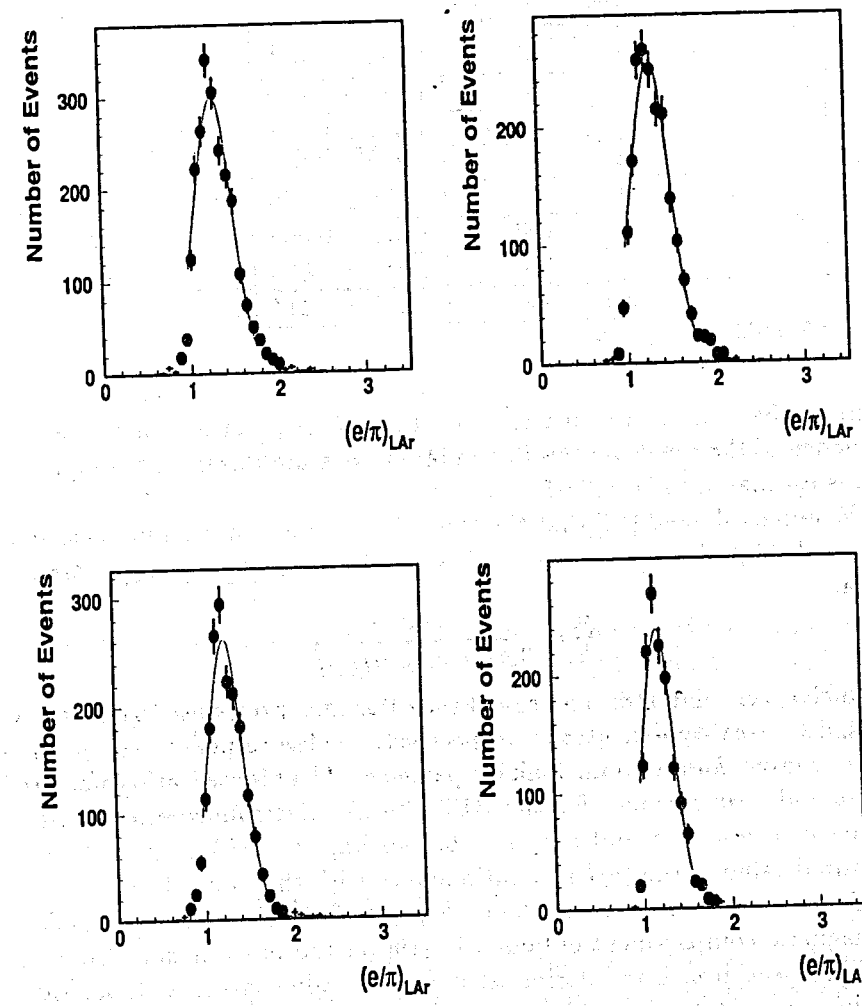


Figure 6: The distributions of the $(e/\pi)_{LAr}$ ratio for $E_{beam}$ = 80, 150 GeV (left column, up to down) and $E_{beam}$ = 100, 300 GeV (right column, up to down).

Table 1: The mean $(e/\pi)_{LAr}$ ratio as a function of the beam energy.

| $E_{beam}(GeV)$ | $(e/\pi)_{LAr}$ |
|---|---|
| 10 | $1.471 \pm 0.025$ |
| 20 | $1.419 \pm 0.015$ |
| 40 | $1.331 \pm 0.017$ |
| 50 | $1.330 \pm 0.019$ |
| 80 | $1.276 \pm 0.010$ |
| 100 | $1.278 \pm 0.009$ |
| 150 | $1.255 \pm 0.009$ |
| 300 | $1.191 \pm 0.014$ |

from the fit. The systematic error on the $(e/h)_{LAr}$ ratio, which is a consequence of the uncertainties in the input constants used in the equation (7), is estimated to be $\pm 0.04$.

Wigmans showed [12] that the the $e/h$ ratio for non-uranium calorimeters with high-Z absorber material is satisfactorily described by the formula:

$$\frac{e}{h} = \frac{e/mip}{0.41 + 0.12\ n/mip} \tag{15}$$

in which $e/mip$ and $n/mip$ represent the calorimeter response to e.m. showers and to MeV-type neutrons, respectively. These responses are normalized to the one for minimum ionizing particles. The Monte Carlo calculated $e/mip$ and $n/mip$ values for the RD3 Pb-LAr electromagnetic calorimeter are $e/mip = 0.78$ and $n/mip < 0.5$ leading to $(e/h)_{LAr} > 1.66$. Our measured value of the $(e/h)_{LAr}$ ratio agrees with this prediction.

There is the estimation of the $(e/h)_{LAr}$ ratio of $3.7 \pm 1.7$ for this electromagnetic compartment obtained in [19] on the basis of data from the combined lead-iron-LAr calorimeter [20]. This value agrees with our value within errors. But we consider their method as the incorrect one since for the determination of the $(e/\pi)_{LAr}$ ratios the calibration constants are used which have been obtained by minimizing the energy resolution that leads to distortion of the true $(e/\pi)_{LAr}$ ratios.



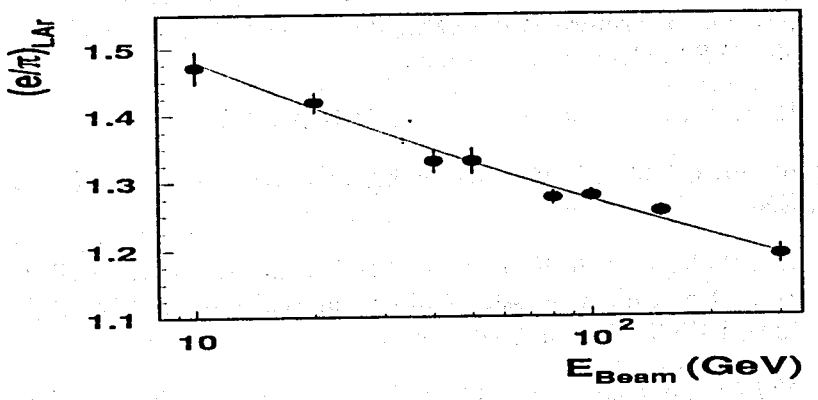


Figure 7: The mean values of the $(e/\pi)_{LAr}$ ratios as a function of the beam energy. The line is the result of a fit of eq. (10).

# 8 Conclusions

The method of extraction of the $e/h$ ratio, the degree of non-compensation, for the electromagnetic compartment of the ATLAS barrel combined prototype calorimeter is suggested. On the basis of the 1996 combined test beam data we have determined this value which turned out to be equal to $1.74 \pm 0.04$ and agrees with the Monte Carlo prediction of Wigmans that $e/h > 1.7$ for this LAr calorimeter.

# 9 Acknowledgments

This work is the result of the efforts of many people from the ATLAS Collaboration. The authors are greatly indebted to all Collaboration for their test beam setup and data taking. Authors are grateful Peter Jenni, Marzio Nessi and Julian Budagov for fruitful discussion and support of this work. We are thankful Illias Efthymiopoulos for giving the results of the Monte Carlo simulation, Irene Vichou and Marina Cobal for constructive advices and fruitful discussion.

# References


[1] ATLAS Collaboration, ATLAS Technical Proposal for a General Purpose pp Experiment at the Large Hadron Collider, CERN/LHCC/94-93, CERN, Geneva, Switzerland.

[2] F. Ariztizabal et al., NIM A349 (1994) 384.

[3] A. Juste, ATLAS Internal note, TILECAL-No-69, 1995, CERN, Geneva, Switzerland.

[4] J.A. Budagov, Y.A. Kulchitsky, V.B. Vinogradov *et al.*, JINR, E1-95-513, 1995, Dubna, Russia; ATLAS Internal note, TILECAL-No-72, 1996, CERN, Geneva, Switzerland.

[5] ATLAS Collaboration, ATLAS TILE Calorimeter Technical Design Report, CERN/LHCC/96-42, ATLAS TDR 3, 1996, CERN, Geneva, Switzerland.

[6] Y.A. Kulchitsky, V.B. Vinogradov, JINR, E1-99-12, 1999, Dubna, Russia; ATL-TILECAL-99-002, 1999, CERN, Geneva, Switzerland.

[7] M. Cobal *et al.*, ATL-TILECAL-98-168, 1998, CERN, Geneva, Switzerland.

[8] ATLAS Collaboration, ATLAS Liquid Argon Calorimeter Technical Design Report, CERN/LHCC/96-41, ATLAS TDR 2, 1996, CERN, Geneva, Switzerland.

[9] D.M. Gingrich *et al.*, (RD3 Collaboration), NIM **A364** (1995) 290.

[10] O. Gildemeister, F. Nessi-Tedaldi and M. Nessi, Proc. 2nd Int. Conf. on Calorimetry in High Energy Physics, Capri, 1991.

[11] D. Groom, Proceedings of the Workshop on Calorimetry for the Supercollides, Tuscaloosa, Alabama, USA, 1989.

[12] R. Wigmans, Proc. 2nd Int. Conf. on Calorimetry in High Energy Physics, Capri, 1991.

[13] D. Acosta *et al.*, NIM A316 (1992) 184.





[14] Y.A. Kulchitsky, M.V. Kuzmin, JINR, E1-98-336, 1998, Dubna, Russia.

[15] Z. Ajaltouni *et al.*, NIM **A387** (1997) 333 – 351.

[16] M. Bosman, Y.A. Kulchitsky, M. Nessi, ATL-COM-TILECAL-99-011, CERN, Geneva, Switzerland.

[17] ATLAS Collaboration, ATLAS Physical Technical Design Report, Volume 1, CERN-LHCC-99-02; ATLAS-TDR-14, CERN, Geneva, Switzerland.

[18] I. Efthymiopoulos, Private communication.

[19] M. Stipcevic, RD3 Note 44, 1993, CERN, Geneva, Switzerland.

[20] D.M. Gingrich *et al.*, [RD3 Collaboration], NIM **A355** (1995) 295.

# $W + jet$ production at LHC – CompHEP, VECBOS and PYTHIA comparison at partonic level

V.A.Ilyin[1] *and* A.N.Skatchkova[2]

**Abstract**

The $W$ boson production recoiled by hard jet at LHC is calculated at partonic level with the help of CompHEP, VECBOS and PYTHIA programs, and obtained results are cross checked. Main goal is to understand the accuracy of the corresponding calculations, in particular at very high transversal momenta. This task should be considered as a basis for the cross check of more complicated cases with $W + Njets$ final states ($N = 2, 3, 4$) which study is crucial for the understanding of the background to several channels for the Higgs boson search and for study of SUSY effects. All three programs have exact matrix elements of the subprocesses. Thus, one can cross check other calculation aspects, in particular the choice of QCD parameters.

Reactions with $W + jets$ production provide important part of physical backgrounds to different standard and, in particular, sypersymmetrical processes at the hadron colliders. We present detailed comparison of the rates at different transversal momenta calculated by CompHEP [1], VECBOS [2] and PYTHIA [3] programs.

Note that $W$ production, associated with two jets, was calculated in [4] at TEVATRON energies with the help of CompHEP and VECBOS. Obtained results were compared, and reasonable agreement was found. In [5] VECBOS and PYTHIA were used for evaluation of $W + Njets$ ($N = 2, 3, 4$) at LHC, and serious underestimating of the rates was fixed for PYTHIA. For example, at moderate transversal momenta (20 GeV) the corresponding ratio VECBOS/PYTHIA was 1.5, and 2.5 at $p_T = 200$ GeV. This is not surprising because of second jet in PYTHIA is simulated by the parton showering mechanism which is an approximation with *ad hoc* unknown applicability at high transversal momenta. However, PYTHIA is a standard tool for simulation of high energy collisions, used widely for LHC processes, for example for search of Higgs boson and SUSY effects.

[1]INP MSU, Moscow
[2]JINR, Dubna



Here large transveral momenta of $W$ boson and jets (up to 500-800 GeV) are of special interest. One can expect that PYTHIA underestimates the rates more seriously at very large $p_T$ than it was observed in [5].

We start our analysis from the $W + jet$ case. Here all three programs have exact (LO QCD) matrix element implemented and one can cross check other calculations conditions. Among them the choice of QCD parameters ($Q^2$ scale of hard subprocess, runing $\alpha_s$ normalization, PDF set) plays the major role. In further reports (to be appear elsewere) we will present next steps of the cross-check: $W + 2jets$ at partonic level, and $W + Njets$ ($N = 1, 2, 3, 4$) with jet simulation through the parton hadronization and subsequent jet reconstruction in CMS detector environment.

Let us give short characteristics of the software used in the calculations.

CompHEP is a program for automatic calculation of cross sections in leading order (LO) of perturbation theory for processes in the Standard Model and its extensions. Matrix elements are calculated symbolically for complete set of Feynman diagrams, and then integrated over the phase spase with the help of adaptive MC program VEGAS [6].

VECBOS is a program for evaluation of $W + Njets$ cross sections (also $Z$ plus up to 3 $jets$) at hadron colliders. It is based on the VEGAS integrator and exact (LO QCD) matrix elements for hard subprocesses. VECBOS was turned out to be an usefull tool for the Tevatron data analysis [9].

PYTHIA is a widely used Monte Carlo physical event generator.

We have used leading order CTEQ4l [7] parametrization for the parton distributions with $\Lambda^{(4)}_{QCD}$ =235 MeV (corresponds to $\Lambda^{(5)}_{QCD}$ =181 MeV) in CompHEP and PYTHIA (where we used the interface with PDFLIB [8]). Here the index at $\Lambda_{QCD}$ parameter means the number of quark flavours. In the VECBOS code the CTEQ4l set is implemented with $\Lambda^{(4)}_{QCD}$ =300 MeV.

In all programs we used fixed strong coupling constant $\alpha_s(M_W)$=0.1345 (corresponds to the LO formula at $\Lambda^{(5)}_{QCD}$ =181 MeV).

The QCD scale $Q^2$ for hard subprocesses and for evolution of parton distributions was chosen equal to $W$ boson mass in CompHEP and VECBOS. In PYTHIA this choice is not available. Thus we used default variant when $Q^2$ equals to average sum of the transversal masses squared for $W$ and $jet$. We have corrected (MSTP(32)=2) this scale by the factor $K = 2M_W^2/(M_W^2 + 2p_T^0)$, where $p_T^0$ is the corresponding cut ($p_T > p_T^0$), to be closer to the fixed scale $Q^2 = M_W^2$.

Physical constants used: $sin\Theta_W$=0.473, $M_W$=80.3427 GeV, $\Gamma_W$=2.10526

GeV, $\alpha_{em}$=1/127.9. Note that the value for $W$ width was obtained as a sum of all 2-body partial widths evaluated in electroweak LO.

**VECBOS at CERN for the CMS experiment**

Current version of VECBOS was copied on the CERN CMS disk space:
**/afs/cern.ch/cms/physics/VECBOS**
Here we placed also some commands and the code of the interface with PYTHIA for hadronization of partonic events generated by VECBOS. VECBOS generator is created by the **VECBOS.make** command. All needed input parameters can be changed in the **INPUT.VECBOS** file. In particular the following PDF sets are available:

- 43 → CTEQ4l , $\Lambda^{(4)}_{QCD}$ = 300 MeV
- 44 → CTEQ4m , $\Lambda^{(4)}_{QCD}$ = 300 MeV
- 130 → CTEQ4m , $\Lambda^{(4)}_{QCD}$ = 215 MeV
- 131 → CTEQ4m , $\Lambda^{(4)}_{QCD}$ = 255 MeV
- 133 → CTEQ4m , $\Lambda^{(4)}_{QCD}$ = 348 MeV
- 134 → CTEQ4m , $\Lambda^{(4)}_{QCD}$ = 401 MeV

In order to start VECBOS generator one has to use **GetPev** command. VECBOS calculation session finishes with:

- cross sections and histograms in the VECBOS.OUT file;
- partonic events in the file VECBOS.pev (in CompHEP format).

**$\Lambda^{N_f}_{QCD}$ in VECBOS**

Strong coupling is evaluated in VECBOS through the well known LO formula $\alpha_s = 12\pi/(33-2N_f)\log(Q^2/\Lambda^2_{QCD})$, but without flavour matching: $\Lambda^{(4)}_{QCD}$ is used for any value of $Q^2$. More correct is to substitute $\Lambda^{(4)}_{QCD}$ on $\Lambda^{(5)}_{QCD}$ when $Q > M_b$, and on $\Lambda^{(6)}_{QCD}$ when $Q > M_{top}$. This is the source for overestimating the $W + jet$ matrix element at the level $\sim 3-4\%$ and (gradually) higher for $W + Njets$.

Also the CTEQ4l set implemented in the VECBOS code is normalized with $\Lambda^{(4)}$ = 300 MeV rather than 235 MeV in "standard" CTEQ4l set. This is the next source for overestimating $(3-4\%)$ the matrix elements in VECBOS.

Furthermore, these two points of different using the $\Lambda_{QCD}$ parameter in VECBOS affect also in the evaluation of parton distributions.

Thus, in our analysis we used two variants of the VECBOS code:
◇ VECBOS$^d$ – with CTEQ4l($\Lambda^{(4)}_{QCD}$ = 300 MeV) and without flavour matching (default code);
◇ VECBOS$^s$ – with CTEQ4l($\Lambda^{(4)}_{QCD}$ = 235 MeV) and flavour matching.



**$W + jet$ final state at partonic level**

Several subprocesses contribute in $W + jet$ final state at the partonic level, which we subdivided on two subsets (in correspondence with the PYTHIA subprocesses 16 and 31):

$$f_i\bar{f}_j \to gW \qquad f_ig \to f_jW$$

where $f_i$ represents quarks of different flavours – $u$, $d$, $c$, $s$ or $b$.

$W$ boson was putted to decay in the $W \to \nu_e e$ channel.

In this paper we do the comparison at partonic level. So, under the jet we understand the parton produced in the hard subprocess. For the jet we used a cut on pseudorapidity $|\eta| < 5$ covering all areas of the CMS detector (including forward HCAL).

Then, we considered the five variants (denoted further as T1, ..., T5) of the cut on the transversal momentum: $p_T > 20$, 50, 200, 400 and 800 GeV.

The resulting cross sections (MC error $\sim 0.7\%$) with percentage rates in terms of CompHEP results are presented in the Tables 1 and 2.

Observed difference between VECBOS$^d$ and CompHEP/PYTHIA at the level 10% at high transversal momenta is explained by the different using the $\Lambda_{QCD}$ parameter discussed above.

Small difference between CompHEP and PYTHIA is caused by slightly different choice of the $Q^2$ scale – fixed in CompHEP ($Q^2 = M^2_W$), and $Q^2 = M^2_W(M^2_W + (p_T)^2)/(M^2_W + (p^0_T)^2)$ in PYTHIA.

Observed difference at the level $\sim 2\%$ between CompHEP and VECBOS$^s$ is caused by the "scalar" treatment in VECBOS of the decay $W \to \nu_e e$, while in CompHEP this decay is treated in terms of "true" $2 \to 3$ Feynman diagrams with Breit-Wigner form of $W$ propagator.

We thank S.Abdullin, E.Boos, M.Cobal, D.Denegri, M.Dittmar, L.Dudko, A.Nikitenko and A.Pukhov for many useful discussions.

# References

[1] A.Pukhov et al, Preprint INP MSU 98-41/542, hep-ph/9908288

[2] F.A.Berends et al, Nucl. Phys. **B357** (1991) 32.

[3] T.Sjostrand, Comp. Phys. Commun. **82** (1994) 74.

[4] A.Belyaev et al, D0 NOTE: 2784, November 1995.

[5] M.Cobal, D.Costanzo and S.Lami, ATLAS Internal Note PHYS-NO-84 April 17, 1996.

[6] G.P.Lepage. J. Comput. Phys. **27** (1978) 192.

[7] H.L.Lai et al, Phys. Rev. **D55** (1997) 1280.

[8] H.Plothow-Besch, Int. J. Mod. Phys. **A10** (1995) 2901.

[9] see e.g.: P.Chang (for the CDF Collaboration), FERMILAB-Conf-99/105-E CDF, April 1999.

| Cut | CompHEP | VECBOS$^s$ | VECBOS$^d$ |
|---|---|---|---|
| T1 | 4.926 | 4.812 (-2.3%) | 5.019 (+1.9%) |
| T2 | 1.171 | 1.145 (-2.2%) | 1.210 (+3.4%) |
| T3 | $2.270 \cdot 10^{-2}$ | $2.190 \cdot 10^{-2}$ (-3.6%) | $2.464 \cdot 10^{-2}$ (+8.5%) |
| T4 | $1.526 \cdot 10^{-3}$ | $1.498 \cdot 10^{-3}$ (-1.8%) | $1.732 \cdot 10^{-3}$ (+13.5%) |
| T5 | $6.620 \cdot 10^{-5}$ | $6.250 \cdot 10^{-5}$ (-5.9%) | $7.393 \cdot 10^{-5}$ (+11.7%) |

Table 1: Partonic $pp \to W + jet$ cross sections (in nb) at different cut on the transversal momentum: CompHEP *vs* VECBOS.

| Cut | CompHEP | PYTHIA 5.7 |
|---|---|---|
| T1 | 4.926 | 4.842 (-1.8%) |
| T2 | 1.171 | 1.151 (-1.7%) |
| T3 | $2.270 \cdot 10^{-2}$ | $2.206 \cdot 10^{-2}$ (-2.9%) |
| T4 | $1.526 \cdot 10^{-3}$ | $1.499 \cdot 10^{-3}$ (-1.7%) |
| T5 | $6.620 \cdot 10^{-5}$ | $6.238 \cdot 10^{-5}$ (-5.8%) |

Table 2: Partonic $pp \to W + jet$ cross sections (in nb) at different cut on the transversal momentum: CompHEP *vs* PYTHIA.



# Low-noise Monolithic Charge Sensitive Preamplifiers ICs for Particle Detectors

*K.Afanasiev, V.Chekhovsky, N.Choumeiko, O.Dvornikov, A.Khomitch, A.Solin, D.Stepankov, F.Zyaziuliya*
*NC PHEP, Minsk, Belarus*
*E-mails: solin@hep.by; tchek@hep.by.*
*I.Golutvin, N.Gorbunov, V.Karjavin, S.Movchan*
*JINR, Dubna, Russia*

Abstract

*A set of large-scale multichannel analog Integrated Circuits has been developed and tested for some types of particle detectors. ASICs were produced using Bi-JFET technology. Examples of low noise, high speed, low power cathode and anode multiwire proportional chambers readout ASICs are shown. Also, results of development of specialized mask programmable analog array are presented. Possibility of development of wide range of multichannel analog ICs for physical experiments based on mask programmable analog array is discussed.*

## 1.Introduction

One of the main features of modern experimental equipment for particle physics is a large number (hundreds and thousands) of data acquisition channels. To create compact data acquisition boards for physical experiments, multichannel integrated circuits are necessary. During the recent years at the National Center of Particle and High Energy physics works has been carried to develop multichannel analog ICs for experimental equipment.

All designs are based on 1.2μm combined microwave Bi-JFET process, which is available from the «Integral» (Minsk, Belarus) production association. Typical structure of bipolar and field effect transistors is shown at the fig. 1. Pspice models of all basic electronic components were developed. These models are used in schematics simulation [1,2].

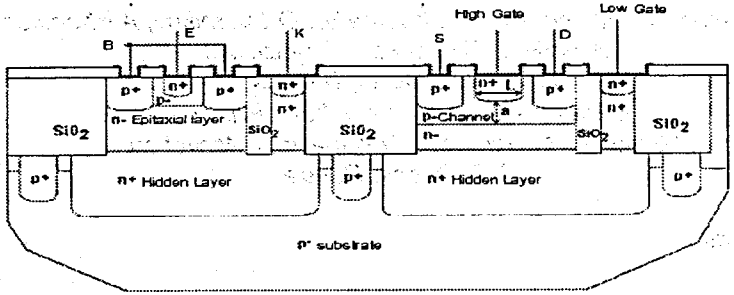


Fig.1. Vertical Section of Single *npn* BJT and *jFET*

As an example of our electronics solutions we present a very forward electronics for the CMS ME1/1 cathode strip chambers (CSC) readout [3,4]. The area of our activity includes only a very front-end chips: charge sensitive preamplifier-shapers for cathode strips readout and charge sensitive preamplifier-shaper-discriminators for anode wires. Our efforts were aimed to meet specific ME1/1 requirements and operational conditions. Chips were designed and tested in co-operation by NC PHEP (Minsk) and JINR (Dubna). All chips were produced by "INTEGRAL" production association.

### *2. Cathode readout*

For cathode readout one of the main task is to provide proper tail cancellation in order to obtain optimal signal-to-noise ratio in presence of high input rates. The gain of ME1/1 cathode amplifier is supposed to be in the range of 4 – 8 mV/fC. The result of R&D is "KATOD-1m" ASIC, which block diagram is shown at fig.2.



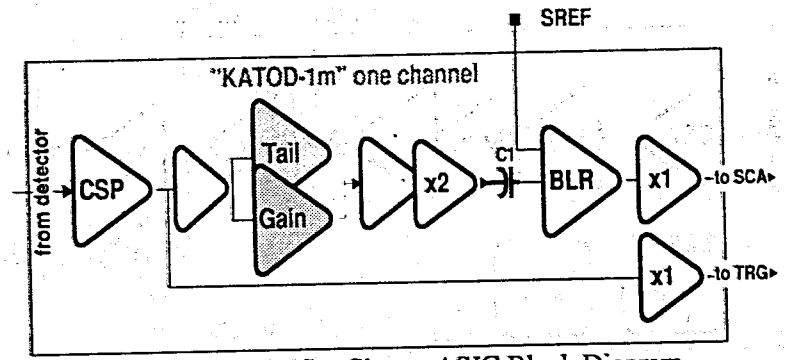


Fig.2. "KATOD-1m" Preamplifier-Shaper ASIC Block Diagram

The main parameters of 16-channel charge sensitive preamplifier–shaper for cathode readout "KATOD-1m" are:

- Peaking time of shaped chamber signal ~150 ns
- Shaper CR-$RC^4$ with Tail Cancellation and Gain Control
- ENC (r.m.s.) ~2400+12 e/pF
- Input Rates up to 1 MHz/channel

The final version of cathode readout ASIC "KATOD" will be based on "KATOD-1m" with additional embedded digital testing, calibrating and control system for each channel. This system consists of 48-bit shift register (3 bits per channel), decoder and a set of analog switches for commutation of test charge from internal 2-bit DAC or external precision charge source. It is also capable of switching on/off every channel on the basis of input code combination.
Block diagram of one channel of "KATOD" IC is shown at fig.3.

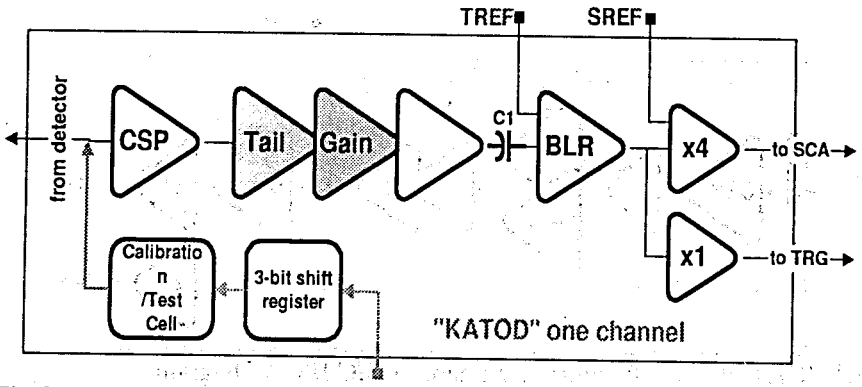


Fig.3. "KATOD" Preamplifier-Shaper ASIC Block Diagram

### *3. Anode readout*

Block diagram of one channel of the "ANOD" ASIC is shown at fig.4.

In order to provide high timing resolution in presence of high input rates and input signal with large dynamic range, tail cancellation circuit with base line restorer and time–over–threshold comparator are employed in the IC for anode readout "ANOD". Optimal threshold for ME1/1 CSC is about 10 fC and gain is 10 mV/fC.

The main parameters of 8-channel charge sensitive preamplifier–shaper-discriminator for anode wire readout "ANOD" are:

- Peaking time ~20 ns
- Shaper CR-RC$^3$ with Tail Cancellation
- ENC (r.m.s.) ~1600+20 e/pF
- Input Rates up to 10 MHz/channel
- LVDS- compatible output



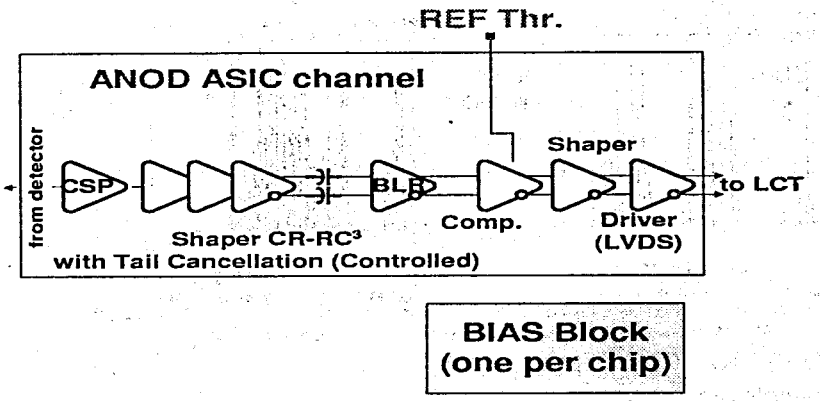


Fig.4. "ANOD" Preamplifier–Shaper-Discriminator ASIC Block Diagram

### *4.Testing and results*

At the figures 5,6 one can see examples of signals from ICs obtained during rate capability test on the prototype of CSC ME1/1. Tests were carried out in JINR (Dubna) on X-ray test setup.

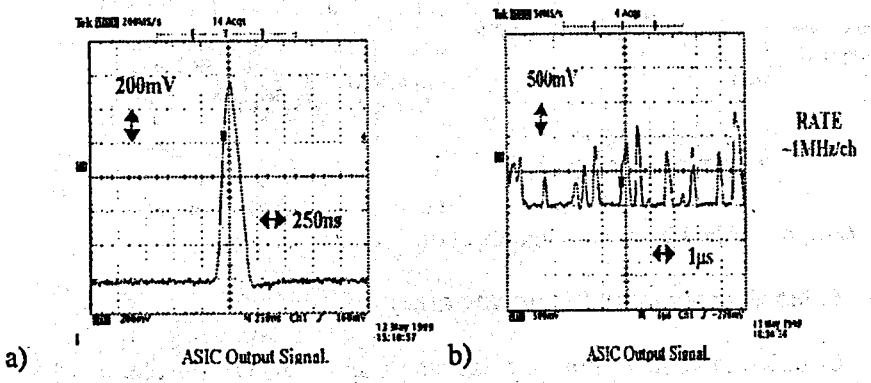

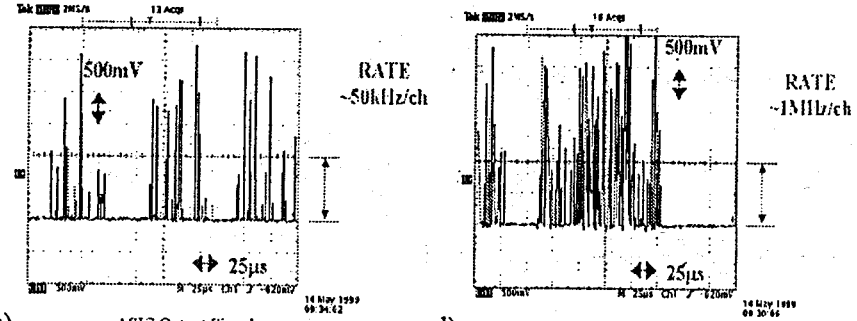


c) ASIC Output Signal. d) ASIC Output Signal.

Fig. 5 (a-d). "KATOD" output signals at:

a) single input pulse;
b) input pulse rate ~1 MHz/ch (sweep time 1 μs/div);
c) input pulse rate ~50 kHz/ch;
d) input pulse rate ~1 MHz/ch (sweep time 25 μs/div).

Shift of output base line not exceeds 40 mV in all cases.

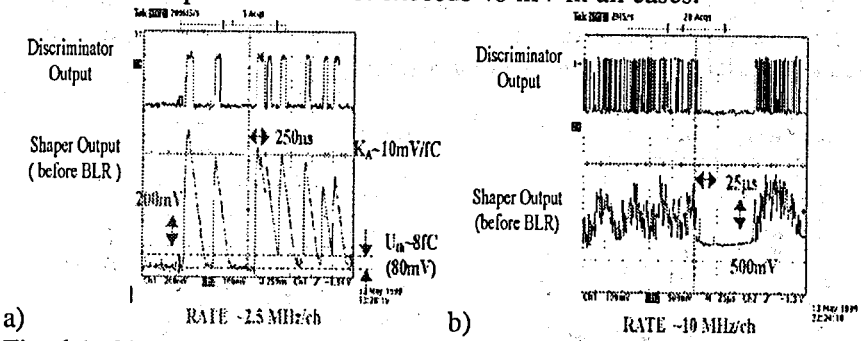


a) RATE ~2.5 MHz/ch b) RATE ~10 MHz/ch

Fig. 6 (a, b). "ANOD" output signals at different input rates.

### *5. Mask programmable analog array*

In order to reduce time and resources spend in the development of custom ICs, mask programmable analog arrays are widely used today.

Such a specialized mask programmable analog array for nuclear electronics applications was developed at NC PHEP. Its design is based on an analysis of most popular schematics for wideband mask programmable analog arrays [1-2,5].



Mask programmable analog array consists of 4 identical channels, which, in turn, consists of two macrocells. Around array core 54 pads are placed. These pads could be used as IC's contact pads or as schematics elements. Mask programmable analog array chip is 2.7X3.6 $mm^2$ in size. One 100 mm wafer can hold up to 650 chips. At fig. 7, 8 are shown the single tile of the mask programmable analog array and a whole chip. We have used mask programmable analog array as base for the following ICs:

Micropower low-noise charge sensitive amplifier
High-speed charge sensitive amplifier-shaper
High-speed comparator
Oscilloscope synchronization IC (for replacement of serial production IC АФ011А)

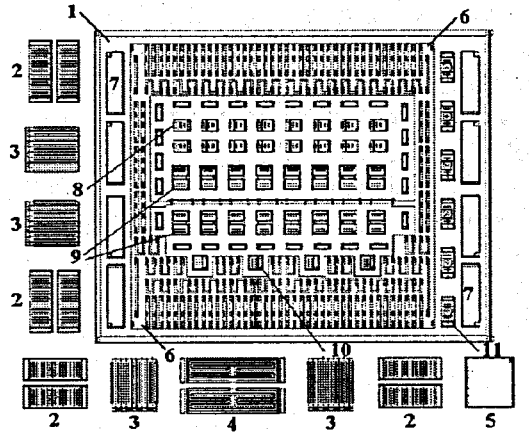


Fig.7. Single tile of the mask programmable analog array

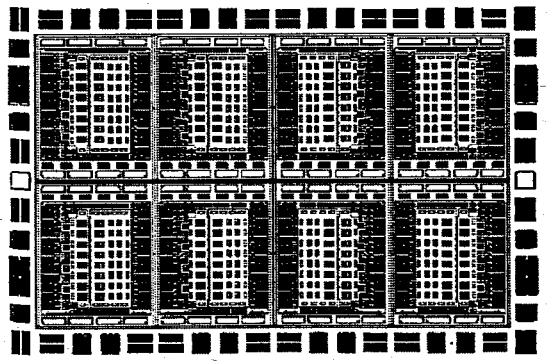

Fig.8. Mask programmable analog array.

### 6.Conclusion

The ICs, showed above, have improved radiation hardness, low noise, highly reproducible parameters, low power consumption and low interchannel crosstalk. They could be used in the design of readout electronics for a wide range of modern particle detectors.

References

1. M.A. Baturitsky, O.V. Dvornikov. Multichannel monolithic front-end system design. Part II, Nucl. Instr. & Meth. A, 378 (1996) p.570-576.

2. M.A. Baturitsky, O.V. Dvornikov. Multichannel monolithic front-end system design. Part I, Nucl. Instr. & Meth. A, 378 (1996) p.564-569.

3. CMS Technical Proposal. CERN/LHCC 94-38, LHCC/P1, 1994.

4. The muon project. TDR. CERN/LHCC 97-32, CMS TDR 3, 1997.

5. Two Low-noise Monolithic Charge Sensitive Preamplifiers IC for Cathode Strip Chambers. V. Chehovsky, O. Dvornikov, I. Emel'yanchik et al. XVII International Symposium on Nuclear Electronics. Varna, 1997 p.82-86.



# QCD Processes

# Multiplicity Distributions Derived From Effective Field Theory Approach To Parton-Hadron Conversion.

V. I. Kashkan

*Institute of Physics, NAS of Belarus*
*Skaryna av.70, Minsk 220072, Belarus*
*e-mail: kashkan@dragon.bas-net.by*

**Abstract**

*In this paper a new Monte-Carlo model for $q\bar{q}$-fragmentation system is constructed on the basis of QCD effective field theory approach proposed by K.Geiger. Factorial moments $F_q$, cumulants $K_q$, and the ratio $H_q = \frac{K_q}{F_q}$ for final state colorless clusters are computed. It appears that Monte-Carlo model gives order of magnitude and oscillating behaviour of experimental $H_q$ though there is no precise fitting. This result may indicate that approach proposed by K.Geiger is a very good hadronization scheme for Monte-Carlo event generators.*

## 1. Introduction.

QCD deals with different objects when different distances are involved. At small distances (less than 1 fm) the relevant degrees of freedom are quarks and gluons, their interaction being well described by perturbative QCD [1]. At large distances we see hadrons and use QCD sum rules and low energy models [2]. But there are no tools to describe dynamics of transition between these different kinematical regions, i.e. dynamics of confinement and hadronization. QCD effective field theory approach proposed by K. Geiger in [3] is designed to fill this gap and has a potential to be developed for systematical description of hadronization. The key element of [3] is Lagrangian accounting for relevant degrees of freedom in each kinematical region, i.e. for quark ($\psi_i$) and gluon ($A_a$) fields in perturbative region ($Q^2 \geq k_\perp^2 \geq Q_0^2$) and quark (U) and gluon ($\chi$) condensate fields in nonperturbative region ($Q_0^2 \geq k_\perp^2 \geq \Lambda^2$). Here $Q^2$ is a hard scale for high-energy process, $k_\perp^2$ is transverse momentum squared, $Q_0$ separates perturbative and nonperturbative domains and $\Lambda$ is

QCD fundamental scale. Dynamics of parton-hadron conversion is described by coupling of quark and gluon fields to gluon condensate field (which drives quark condensate field). I urgently refer reader to [3] for details and in this paper I only look for multiplicity distributions emerging from this approach in $q\bar{q}$-fragmentation (only gluodynamics will be considered).

## 2. Monte-Carlo Model.

In [3] K. Geiger applies his approach to gluodynamics of $q\bar{q}$-fragmentation and shows that perturbative and nonperturbative stages can be treated on the very same footing. Usual for perturbative evolution parton shower description can be applied in the frame of Geiger's approach to nonperturbative evolution. Gluon with momentum $k = (k^+, k^-, \vec{k}_\perp)$ (light cone variables are used) can participate in the following processes: gluon branching ($g \to gg$) at perturbative stage, energy transition from gluon to gluon condensate ($g \to g\chi$) and gluon fusion ($gg \to \chi$) at nonperturbative stage, the whole evolution ending in gluon extinction and cluster formation. The corresponding probabilities are:

$$\omega_{g\to gg}(z, k_\perp^2) = \frac{\alpha_s(k_\perp^2)}{2\pi}\gamma_{g\to gg}(z), \tag{1}$$

$$\omega_{g\to g\chi}(z, k_\perp^2) = \frac{\lambda_\chi(k_\perp^2)}{2\pi}\gamma_{g\to g\chi},(z) \tag{2}$$

$$\omega_{gg\to\chi}(z, k_\perp^2) = \frac{\lambda_\chi(k_\perp^2)}{2\pi}\left(\frac{\Lambda^2}{k_\perp^2}\right)\pi^2 z(1-z)\gamma_{gg\to\chi}(z). \tag{3}$$

Here z is lightcone momentum fraction ($z = \frac{k_2^+}{k_1^+}$ for $1 \to 23$ branching, $z = \frac{k_1^+}{k_3^+}$ for $12 \to 3$ fusion). $\alpha_s(k_\perp^2)$ and $\gamma_{g\to gg}(z)$ are well known strong QCD coupling and splitting function for gluon branching correspondingly. Coupling $\lambda_\chi(k_\perp^2)$ and functions $\gamma_{g\to g\chi}(z)$, $\gamma_{gg\to\chi}(z)$ are:

$$\lambda_\chi(k_\perp^2) = \frac{\theta(Q_0^2 - k_\perp^2)}{4\pi}\frac{ln(Q_0^2/k_\perp^2)}{ln(Q_0^2/\Lambda^2)}, \tag{4}$$



$$\gamma_{g\to g\chi}(z) = \frac{1}{4}\left(\frac{1+z^2}{1-z}\right), \tag{5}$$

$$\gamma_{gg\to\chi}(z) = 8\left(z^2 - z + \frac{1}{2}\right). \tag{6}$$

Monte-Carlo simulation of branching is well defined procedure (see for example [4]). For branching $1 \to 23$ the following kinematics arises:

$$k_2^+ = zk_1^+, \tag{7}$$

$$k_3^+ = (1-z)k_1^+, \tag{8}$$

$$\vec{k}_{\perp 2} = z\vec{k}_{\perp 1} + \vec{p}_\perp, \tag{9}$$

$$\vec{k}_{\perp 3} = (1-z)\vec{k}_{\perp 1} - \vec{p}_\perp, \tag{10}$$

where $\vec{p}_\perp$ is intrinsic transverse momentum for branching,

$$p_\perp^2 = z(1-z)k_1^2 - (1-z)k_2^2 - zk_3^2. \tag{11}$$

I employed constrained evolution scheme, invariant mass being evolution variable. In this scheme one picks up value of $z \in (z_-, z_+)$ distributed according (1) or (2), $z_\pm$ being obtained from kinematical restrictions ($p_\perp^2 \geq Q_0^2$, $k_2^2 \geq Q_0^2$, $k_3^2 \geq Q_0^2$ for perturbative gluon branching, $p_\perp^2 \geq \Lambda^2$, $k_2^2 \geq \Lambda^2$, $k_3^2 \geq \Lambda^2$ for nonperturbative energy transfer from gluon to gluon condensate):

$$z_\pm^{pert} = \frac{1}{2}\left(1 \pm \frac{\sqrt{k_1^2 - 8Q_0^2}}{k_1}\right), \tag{12}$$

$$z_\pm^{nonpert} = \frac{1}{2}\left(1 \pm \frac{\sqrt{k_1^2 - 8\Lambda^2}}{k_1}\right). \tag{13}$$

Once z is picked up, the values of $k_2^2$ and $k_3^2$ are picked up randomly from the allowed kinematical region. Accurate account of Sudakov form factor is done as well.

The fusion of gluons is rather straightforward. The only subtle point is impossibility to carry out fusion effectively at moderate energies, when there is a shortage of gluons to choose for fusion.

### 3. Multiplicity Distributions.

Experimental multiplicity distributions of hadrons ($P_n = \frac{\sigma_n}{\sigma}$) are the result of processing large number of events with large number of particles in each event. Therefore they are statistical distributions and dynamics of the process can be concealed by large number of events. Let us define factorial moments [5] which are quantities refined from statistical fluctuations:

$$F_q = \frac{\sum_{n=0}^{\infty} n(n-1)...(n-q+1)P_n}{(\sum_{n=0}^{\infty} nP_n)^q} = \tag{14}$$
$$= \frac{< n(n-1)...(n-q+1) >_{events}}{< n >^q_{events}}.$$

Cumulants $K_q = F_q - \sum_{m=1}^{q-1} C^m_{q-1} K_{q-m} F_m$ and the ratio of cumulants to factorial moments $H_q = \frac{K_q}{F_q}$ are also studied because of their sensivity to the form of multiplicity distributions.

On fig.1,2 computed $F_q$ and $H_q$ are shown (Q=100 Gev, $\Lambda$=0.23 Gev, $Q_0$=1 Gev). It appears that Monte-Carlo model gives order of magnitude and oscillating behaviour of $H_q$ shown in [6] for experimental data though there is no precise fitting. This result may indicate that approach proposed in [3] is a very good hadronization scheme for Monte-Carlo event generators.

## References


[1] Yu. L. Dokshitzer, V. A. Khoze, A. H. Müller and S. I. Troyan, Basics of Perturbative QCD, edited by J. Tran Thanh Van (Editions Frontiers, Gif-sur-Yvette Cedex-France, 1991).

[2] E. Witten, Nucl. Phys. **B223**, 422,433 (1983).

[3] K. Geiger, Phys. Rev. **D51** (1995) 3669-3687.

[4] T. Sjöstrand, Computer Physics Commun. **82**(1994) 74.

[5] E.A. DeWolf, I.M. Dremin, W. Kittel, Usp. Fiz. Nauk.**163** (1993)3.

[6] B.B. Levtchenko, Proc. of the Joint International Workshop on High Energy Physics and Quantum Field Theory, 1994.




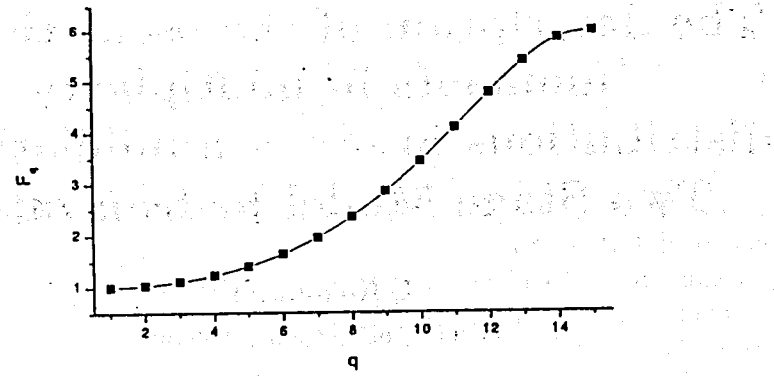


**Figure 1.** Factorial moments $F_q$ from Monte-Carlo code for $e^+e^-$-annihilation (Q=100 Gev, $\Lambda$=0.23 Gev, $Q_0$=1 Gev).

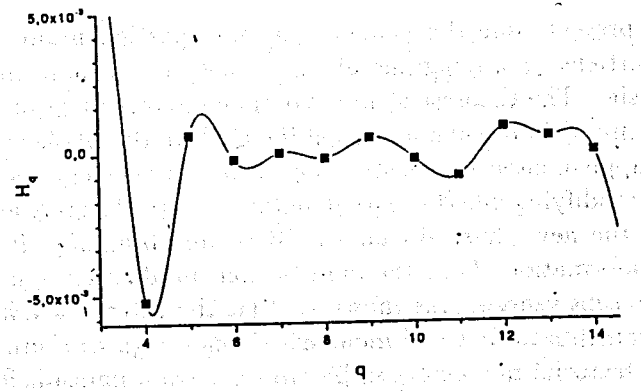


**Figure 2.** $H_q$ from Monte-Carlo code for $e^+e^-$-annihilation (Q=100 Gev, $\Lambda$=0.23 Gev, $Q_0$=1 Gev).

# The description of the oscillations of moments in multiplicity distributions in $e^+e^-$ - annihilation in Two Stage Model hadronization

E.Kokoulina
GSTU, 246746 Gomel, Belarus

June 8, 2000

**Abstract**

It is shown that Two Stage Model hadronization can explain the qualitative oscillations in sign of the ratio of factorial cumulant momentum on the factorial momentum of increasing order in $e^+e^-$-annihilation at $Z^0$ peak.

At the present time the dynamics of multiparticle production of elementary particles is staying one of the actual directions in modern high energy physics. The theoretical and experimental investigations are taking place. The impossibility of application PT QCD in the whole of interaction region is supplemented by construction of phenomenologic models. This models are modifying due the experimental data are changing at more high energies or the new physical characteristics are obtaining. It lets to get more new information about the multiparticle production dynamics.

At the recent years it was shown [1] that the ratio of the factorial cumulative moments to factorial moments changes sign as a function of its order. The factorial moments can be obtained from multiplicity distributions (MD) $P_n$, through the relations [2]:

$$F_q = \sum_{n=q} n(n-1)...(n-q+1)P_n \qquad (1)$$



for factorial moments and

$$K_q = F_q - \sum_{i=1}^{n} C_{q-i}^{i} K_{q-i} F_i \qquad (2)$$

for factorial cumulative moments. The ratio of their quantities is

$$H_q = K_q / F_q \qquad (3)$$

In this job the ratios are calculating (3) in Two Stage Model (TSM) [3] multiparticle production for $e^+e^-$-annihilations at the $Z^0$ peak. MDs were calculated in TSM [3] and described the experimental data [4] well. In this model process of multiparticle hadron production in $e^+e^-$ -annihilation goes on two stages. The stage of quark-gluon division is described by perturbative theory (PT) QCD. At the second stage (the transformation of quarks and gluons in hadrons) phenomenological model is used. MD of partons on the first stage is described by negative binomial distributions (NBD)

$$P_m^p = \frac{1}{m!}\frac{\partial^m}{\partial z^m} Q^p(s,z)|_{z=0}, Q^p(s,z) = [1 + \frac{\overline{m}}{k_p}(1-z)]^{-k_p} \qquad (4)$$

where $\overline{m}$ and $k_p$ are parameters, $Q^p(s,z)$ is the generation function for MD $P_m^p$. On stage of hadronization MDs of hadrons formed from partons are described by positive binomial distribution (PBD)

$$P_n^h = C_{N_p}^n (\frac{\overline{n}_p^{\,h}}{N_p})^n (1 - \frac{\overline{n}_p^{\,h}}{N_p})^{N_p - n} \qquad (5)$$

with generation function

$$Q_p^H = [1 + \frac{\overline{n}_p^{\,h}}{N_p}(z-1)]^{N_p}. \qquad (6)$$

The parameters $n_q^h$ and $N_p$ ( p=q(g) for quark(gluon) ) have sense of average and maximum multiplicities of hadrons formed from parton (q or g) on the stage of hadronization. The generation function for MD of hadrons in $e^+e^-$-annihilation in supposition soft blechment of partons are determining by convolution of two stages

$$G(z) = \sum_{m=0} P_m^g [Q_g^H(z)]^m Q_q^2(z), G(z) = Q^p(Q_g^H(z)) Q_q^2(z). \qquad (7)$$

For comparison with experimental data on MD [4] the expression was used [5]

$$P_n(s) = \Omega \sum_{m=0} P_m^p C^m_{(2+\alpha m)N} (\frac{\overline{n}_q{}^h}{N})^n (1 - \frac{\overline{n}_q{}^h}{N})^{(2+\alpha m)N-n} \quad (8)$$

where $\Omega$ is a normalized factor, $P_m^P$ is determined by (4), $N = N_q$, $\alpha = \frac{N_g}{N_q}$ are parameters of the model.

MD (8) are described the experimental data from 14 GeV to $Z^0$ peak [4]. The summation over numbers of gluons (m) is fulfilling from 0 to 80. In [5] the parameter $N$ is constant and equals to 5. In this job the parameter $N$ can change. This behavior of the parameters of TSM lets to describe the oscillations of sign of $H_q$ (3). In accordance [5] it is possible to calculate in TSM $F_q$ and $K_q$ [6]:

$$F_q = \frac{1}{\overline{n}^q(s)} \frac{\partial^q G}{\partial z^q}|_{z=1} \quad (9)$$

$$K_q = \frac{1}{\overline{n}^q(s)} \frac{\partial^q \ln G}{\partial z^q}|_{z=1} \quad (10)$$

The expression (7) for $G(s,z)$ after taking a logarithm

$$\ln G(s,z) = -k_p \ln [1 + \frac{\overline{m}}{k_p}(1 - Q_\alpha)] + 2 \ln Q$$

and the expansion to series in a power on $Q_\alpha$ will be

$$\ln G(s,z) = k_p \sum_{m=1} (\frac{\overline{m}}{\overline{m} + k_p})^m \frac{Q_\alpha^m}{m} + 2 \ln Q. \quad (11)$$

If will put (6) into (11) for $Q_\alpha$ and $Q$, we will get

$$\ln G(s,z) = k_p \sum (\frac{\overline{m}}{\overline{m} + k_p})^m \frac{1}{m} [1 + \frac{\overline{n}^h}{N}(z-1)]^{\alpha m N} + 2N \ln [1 + \frac{\overline{n}^h}{N}(z-1)].$$

Now it is possible to find $K_q$ using (10)

$$K_q = (\sum_{m=1} \alpha(\alpha m - \frac{1}{N})...(\alpha m - \frac{q-1}{N})(\frac{\overline{m}}{\overline{m} + k_p})^m - (-1)^q \frac{(q-1)!}{N^{q-1}})(\frac{\overline{n}^h}{\overline{n}(s)})^q, \quad (12)$$



where $\overline{n}(s)$ is the average multiplicity hadrons in $e^+e^-$ - annihilation and $F_q$, using (9)

$$F_q = \sum_{m=0} (2 + \alpha m)(2 + \alpha m - \frac{1}{N})...(2 + \alpha m - \frac{q-1}{N}) P_m (\frac{\overline{n}^h}{\overline{n}(s)})^q \quad (13)$$

with

$$P_m = \frac{k_p(k_p+1)...(k_p+m-1)}{m!} (\frac{k_p}{k_p + \overline{m}})^{k_p} (\frac{\overline{m}}{\overline{m} + k_p})^m.$$

The sougt-for expression for $H_q$ will be

$$H_q = \Omega_1 \frac{\sum_{m=1} \alpha m(\alpha m - \frac{1}{N})...(\alpha m - \frac{q-1}{N})(\frac{\overline{m}}{\overline{m}+k_p})^m \frac{1}{m} - (-1)^q \frac{(q-1)!}{N^{q-1}}}{\sum_{m=0}(2 + \alpha m)(2 + \alpha m - \frac{1}{N})...(2 + \alpha m - \frac{q-1}{N}) P_m}, \quad (14)$$

where $\Omega_1$ is a normalized factor.

The comparison with data SLD coll.[1] shows that (14) describes qualitatively behavior of the factorial momentum ratio only. It is seen minimum at q=5, there are small oscillations of sign for q from 9 to 15, but after q=15 the oscillations begin to grow.

The value of parameters described quark-gluon devision ($\overline{m}$, $k_p$) and the stage of hadronization ($\alpha$, $N$) almost not differ from value were got in [5] for MD. The parameter $\overline{n}^h$ in (14) is absent. It value may be get from average multiplicity

$$\overline{n}(s) = (2 + \alpha \overline{m}) \overline{n}^h. \quad (15)$$

It is staying almost regular in both fits: for MD and $K_q$. The parameter $\alpha$ is staying regular too. It determines the ratio $N_g$ to $N_q$ and equal from 0.3 to 0.4. It shows that quark jet gives more hadrons than gluon jet about three times. The parameter $N$ (maximum number of hadrons from quark on stage of hadronization) from MD in [5] is changing from 5 and higher, and from $H_q$ from 5 to 3. The parameter of OBD $k_p$ is staying constant (from 18 to 23) in both cases, too.

So, the behaviour parameters of TSM at $Z^0$ peak for MD is agreed with behaviour for $H_q$. The quantity of $\chi^2$ for $H_q$ is not good. Perhaps this happens on the reason of difference the mechanism of multiparticle production of hadrons on the second stage from TSM, the undeveloped parton cascade (not a lot of gluons) and so assymetry of process cascade, marking besides two quark jets and their bremstrahlung gluons, deviding gluons, too.

The formation of several gluon jets in addition of quark jets can make the oscillation of $H_q$ slower.

In conclusion can made some additions to the behaviour mean multiplicity of partons $\overline{m}(s)$ for $e^+e^-$-annihilation on the first stage. In accordance [3] it may be fitted by phenomenological expression

$$\overline{m}(s) = \beta \ln \frac{\sqrt{s}}{\sqrt{s_0}}, \qquad (16)$$

with $\beta \approx 1.35$ and $\sqrt{s_0} \approx 1.8$ GeV. So, considering true this approximation at low energies it is possible to consider appearance of gluons in $e^+e^-$-annihilation begins from the energies near 2 GeV.

The mean multiplicity of hadrons on the second stage from one quark $\overline{n}_q^h(s)$ may be approximated phenomenological, too

$$\overline{n}_q^h(s) = \beta \ln \frac{\sqrt{s}}{m_0}, \qquad (17)$$

where $\beta_1 \approx 0.79$, $m_0 \approx 370$ MeV. The last energy $m_0$ determs energetic region from which begin to appear process of multiparticle production.

It is shown that TSM does not contradict the experimental data on the oscillation ratio of factorial moments at $Z^0$ break, but it is necessary detail study and subsequent modifications.

I thank Kuvshinov V.I. for support and help in job. I thank the laboratory of physics investigations of Gomel state technical university for support, too.

## References

[1] K. Abe et al. SLD Coll. //Phys.Lett. B 371, 149 (1996)

[2] A. Giovannini, S. Lupia and R. Ugoccioni //Phys.Lett. B 374, 231 (1996)

[3] V.I. Kuvshinov, E.S. Kokoulina // Acta Phys.Pol. B 13, 553 (1982)

[4] DELPHI Coll. // CERN-PPE/90-173 (1990)

[5] E.S. Kokoulina // Proc. sem. NPCS. 176 (1995)

[6] I.M. Dremin //Physics Uspekhi 164, 785 (1994)



# Some notes about multiplicity distribution at hadron colliders

E.A.Kuraev, J.Manjavidze*, A.Sissakian
JINR, Dubna, Russia

July 12, 2000

**Abstract**

Idea that the very high multiplicity (VHM) ivents are governed by hard processes is considered. For this purpose quantitative realization of the Pomeron, DIS and large-angle annihilation (LAA) mechanism combinations are considered in the pQCD frame. The phase transition (condensation) in the soft pions system is described as the alternative to above mechanism. It is shown that it predicts enhancement in VHM tail as compared to QCD prediction.

## 1

The estimations of an expected multiplicities distribution tails at LHC energies are offered as possible physical programm. Investigation of the multiplicity distributions was popular since seventies [1]. The very high multiplicity (VHM) processes as the attempt to get beyond standard multiperipheral hadron physics was considered in [2]. The hadron theory based on the local QCD Lagrangians [3] and the experimental consequences was given in the review papers [4].

We begin with general analysis. Let $\sigma_n(s)$ be the cross section of $n$ particles creation at the CM energy $\sqrt{s}$. We introduce the generating function:

$$T(s,z) = \sum z^n \sigma_n, s = (p_1 + p_2)^2 >> m^2. \qquad (1.1)$$

*Permanent address: Inst.of Phys. Tbilisi, Georgia

So, the total cross section and the averaged multiplicity will be:

$$\sigma_{tot} = T(s,1) = \sum \sigma_n, \sigma_{tot}\bar{n} = \sum n\sigma_n = \frac{d}{dz}T(s,z)_{z=1}. \quad (1.2)$$

At the same time

$$\sigma_n = \int \frac{dz}{2\pi i z^{n+1}} T(s,z) = \int \frac{dz}{2\pi i} e^{(-(n+1)\ln z + \ln T(s,z))}. \quad (1.3)$$

Applying the steepest descent method we may determine the asymptotical behavior of $\sigma_n$ at large $n$. It was shown in paper of T.D.Lee and C.N.Yang [5] that the singularities $z_s$ of $T(z,s)$ in the $z$ plane may be located at $|z| \geq 1$ only. We may distinguish following possibilities at $n \to \infty$:
1)$z_s = 1$: $\sigma_n > O(e^{-n})$;
2)$z_s = \infty$: $\sigma_n < O(e^{-n})$;
3)$z_s = z_c, 1 < z_c < \infty$: $\sigma_n = O(e^{-n})$.
The second type belong to the multiperipheral processes kinematics: created particles form jets moving with different velocities along the CM incoming particles.

Another information is included in

$$\ln T(s,z) = \sum \frac{(z-1)^m}{m!} c_m. \quad (1.4)$$

For instance, if $c_m = 0$, $m > 1$ we have the Poisson distribution: $\sigma_n = \sigma_{tot}\frac{(\bar{n})^n}{n!}\exp(-\bar{n})$. If $c_m = \gamma_m (c_1)^m$, i.e. $\gamma_m$ is the some restricted function of $m$, than the so called KNO scaling take place: $\sigma_n \sim \sigma_{tot} f(n/\bar{n})$. One of the mostly interesting question: is the KNO scaling really takes place?

It was found in seventieth that the multiperipheral kinematics dominates inclusive cross sections $f(s,p_c)$. Moreover, the created particles spectra do not depend on $s$ at high energies in the multiperipheral region:

$$f(s,p_c) = 2E_c\frac{d\sigma}{d^3p_c} = \int \frac{dt_1 dt_2 s_1 s_2 \phi_1(t_1)\phi_2(t_2)}{(2\pi)^2 s(t_1-m^2)^2(t_2-m^2)^2}, \; s_1 s_2(-p_{c\perp}^2) = s t_1 t_2.$$

Here $s_1 = (p_a + p_c)^2, s_2 = (p_b + p_c)^2, p_c = \alpha_c p_a + \beta_c p_b + p_{c\perp}$ and $\phi_i(t_i)$ are the impact factors of hadrons. So the particle $c$ forgot the details of its creation. It was found experimentally that the ratio

$$\frac{f(\pi^+ p \to \pi_- + ...)}{\sigma(\pi^+ p)} = \frac{f(K^+ p \to \pi_- + ...)}{\sigma(K_+ + p)} = \frac{f(pp \to \pi_- + ...)}{\sigma(pp)} \quad (1.5)$$



is universal [6]. This take place due to the two Pomeron multiperipheral exchange providing the nonvanishing contribution in the $s$ asymptotics to the cross section. It was implied that the Pomeron intercept is exactly equal to one. Just this kinematics leads to the KNO-scaling [7].

The asymptotics 1) assumes phase transition [8]. The signal of creation of exotic state of pions say in the isotopic state with $I_z = 0$ (production of anomalous number of $\pi_0$) in the region of space of pions Compton wavelength order – so called pion condensate – may lead to the observable effect in multiplicity distributions. One may expect considerable deviation from the regime $O(e^{-n})$ mentioned above.

Let us demonstrate this reason using almost hand-waving arguments. The effective pion's lagrangian of S.Weinberg [9] $L_{eff} \sim (1-\vec{\pi}^2/f_\pi^2)^{-1}, f_\pi = 140 MeV$, regards the current algebra theorems, describe rather satisfactory the soft pions interaction. Using the functional integral approach we may consider the $n$ pion's correlator

$$\int D\pi f_\pi^{-2n} \pi^{i_1}(x_1)...\pi^{i_{2n}}(x_{2n}) e^{-L_{eff}(\pi)}.$$

The associated probability of creation of $2n$ pions may estimated, assuming that the kinetic part of Lagrangian is negligible,

$$p_{2n} = \int_0^1 dx x^n \frac{1}{1-x} e^{[-\frac{1}{1-x}]} \sim e^{(-2\sqrt{n})}, \quad n \to \infty. \quad (1.6)$$

Note, the $\pi^2 \approx 1 - \sqrt{f_\pi/n} \to 1$ is essential in this integral. This means that the potential part of Lagrangian is $\sim \sqrt{n/f_\pi} \to \infty$ and thus the semiclassical approximation is valid.

## 2

The Pomeron is treated as a (infinite) set of particles emitted close to the CM beams direction (within the small angles of order $\theta_i \sim 2m_h/\sqrt{s} << 1$). We expect that these type of particles will not be detected by the detectors since they are move into the beams pipe. The collider experiment detectors locate at finite angles $\theta_D \sim 1$ and will measure the products only of particle $c$ decay.

What will happened when instead of one particle a set of particles with invariant mass square $s_t$ is created at large angles? Then the cross section

will acquire the type suppression factor $(m^2/s_t)F(\alpha_s \ln^2(s_t/s_0))$ with the function

$$\sigma_n = \frac{\alpha_s^2}{s_t} N F_n(\alpha_s^2 \ln^2(\frac{s}{s_0})),\ N = (\frac{s}{s_0})^{\Delta},$$
$$\Delta = \alpha_P - 1 = \frac{12 \ln 2}{\pi}\alpha_s \approx 0.55,\ \alpha_s = 0.2 \qquad (2.1)$$

Radiative corrections to the intercept was calculated [10] in recent time. The resulting value is $\Delta \approx 0.2$.

The way to obtain detected large multiplicity is to organize DIS-like experiments, expecting the large-angle scattered hadrons in the detectors. Large transfers momenta will be decreasing by ordinary evolution mechanism to the value of order $m_\pi$ and then the Pomeron mechanism of peripheral scattering of the created hadrons from the poinization region will start.

What the characteristic multiplicities expected from Pomeron mechanism with the intercept exceeding unity, $\Delta \sim 0.2$? It is the quantity of order $(s/m_\pi^2)^{\Delta} \approx 200$ for $\sqrt{s} = 14TeV$. This rather rough estimation is in agreement with the phenomenological analysis of A.Kaidalov [1], based on multi-pomeron exchange in the scattering channel.

## 3

Let now construct the relevant cross sections. It is convenient to separate them to the classes
a) Pomeron regime (P);
b) Evolution regime (DIS);
c) Double logarithmic regime (DL);
d) DIS+P regime;
e) P+DL+P regime.
The description of every regime may be performed in terms of effective ladder-type Feynman diagrams (The set of relevant FD depends on the gauge chosen and include much more number of them).

For the pure Pomeron regime [3] the estimated cross section have the form: $(y = \frac{\alpha_s}{16\pi^2},\quad m^2 \sim s_0 \sim m_\pi^2)$

$$d\sigma_{2\to 2+n} = \frac{1}{64\pi^2}\int_{m^2/s}^{1}\frac{d\beta_n}{\beta_n}\int_{m^2/s}^{\beta_n}\frac{d\beta_{n-1}}{\beta_{n-1}}\dots$$



$$\times \int_{m^2/s}^{\beta_2}\frac{d\beta_1}{\beta_1}dZ_n \int \frac{d^2q_{n+1}}{(q_{n+1}^2 - m^2)^2}(\Gamma_1\Gamma_2)^2; \qquad (3.1)$$
$$dZ_n = y^n \Pi_{i=1}^{i=n}\int d^2q_i \Pi_{i=1}^{i=n}\frac{(s_i/s_0)^{\alpha(q_i)}\gamma_{i,i+1}^2}{(q_i^2 - m^2)^2}.$$

Performing $\beta$-integration,

$$\int_{m^2/s}^{1}\frac{d\beta_n}{\beta_n}\int_{m^2/s}^{\beta_n}\frac{d\beta_{n-1}}{\beta_{n-1}}\dots\int_{m^2/s}^{\beta_2}\frac{d\beta_1}{\beta_1} = L^n n!,\quad L = \ln\frac{s}{m^2}. \qquad (3.2)$$

Here $q_i = \alpha_i p_2 + \beta_i p_1 + q_{i\perp}$ is the 4-momentum of the virtual gluon joining the emitted particles with 4-momenta $k_i, k_{i+1}$, $s_i = (k_i + k_{i+1})^2$ is their invariant mass square. One should use here that

$$s_1 s_2 \cdots s_{n+1} = s E_{1\perp}^2 \cdots E_{n\perp}^2,\ E_{i\perp}^2 = m_i^2 + (\vec{q}_i - \vec{q}_{i-1})^2,$$
$$m^2 << s_i << s = 2p_1p_2, \qquad (3.3)$$

where

$$\alpha(q_i) = \frac{\alpha_s(q_i^2 - m^2)}{2\pi^2}\int \frac{d^2k}{(k^2 - m^2)((q_i - k)^2 - m^2)},$$

is the reggeized gluon trajectory. Here we imply the arrangement on the rapidities of the emitted gluons

$$\frac{m^2}{s} << \beta_n << \beta_{n-1} < \dots << \beta_1 \sim 1. \qquad (3.4)$$

The quantity $\Gamma_{1,2}$ may be associated with the formfactors of the initial hadrons (simply we replace them by the coupling constants of $g$, $g^2 = 4\pi\alpha_s$) whereas the quantities $\gamma_{i,i+1}$ associated with the effective vertices of transition of two gluons to the emitted particle. For the case of emission of scalar particle we have $\gamma_{i,i+1} = m$. For the case of emission of gluon with momentum $k_i = q_i - q_{i+1}$ we have

$$\gamma_{i,i+1} = g[-(q_i + q_{i+1}) - p_2(\frac{2p_1k_i}{p_1p_2} - \frac{m^2 - q_i^2}{p_2k_i}) + p_1(\frac{2p_2k_i}{p_1p_2} - \frac{m^2 - q_{i+1}^2}{p_1k_i})]. \qquad (3.5)$$

## 4

For the pure deep inelastic case, when one of the initial hadrons is scattered at the angle $\theta$ have the energy $E'$ in the cms of beams whereas

the another is scattered at small angle and the large transfer momentum $Q = 4EE'\sin^2(\theta/2) >> m^2$, is distributed to the some number of the emitted particles due to evolution mechanism we have [11]($\theta$ is small):

$$d\sigma_n^{DIS} = \frac{4\alpha^2 E'^2}{Q^4 M} dD_n dE' d\cos\theta,$$

$$dD_n = (\frac{\alpha_s}{4\pi})^n \int_{m^2}^{Q^2} \frac{dk_n^2}{k_n^2} \int_{m^2}^{k_n^2} \frac{dk_{n-1}^2}{k_{n-1}^2} \cdots \int_{m^2}^{k_2} \frac{dk_1^2}{k_1^2} \int_x^1 d\beta_1 \int_{\beta_1}^1 d\beta_2 ...$$

$$\times \int_{\beta_2}^1 d\beta_1 P(\frac{\beta_n}{\beta_{n-1}}) ... P(\beta_1), \quad P(z) = 2\frac{1+z^2}{1-z}, \qquad (4.1)$$

where the limits of integrals show the intervals of variation and the integrand is the differential cross section.Again the rapidities $\beta_i$ are rigorously arranged as well as the transvers momenta squared.

# 5

For the large-angles particles production process the differential cross section (as well as the total one) fall with cms energy $\sqrt{s}$.We will consider for definiteness the process of annihilation of electron-positron pair to $n$ photons [12]:

$$d\sigma_n^{DL} = \frac{2\pi\alpha^2}{s} dF_n,$$

$$dF_n = (\frac{\alpha}{2\pi})^n \int_0^\rho dy_n \int_0^\rho dx_n \theta(x_n - y_n) \int_0^{y_n} dy_{n-1}$$

$$\times \int_0^{x_n} dx_{n-1} \theta(x_{n-1} - y_{n-1}) ..., x_i = \ln\frac{q_i^2}{m^2}, \quad y_n = \ln\frac{1}{\beta_i}, \quad \rho = \ln\frac{s}{m^2}, \qquad (5.1)$$

The similar formulae takes place for subprocess of quark-antiquark annihilation into the $n$ large-angle moving gluons. We note that the quantities $q_i^2$ may vary up to maximal value,$s$ which corresponds to the emission at large angles. The total cross section of annihilation to any number of photons is:

$$\sigma_{tot}(s) = \frac{2(2\pi\alpha)^{3/2}}{s} \frac{2}{x} I_2(x), x^2 = \frac{2\alpha}{\pi}\rho^2. \qquad (5.2)$$

We conclude that the differential cross sections of the $n$ particles production may be presented as a product of factors

$$\frac{dq_i^2}{q_i^2} \frac{d\beta_i}{\beta_i}$$



under various assumptions about transvers momentum $q_i$ and rapidity $\beta_i$.

We will suppose that every emitted particle of mass (virtuality) $M$ will decay and create the number of secondary particles (pions) with the probability

$$dW_n(M) = dn \frac{c}{\bar{n}} e^{-\frac{cn}{\bar{n}}}, \bar{n} = \ln\frac{M^2}{m_\pi^2}. \qquad (5.3)$$

Construct now the cross sections of combined processes. When the one of the initial particles $h_1$ is scattered on small but sufficient enough angle to fit the detectors and other is scattered almost forward the combination of DIS and Pomeron regimes take place:

$$d\sigma_{n,m} = d\sigma_n^{DIS} dZ_m, |q_n|^2 \sim m^2 \qquad (5.4)$$

provided that the virtuality of the last step of evolution regime of order of hadron mass. For the kinematical case of almost forward scattering of both initial hadrons the situation may be realized with large angles hadron production from the central region:

$$d\sigma_{n,m,k} = dZ_n d\sigma_m^{DL} dZ_k. \qquad (5.5)$$

# 6

We discuss in conclusion possible mechanism violation of the exponential fall down of the multiplicity as a function of the number of the created particles $n$. It may take place due to creation pion condensate - the states of identical particles obeying the Bose-statistics. As a signal of this state may be the change of the distribution character of multiplicity on $n$ in the region $n \sim n_{max}/2$: exponential fall off will be changed on the (exponential?) growth [13]. If such an effect will take place some understanding about Centaurus cosmic events may be obtained.

**Acknowledgments**

We are grateful to V.G.Kadyshevski for interest to discussed in the paper questions.

# References

[1] A.Kaidalov, *Yad. Fiz.*, **61** (1998) 911; I.Dremin R.C.Hwa, *Phys. Rev.*, **D49** (1994) 5805

[2] J.Manjavidze and A.Sissakian, *JINR Rap. Comm.*, (1999)

[3] E.Kuraev, L.Lipatov and V.Fadin, Sov. Phys. JETP, 44, 443 (1976), Zh. Eksp. Teor. Fiz., 71 (1976) 840; L.Lipatov, *Sov. J. Nucl. Phys.*, **20** (1975) 94, V.N.Gribov and L.Lipatov, *Sov. J. Nucl. Phys.*, **15** (1972) 438, 675, G.Altarelli and G.Parisi, *Nucl. Phys.*, **B126** (1977) 298.

[4] V.Khoze and W.Ochs, *J. Mod. Phys.*, **A12** (1997) 2949.

[5] T.D.Lee and C.N.Yang, Phys. Rev., 87 (1952), 404,410.

[6] M.Ryskin, *VII Winter School*, (LIYaPh, 1972).

[7] Z.Koba, H.Nielsen and P.Olesen, *Nucl. Phys.*, **B40** (1972) 317.

[8] M.Kac, G.Uhlenbeck and P.Hemmer, *J. Math. Phys.*, 4 (1963) 216, 229.

[9] S.Weinberg, Phys. Rev., 166 (1968) 1568.

[10] V.Fadin and L.Lipatov, Phys. Lett., B429 (1998),127; M.Giaffaloni and G.Camici, Phys. Lett., B430 (1998),349.

[11] Yu.Dokshitzer, V.Khoze, A.Mueller and S.Trojan, *Basic of perturbative QCD* (Frontiers, 1991).

[12] V.G.Gorshkov and L.N.Lipatov, Yad. Fiz., 9 (1969) 818; V.G.Gorshkov, V.N.Gribov, L.N.Lipatov, G.V.Frolov, Yad. Fiz., 6 (1967) 129.

[13] V.A.Nikitin, *private communication.*



# ANALYTIC APPROACH IN QUANTUM CHROMODYNAMICS AND ITS APPLICATIONS

**I.L. Solovtsov**

*Gomel State Technical University, Gomel, 246746 Belarus and*
*Bogoliubov Laboratory of Theoretical Physics,*
*Joint Institute for Nuclear Research, Dubna, 141980 Russia*

**Introduction.** An intrinsic ingredient of modern quantum field theory (QFT) is the renormalization group (RG) method proposed in the mid-fifties [1, 2]. The role of this method is particularly important in the cases where the interaction is not weak, for example, in quantum chromodynamics (QCD). Hardly any hadronic process investigated in the QCD framework can be analyzed without using the renormalization group. It is well known that directly solving the RG equation for the invariant charge leads to unphysical singularities, for example, to the ghost pole in the one-loop approximation. Taking next loop corrections into account does not alter the essence, and leads only to additional branch cuts. The existence of such singularities contradicts the general principles of local QFT.

As early as in the late-fifties, N.N. Bogoliubov, A.A. Logunov and D.V. Shirkov in the paper [3] proposed a resolution of this problem in the context of quantum electrodynamics by unifying the RG method with the requirement of analyticity with respect to $Q^2$, which in turn followed from the known Källén–Lehmann representation expressing the basic principles of local QFT [4].

In this lecture we consider an analytic approach (AA) to QCD which has been proposed in [5, 6] and devised further in [7-19]. A new expression for the QCD running coupling obtained within this approach has a regular ghost-free behavior in the infrared region with the universal limiting value expressed only via group symmetry factors and independent of experimental estimates on the QCD scale parameter. The method leads to a well-defined procedure for analytically continuing the running coupling from the spacelike to the timelike domain. We present results of applying analytic perturbation theory to some hadronic processes. Theoretical predictions thus obtained turn out to be remarkably stable with respect to the renormalization scheme and higher loop dependence for the whole low-energy region.

**Analytic running coupling.** To construct an analytic coupling, we start with the leading order expression for the running coupling

$$\bar{a}^{(1)}(Q^2) = \frac{a}{1 + a\beta_0 \ln(Q^2/\mu^2)} = \frac{1}{\beta_0 \ln(Q^2/\Lambda^2)} \qquad (1)$$

where $\bar{a}(Q^2) = \bar{\alpha}_s(Q^2)/4\pi$ and $\beta_0 = 11 - (2/3)f$, the one-loop coefficient of the $\beta$-function for $f$ active flavors. According to [5, 6] an analytic coupling is written in the form of the spectral representation

$$\bar{a}_{\rm an}(Q^2) = \frac{1}{\pi}\int_0^\infty d\sigma \frac{\rho(\sigma)}{\sigma + Q^2 - i\epsilon}. \qquad (2)$$

The spectral function $\rho(\sigma)$ can be found via a discontinuity of the running coupling (1) on the physical cut

$$\rho^{(1)}(\sigma) = \frac{a^2\beta_0\pi}{(1 + a\beta_0 L)^2 + (a\beta_0\pi)^2}, \quad L = \ln\frac{\sigma}{\mu^2}. \qquad (3)$$

The renormalization group invariance of $\bar{a}_{\rm an}$ defined via Eq.(2) is provided by the scaling property of the spectral function $\rho(\sigma/\mu^2, a) = \tilde{\rho}(\ln\sigma/\Lambda^2)$, where the scale parameter is $\Lambda^2 = \mu^2\exp(-1/a\beta_0)$.

Substituting $\rho^{(1)}$ into Eq. (2) we get

$$\bar{a}^{(1)}_{\rm an}(Q^2) = \frac{1}{\beta_0}\left[\frac{1}{\ln Q^2/\Lambda^2} + \frac{\Lambda^2}{\Lambda^2 - Q^2}\right]. \qquad (4)$$

The analytic coupling (4) has no ghost pole at $Q^2 = \Lambda^2$. Its infrared limiting value $\bar{\alpha}^{(1)}_s(0) = 4\pi/\beta_0$ depends only on group factors and, numerically, for $f = 3$, we have $\bar{\alpha}^{(1)}_{\rm an}(0) = 4\pi/9 \simeq 1.398$. The first term on the of right-hand side Eq. (4) preserves the standard ultraviolet behavior of the invariant coupling. The second term, which comes from the spectral representation and enforces the proper analytic properties, compensates the ghost pole at $Q^2 = \Lambda^2$ and is essentially nonperturbative. This term gives no contribution to the perturbative expansion. Thus, the causality and spectrality principles expressed in the form of $Q^2$-analyticity, send us the message that perturbation theory is not the whole story. The requirement of proper analytic properties leads to the appearance of contributions given by powers of $Q^2$ that cannot be seen in the original perturbative expansion. We note also that unlike in electrodynamics, the asymptotic freedom



property in QCD has the effect that such nonperturbative contributions show up in the effective coupling function already in the domain of low energies and momentum transfers reachable in realistic experiments, rather than at unrealistically high energies.

As for a particular value of the analytic running coupling at $Q^2 = 0$ one can make two important statements. Firstly, the $\bar{\alpha}_{\rm an}(0)$ value is independent of $\Lambda$. Secondly, this infrared limiting value in any order of approximation is defined by the one-loop contribution (see details in [6, 19]). This means that the causality (=analyticity) property brings the feature of the universality. The theory supplies us with a set of possible curves for $\bar{\alpha}_s(Q)$ and one has to fix the "physical one" by comparing with experiment is accustomed. Eq. (4) describes a family of possible curves for $\bar{\alpha}_{\rm an}(Q^2)$ forming a bundle with the same common limit at $Q^2 = 0$ as it is shown in Fig. 1 (on the left).

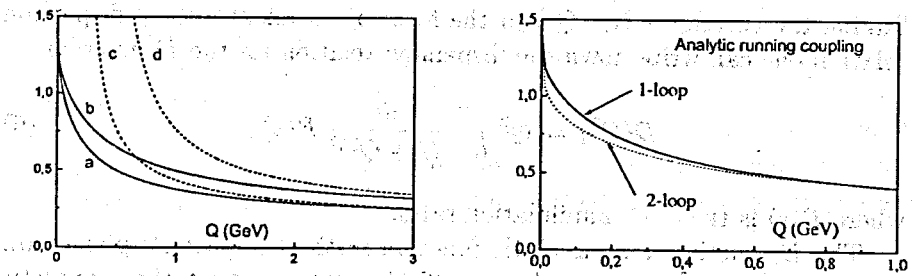


Figure 1: On the left. *The bundle of analytic solutions for invariant QCD coupling. The curves (a) and (b) are the 1-loop analytic $\bar{\alpha}_{\rm an}$ for $\Lambda = 200$ MeV and 400 MeV, respectively; the curves (c) and (d) show the corresponding pQCD result.* On the right. *"Higher loop stability" of the analytic solution. The normalization point is on the $\tau$ lepton scale: $\bar{\alpha}_s(M_\tau^2) = 0.34$.*

The whole shape of the $\bar{\alpha}_{\rm an}(Q^2)$ evolution turns out to be reasonably stable with respect to higher corrections. The point is that the universality of $\bar{\alpha}_{\rm an}(0)$ practically gives rise to stability of the $\bar{\alpha}^{(\ell)}_{\rm an}(Q^2)$ behavior with respect to higher correction in the whole infrared region. On the other hand, this stability in the ultraviolet domain is a reflection of the property of asymptotic freedom. As a result, our analytic model obeys approximate "higher loops stability" in the whole Euclidean region. Numerical calculation (performed in the $\overline{\rm MS}$ scheme for one-, two-, and three-loop cases with

$f = 3$) reveals that $\bar{\alpha}_{an}^{(2)}(Q^2)$ differs from $\bar{\alpha}_{an}^{(1)}(Q^2)$ within the 10% interval and $\bar{\alpha}_{an}^{(3)}(Q^2)$ from $\bar{\alpha}_{an}^{(2)}(Q^2)$ within the 1% limit. This fact is demonstrated in Fig. 1 on the right.

**Spacelike and timelike effective couplings.** The method described above defines the running coupling in the Euclidean (spacelike) range of momentum, $Q^2 > 0$. If we wish to parametrize processes with timelike momentum transfer, for example, the process of $e^+e^-$ annihilation into hadrons, we must make use of some nontrivial analytic continuation procedure from the spacelike to the timelike region (see, for example, [20, 21, 22, 23]). To this end one usually applies the dispersion relation for the Adler $D$-function, defined in terms of the correlation function for the quark vector current, $\Pi(q^2)$, as follows

$$D(Q^2) = -Q^2 \frac{d\Pi(-Q^2)}{dQ^2}. \tag{5}$$

Taking the correlator $\Pi(-Q^2)$ in the form of an unsubtracted dispersion relation one can write down the dispersion relation for the $D$-function

$$D(Q^2) = Q^2 \int_0^\infty \frac{ds}{(s+Q^2)^2} R(s), \tag{6}$$

where $R(s)$ is the $e^+e^-$ annihilation ratio.

The $D$-function is an analytic function in the complex $Q^2$ plane with a cut along the negative real axis. Taking into account these analytic properties we can write down the inverse relation for $R(s)$,

$$R(s) = -\frac{1}{2\pi i} \int_{s-i\epsilon}^{s+i\epsilon} \frac{dz}{z} D(-z), \tag{7}$$

where the contour goes from the point $z = s - i\epsilon$ to the point $z = s + i\epsilon$ and lies in the region of analyticity of the function $D(z)$.

Let us define effective couplings $\bar{a}^{\rm eff}(Q^2)$ in the spacelike region and $\bar{a}_s^{\rm eff}(s)$ in the timelike region based on the following expressions for $D(Q^2)$ and $R(s)$

$$D(Q^2) \propto \left[1 + d_1 \bar{a}^{\rm eff}(Q^2)\right], \quad R(s) \propto \left[1 + r_1 \bar{a}_s^{\rm eff}(s)\right], \tag{8}$$

where $d_1$ and $r_1$ are the first coefficients of perturbative expansions. The subscript $s$ in (8) means "$s$-channel" (the timelike region). From (6) and



(7), one finds the connections between these effective couplings in the spacelike and timelike regions

$$\bar{a}^{\rm eff}(Q^2) = Q^2 \int_0^\infty \frac{ds}{(s+Q^2)^2} \bar{a}_s^{\rm eff}(s), \quad \bar{a}_s^{\rm eff}(s) = -\frac{1}{2\pi i} \int_{s-i\epsilon}^{s+i\epsilon} \frac{dz}{z} \bar{a}^{\rm eff}(-z). \tag{9}$$

These equations serve to define the effective coupling $\bar{a}_s^{\rm eff}(s)$ which parametrizes the $R(s)$ ratio and plays the role of the running coupling in the timelike region. One usually applies the standard perturbative approximation for $a^{\rm eff}(z)$ to derive the effective coupling in the $s$-channel from (9). This way leads to the so-called $\pi^2$-terms which play an important role in the phenomenological analysis of various processes. However, the perturbative approximation of $a^{\rm eff}(z)$ breaks the analytic properties mentioned above. For example, in the one-loop approximation the function $a^{\rm eff}(z)$ has the form $1/[\beta_0 \ln(z/\Lambda^2)]$ with a ghost pole at $z = \Lambda^2$, which contradicts the assumption that $a^{\rm eff}(z)$ is an analytic function in the cut $z$-plane. A consequence of this problem is the fact that if $a_s^{\rm eff}(s)$, obtained in such a way, is substituted into (9), the original one-loop formula in the spacelike region is not reproduced.

This difficulty can be avoided in the framework of AA, in which the running coupling is forced to have the correct analytic properties.[1] As a result,the effective coupling in the timelike region is given by the following elegant expression [7]:

$$\bar{a}_s^{\rm eff}(s) = \frac{1}{\pi} \int_s^\infty \frac{d\sigma}{\sigma} \rho(\sigma). \tag{10}$$

Both couplings $\bar{a}^{\rm eff}(Q^2)$ and $\bar{a}_s^{\rm eff}(s)$ have the same universal limit at $Q^2 = +0$ and $s = +0$ and a similar ultraviolet tails as $Q^2 \to \infty$ and $s \to \infty$. However, in the intermediate region the effect of analytic continuation becomes important. The distinction between the different effective couplings is several percent, which may be important for extracting the QCD coupling constant from various experimental data.

More than two decades ago, Schwinger proposed [27] that the Gell-Mann–Low function, or the $\beta$-function, in QED could be represented by a spectral function for the photon propagator. Remarkably, we find that

[1] The correct analytic properties of the $D$-function can also be maintained in the framework of the so-called variational perturbation theory which is based on a new small expansion parameter [24] (see Refs. [25, 26]).

this idea is realized in our proposal for the timelike coupling in QCD. For the $\beta$-function which corresponds to the coupling defined in the Euclidean region this statement is true through the two-loop approximation, but breaks down if one takes into account three-loop contributions. However, Schwinger's identification is certainly correct if we construct the $\beta$-function for the coupling (10) defined in the timelike region:

$$\beta_s = s\frac{d\bar{a}_s^{\rm eff}}{ds} = -\frac{\rho(s)}{\pi}. \tag{11}$$

In perturbation theory, the difference between the couplings in the spacelike and timelike regions is given by three-loop diagrams and, therefore, $\beta = Q^2 d\bar{a}^{\rm eff}/dQ^2 = -\rho(s)/\pi + O(\text{3-loop})$.

Defining the $\beta$-function of the $t$-channel charge $\beta(Q^2) = Q^2 d\bar{a}^{\rm eff}(Q^2)/dQ^2$ we can write down the following relation between two $\beta$-functions

$$\beta(Q^2) = Q^2 \int_0^\infty \frac{ds}{(s+Q^2)^2}\beta_s(s)\,. \tag{12}$$

Thus, the general properties of the theory lead to the following properties of the $\beta$-function considering as a function of $Q^2$: $\beta(Q^2)$ is an analytic function in the complex $Q^2$-plane with a cut along the negative real axis.

It is interesting to consider whether there exists a possible solution, which can be called an $s$-$t$ 'self-dual solution' of Eq. (12), in which there is a symmetrical behavior of the charges for the $t$- and $s$- channels. In this case $\beta(Q^2) = \beta_s(s = Q^2)$ and we have the integral equation to the $\beta$-function. It is clear that there is a "trivial" solution of this equation, $\beta(Q^2) = const$. Are there any other solutions? Introduce the variables $Q^2/\Lambda^2 = \exp(x)$ and $s/\Lambda^2 = \exp(y)$, and put $\phi(x) = \beta(Q^2)$ and $\phi(y) = \beta(s)$; we obtain the integral equation

$$\phi(x) = \int_{-\infty}^{\infty} dy\, K(x-y)\,\phi(y) \tag{13}$$

with the kernel $K(x) = 1/[4\cosh^2(x/2)]$.

By applying the Fourier transform to Eq. (13) one finds

$$\tilde{\phi}(p) = \tilde{K}(p)\,\tilde{\phi}(p)\,, \tag{14}$$

where $\tilde{K}(p) = \pi p/\sinh(\pi p)$.

Possible nontrivial solutions of Eq. (14) appear at the points, for which $\tilde{K}(p) = 1$. However, there is only one point of that sort: $p = 0$. Therefore,



$\tilde{\phi}(p) \propto \delta(p)$, which leads to the "trivial" solution $\beta(Q^2) = const$ and other $s$-$t$ self-dual solutions are absent.

Thus, behaviors of the running couplings in the spacelike and timelike regions can not be symmetrical in any renormalization scheme [12]. It should be stressed that to reach this conclusion we used only the properties of analyticity, which reflect the general principles of the theory, and, therefore, this result can be considered as a rigorous result coming from the first principles of quantum field theory.

**Analytic perturbation theory and inclusive $\tau$ decay.** The inclusive character of the decay of a $\tau$ lepton into hadrons and the fact that the nonperturbative QCD contributions to this process are very small [28] make it possible, in principle, to describe this process on the basis of the standard methods of quantum field theory without any model assumptions. Measurement of the ratio of hadronic to leptonic $\tau$ decay widths, i.e., the quantity $R_\tau = \Gamma(\tau \to \text{hadrons}+\nu)/\Gamma(\tau \to l\nu\bar{\nu})$, allows one to extract, with a high degree of accuracy, the value of the strong coupling constant $\alpha_s$ at the $\tau$ mass, $M_\tau \simeq 1.78$ GeV. Comparing this value with the values of $\alpha_s$ found at higher energy is an important test of the applicability of QCD perturbation theory over a wide range of energies and requires a careful check. At present, both experimental and theoretical investigations of the decay of a $\tau$ lepton are continuing intensively.

One usually employs analytic properties of the hadronic correlation function in order to rewrite the original expression for the $\tau$ hadronic rate, which involves integration over a nonperturbative region of small momenta, in the form of a contour integral over a circle of sufficiently large radius $Q^2 = M_\tau^2$ to apply perturbation theory (PT). However, the perturbative approximation, which introduces a ghost pole, violates the analytic properties required to use the Cauchy theorem in this manner.

Following [10] we will apply analytic perturbation theory (APT) in which it is possible to maintain the correct analytic behavior. For our purpose, it is important that, within this approach, it is possible to give a self-consistent definition of the running coupling in the Minkowskian region [7]. This fact allows us to obtain two equivalent representations for the QCD correction to $\tau$ decay, involving the timelike and the spacelike definitions of the running couplings, respectively.

Why is analyticity important? The initial theoretical expression for $R_\tau$ in the case of massless quarks contains an integral over timelike momen-

tum $s$ [28]

$$R_\tau = \frac{2}{\pi}\int_0^{M_\tau^2}\frac{ds}{M_\tau^2}\left(1-\frac{s}{M_\tau^2}\right)^2\left(1+2\frac{s}{M_\tau^2}\right)\mathrm{Im}\,\Pi(s)\,, \qquad (15)$$

where the range of integration extends down to small $s$ and cannot be calculated in the framework of the standard perturbation theory. The method of calculation of $R_\tau$ based on exploiting certain analytic properties of the hadronic correlators $\Pi(s)$ allows one to rewrite the expression (15) by using the Cauchy theorem in the form of a contour integral in the complex $s$-plane with the contour running clockwise around a circle centered on the origin of radius $M_\tau^2$:

$$R_\tau = \frac{1}{2\pi\mathrm{i}}\oint_{|s|=M_\tau^2}\frac{ds}{s}\left(1-\frac{s}{M_\tau^2}\right)^3\left(1+\frac{s}{M_\tau^2}\right)D(-s)\,. \qquad (16)$$

In the representation (16) the contour has a sufficiently large radius, and it is possible, in principle, to calculate $R_\tau$ perturbatively. However, the transition to the contour representation requires certain analytic properties of the correlator. Namely, the correlator $\Pi(s)$ is an analytic function in the complex $s$-plane with a cut along the positive part of the real axis. The parametrization of $\Pi$ by the perturbative running coupling violates these analytic properties. It is clear that the difference in the regions of integration in the initial expression (15) for $R_\tau$ and the expression (16) obtained after applying the Cauchy theorem makes it necessary to parametrize $\Pi$ in (15) and $D$ in (16) with different couplings. Indeed, a renormalization-group analysis gives a running coupling determined in the spacelike region, while the initial expression (15) contains an integration over timelike momentum and therefore to calculate (16) requires the procedure of analytic continuation from spacelike to timelike momentum.

Separating the QCD contribution $\Delta_\tau$ in $R_\tau$

$$R_\tau = 3(|V_{ud}|^2+|V_{us}|^2)S_{\mathrm{EW}}(1+\Delta_\tau)\,, \qquad (17)$$

where $V_{ud}$ and $V_{us}$ are the CKM matrix elements, and $S_{\mathrm{EW}}$ is the electroweak factor, we obtain the two equivalent representations,

$$\Delta_\tau = 2r_1\int_0^{M_\tau^2}\frac{ds}{M_\tau^2}\left(1-\frac{s}{M_\tau^2}\right)^2\left(1+2\frac{s}{M_\tau^2}\right)\bar{a}_s^{\mathrm{eff}}(s), \qquad (18)$$



and

$$\Delta_\tau = \frac{d_1}{2\pi\mathrm{i}}\oint_{|z|=M_\tau^2}\frac{dz}{z}\left(1-\frac{z}{M_\tau^2}\right)^3\left(1+\frac{z}{M_\tau^2}\right)\bar{a}^{\mathrm{eff}}(z). \qquad (19)$$

It should be noted that the equivalence of these formulae holds only in the case of the above-mentioned analytic properties of the correlator $\Pi(s)$ and $D$-function and that these analytic properties are broken in the standard perturbation theory. The QCD contribution represented in the form (16) is the expression which one usually uses for theoretical analysis. In principle, the expression (19) can be calculated on the basis of perturbation theory, but then it is impossible to return from (19) to (18) which corresponds to the initial Eq. (15), and nothing can be said about the error associated with switching from (18) to (19). Therefore, it is impossible to give in the framework of the standard perturbation theory a self-consistent description of the inclusive decay of a $\tau$ lepton into hadrons. The method of APT allows one to avoid the above-mentioned difficulties and evaluate both the initial integral over the physical region and the contour representation which are equal due to the Cauchy theorem. We underscore once again that the APT makes it possible to implement the correct transition from expression (15) to (16). These expressions simply coincide, as they should, while the application of perturbation theory with the standard renormalization-group refinement runs into serious difficulties.

The fundamental quantity in the APT approach is the spectral density $\varrho(\sigma)$ by which one can parametrize both the running couplings in the spacelike and in the timelike regions. We now find a formula which expresses the strong interaction contribution to $R_\tau$ via the spectral density function. To this end, introduce an effective spectral density $\rho^{\mathrm{eff}}(\sigma)$ that corresponds to the effective coupling. The QCD correction has the form

$$\Delta_\tau = \frac{d_1}{\pi}\int_0^\infty\frac{d\sigma}{\sigma}\rho^{\mathrm{eff}}(\sigma) - \frac{d_1}{\pi}\int_0^{M_\tau^2}\frac{d\sigma}{\sigma}\left(1-\frac{\sigma}{M_\tau^2}\right)^3\left(1+\frac{\sigma}{M_\tau^2}\right)\rho^{\mathrm{eff}}(\sigma). \qquad (20)$$

Due to the feature of universality, the first term in this equation can be expressed in terms of only the first $\beta$-function coefficient.

The results of the analysis performed in [9, 10, 17] demonstrate the importance of analyticity in the running coupling, not only from the fundamental point of view – a self-consistent theoretical description of $\tau$ decay – but also from the standpoint of giving a self-consistent description of the $Q^2$ evolution of the running coupling and extracting the parameter $\Lambda_{\mathrm{QCD}}$ from the experimental data on $\tau$ decay.

**Renormalization scheme dependence.** Inevitable truncation of the PT series, i.e., the approximation of a physical quantity by one of its partial sums, leads to the known problem of the dependence of the results on the renormalization prescription. Thus, the partial sum of the PT series used in approximating a physical quantity bears a dependence on the choice of the renormalization scheme, which is the source of theoretical ambiguity in describing experimental data. In QCD, such ambiguity is the greater the smaller are the energy parameters characteristic of the process. To solve the stability problem of the results obtained, it is by far not enough to investigate only loop stability within a certain renormalization scheme; one should also consider the scheme stability of the results.

Here, we discuss the scheme arbitrariness arising in the APT in the example of the $R$-ratio for the $e^+e^-$-annihilation process into hadrons. This example is physically interesting for the renormalization scheme (RS) stability issue (see, e.g., discussion in Ref. [29] and references therein). The AA analysis of the process of $e^+e^-$ annihilation into hadrons and investigation of the RS dependence problem have been performed in [14, 18] (see also [19]). In the framework of the nonperturbative $a$-expansion the process of $e^+e^-$ annihilation has been studied in [30].

In passing from one renormalization scheme to another, the coupling constant transforms as

$$a' = a(1 + v_1 a + v_2 a^2 + \cdots). \tag{21}$$

We limit ourselves here to the three-loop level of the $D$-function achieved at present, with the QCD corrections taken in the approximation where

$$d = a(1 + d_1 a + d_2 a^2), \tag{22}$$

with the running charge determined as a solution of the renormalization group equation with the three-loop $\beta$-function

$$\beta(a) = \mu^2 \frac{\partial a}{\partial \mu^2} = -ba^2(1 + b_1 a + b_2 a^2), \tag{23}$$

where

$$b = \frac{33 - 2f}{6}, \quad b_1 = \frac{153 - 19f}{66 - 4f}, \quad b_2^{\overline{\rm MS}} = \frac{77139 - 15099f + 325f^2}{288(33 - 2f)}. \tag{24}$$

The three-loop $\beta$-function coefficient $b_2$ and the expansion coefficients $d_1$ and $d_2$ depend on the choice of the renormalization scheme. Under scheme



transformation (21), they change as

$$\begin{aligned} b_2' &= b_2 - v_1^2 - b_1 v_1 + v_2, \\ d_1' &= d_1 - v_1, \\ d_2' &= d_2 - 2(d_1 - v_1)v_1 - v_2. \end{aligned} \tag{25}$$

Thus, every term in representation (22) undergoes a transformation, and we thus obtain the new function

$$d' = a'(1 + d_1' a' + d_2' a'^2), \tag{26}$$

where the coupling $a'$ is evaluated with the new $\beta$-function, with the three-loop coefficient $b_2$ replaced by the primed one $b_2'$.

Eqs. (26) and the transformation law of the scaling parameter $\Lambda' = \Lambda \exp(v_1/b)$ [31] allow us to write down two scheme invariants [32]

$$\rho_1 = \frac{b}{2} \log \frac{Q^2}{\Lambda^2} - d_1, \qquad \rho_2 = b_2 + d_2 - b_1 d_1 - d_1^2. \tag{27}$$

We normalize the momentum scale at $\Lambda_{\overline{\rm MS}}$. In arbitrary scheme, the invariant charge is then determined from the equation

$$\frac{b}{2} \log \left( \frac{Q^2}{\Lambda^2_{\overline{\rm MS}}} \right) = d_1^{\overline{\rm MS}} - d_1 + \Phi(a, b_2), \tag{28}$$

where

$$\Phi(a, b_2) = \frac{1}{a} - b_1 \log \frac{1 + b_1 a}{\beta_0 a} + b_2 \int_0^a \frac{dx}{(1 + b_1 x)(1 + b_1 x + b_2 x^2)}. \tag{29}$$

Although there are no general arguments to prefer a certain renormalization scheme from the start, we nevertheless can define a class of "natural" schemes, which look reasonable at the three-loop level that we consider. The relevant criterion was proposed in [33]. One should restrict oneself to the schemes where the cancellations between different terms in the second scheme invariant (27) are not too large. Quantitatively, this criterion can be related to the cancellation index

$$C = \frac{1}{|\rho_2|} (|b_2| + |d_2| + d_1^2 + |d_1||b_1|). \tag{30}$$

One should of course keep in mind the conventions involved in these considerations, in particular as regards the minimal value of the cancellation index.

Given a certain maximum value of the cancellation index $C_{\max}$, we can investigate stability of the results obtained by taking different schemes with the index $C \le C_{\max}$. As $C_{\max}$, we take the index corresponding to the optimal RS scheme based on the principle of minimal sensitivity (PMS). We then have a relatively small class of "admissible" schemes bounded by the maximal index $C_{\rm PMS}$.

Consider the RS-invariant $e^+e^-$ annihilation cross-section ratio

$$R(s) = 3\sum_f Q_f^2\,[1 + r_f(s)], \quad r_f(s) = \tilde{a}(s)\left[1 + r_1\tilde{a}(s) + r_2\tilde{a}^2(s)\right], \quad (31)$$

where we wrote the QCD contribution, $r_f(s)$, in the third order for the massless case. The function $\tilde{a}(s)$ and coefficients $r_k$ depend of the flavor number $f$. The function $\tilde{a}(s)$, "the running coupling in the timelike region", usually, is defined naively as a mirror image $\tilde{a}(-Q^2) = a(Q^2)$. Instead, we use the self-consistent analytic approach.

Expansion for the QCD correction $r(s)$ is similar to the one for the RS-invariant Adler function $D(Q^2)$

$$d_f(Q^2) = a(Q^2)\left[1 + d_1 a(Q^2) + d_2 a^2(Q^2)\right]. \quad (32)$$

The effective spectral density $\varrho_f^{\rm eff}(\sigma)$ is represented by an expansion

$$\varrho_f^{\rm eff}(\sigma) = \rho_0(\sigma) + d_1\varrho_1(\sigma) + d_2\varrho_2(\sigma),$$

where the quantities in the r. h. s. depend on $f$. The first term, $\rho_0(\sigma)$, in the last expression is just the spectral function for $a(Q^2)$ and $\varrho_k(\sigma) = {\rm Im}[a(-\sigma - {\rm i}\epsilon)]^{k+1}$ are related to its higher powers. It is essential that the Adler function is defined in the Euclidean region where the renormalization group method can be applied directly.

For $R(s)$, the cancellation index $C_R$ is evaluated using the known coefficients $r_1$ and $r_2$ of the perturbative expansion of the correction $r = a(1 + r_1 a + r_2 a^2)$. For the PMS-scheme, it is $C_{\rm PMS} \simeq 2$. To demonstrate the scheme arbitrariness arising here, we choose two schemes from this class. The first one is the $H$ scheme with the parameters $r_1^{\rm (H)} = -3.2$ and $b_2^{\rm (H)} = 0$ (the 't Hooft scheme), and the second is the $\overline{\rm MS}$-scheme corresponding to the parameters $r_1^{(\overline{\rm MS})} = 1.64$ and $b_2^{(\overline{\rm MS})} = 4.47$. These schemes are close to each other and to the boundary cancellation index $C_{\rm H} \simeq C_{\overline{\rm MS}} \simeq C_{\rm PMS} \simeq 2$.



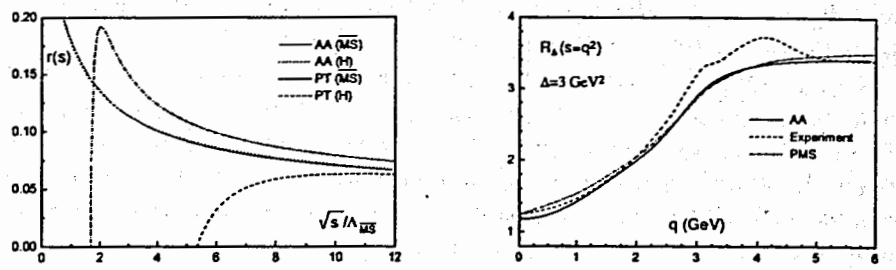


Figure 2: On the left. *Plot of the QCD correction $r_{f=3}(s)$ calculated in the cases of perturbation theory* (PT) *and the analytic approach* (AA) *in two different RS's with approximately the same cancellation index $C_R \simeq 2$: H and* $\overline{\rm MS}$. On the right. *The smeared $e^+e^-$ annihilation ratio $R_\Delta(q^2)$.*

In Fig. 2 (on the left), we plot the QCD correction $r_{f=3}(s)$ as a function of $\sqrt{s}/\Lambda_{\overline{\rm MS}}$ for these two schemes in the usual treatment, as it was considered, e.g., in [34, 29, 35] and within the AA. One can see that the analytically improved result for $R(s)$ obeys a stable behavior for the whole interval of energies being practically scheme-independent. The RS stability of the IAA predictions has also been observed for the Bjorken and Gross-Llewellyn Smith sum rules and for the semileptonic $\tau$-decay [15, 16, 17].

To incorporate threshold effects and compare our results with experiment, we use for the cross-section ratio an approximate expression suggested in [36]

$$\tilde{R}(s) = 3\sum_f Q_f^2\,\Theta(s - 4m_f^2)\,T(v_f)\,[1 + g(v_f)r_f(s)], \quad (33)$$

where

$$v_f = \sqrt{1 - \frac{4m_f^2}{s}},\ T(v) = \frac{v(3 - v^2)}{2},\ g(v) = \frac{4\pi}{3}\left[\frac{\pi}{2v} - \frac{3 + v}{4}\left(\frac{\pi}{2} - \frac{3}{4\pi}\right)\right],$$

and consider the "smeared" quantity [36]

$$R_\Delta(q^2) = \frac{\Delta}{\pi}\int_0^\infty ds \frac{\tilde{R}(s)}{(s - q^2)^2 + \Delta^2}. \quad (34)$$

In Fig. 2 (on the right) we show smeared experimental data for $R_\Delta(q^2)$ at $\Delta = 3\,{\rm GeV}^2$ and the third-order PMS curve taken from [34]. In the

same figure we plot the AA three-loop result obtained with the value of the scale parameter as in [14] matched according to [11].

**Conclusion.** We have considered the analytic approach to QCD and some its applications. The general principles of the theory, the consequence of which the certain analytic properties of the running coupling, lead to the essential stability of the running coupling behavior in the infrared region with respect to many loop correction. Here, the prime point is the universal value of the analytic coupling at $Q^2 = 0$.

The results of analysis performed in the framework of the analytic approach demonstrate the importance of the running coupling analyticity, not only from the fundamental point of view – a correct theoretical description of $\tau$ decay, but also from the standpoint of giving a description of the $Q^2$ evolution of the running coupling and extracting the parameter $\Lambda_{\rm QCD}$ from the experimental data on $\tau$ decay. The analytic properties play a key role in self-consistent definition of the running coupling in the timelike region.

Analytic perturbation theory reduces the RS dependence drastically. Physical quantities thus obtained turn out to be practically scheme independent in a wide class of RS for the whole energy interval. We have also demonstrated that the AA description agrees with experimental data for the smeared $e^+e^-$ annihilation ratio.

The author would like to express sincere thanks to professors D.V. Shirkov and K.A. Milton and to Dr. O.P. Solovtsova for fruitful collaboration and helpful discussions.

*REFERENCES*

[1] N.N. Bogoliubov and D.V. Shirkov, Dokl. Akad. Nauk SSSR **103** (1955) 203; 391.
[2] N. N. Bogoliubov and D. V. Shirkov, JETP **30** (1956) 77; Nuovo Cim. **3** (1956) 845.
[3] N.N. Bogoliubov, A.A. Logunov and D.V. Shirkov, Sov. Phys. JETP **10** (1959) 574.
[4] N.N. Bogoliubov and D.V. Shirkov, *Introduction to the Theory of Quantum Fields*. "Nauka", Moscow, 1986.
[5] D.V. Shirkov and I.L. Solovtsov, JINR Rapid Comm. No. 2[76]-96 (1996) 5.
[6] D.V. Shirkov and I.L. Solovtsov, Phys. Rev. Lett. **79** (1997) 1209.
[7] K.A. Milton and I.L. Solovtsov, Phys. Rev. D **55** (1997) 5295.



[8] D.V. Shirkov, Nucl. Phys. (Proc. Suppl.) **B64** (1998) 106.
[9] O.P. Solovtsova, JETP Lett. **64** (1996) 714.
[10] K.A. Milton, I.L. Solovtsov and O.P. Solovtsova, Phys. Lett. **B415** (1997) 104.
[11] K.A. Milton and O.P. Solovtsova, Phys. Rev. D **57** (1998) 5402.
[12] K.A. Milton and I.L. Solovtsov, Phys. Rev. D **59** (1999) 107701.
[13] D.V. Shirkov, Theor. Math. Phys. **119** (1999) 55.
[14] I.L. Solovtsov and D.V. Shirkov, Phys. Lett. **B442** (1998) 344.
[15] K.A. Milton, I.L. Solovtsov and O.P. Solovtsova, Phys. Lett. **B439** (1998) 421.
[16] K.A. Milton, I.L. Solovtsov and O.P. Solovtsova, Phys. Rev. D **60** (1999) 016001.
[17] K.A. Milton, I.L. Solovtsov and O.P. Solovtsova, Proceedings of the XXIX Int. Conference on High Energy Physics, Vancouver, B.C., Canada, July 23-29, Vol. II (1998) 1608, hep-ph/9808457.
[18] D.V. Shirkov and I.L. Solovtsov, Talk given at the International Workshop "$e^+e^-$ collisions from $\phi$ to $J/\Psi$", Novosibirsk, March 1-5, 1999 (to be published in the Proceedings), hep-ph/9906495.
[19] I.L. Solovtsov and D.V. Shirkov, Theor. Math. Phys. **120** (1999) 482.
[20] A.V. Radyushkin, Preprint JINR, E2-82-159, 1982, JINR Rapid Comm. No. 4[78]-96 (1996) 9.
[21] M.R. Pennington, G.G. Ross, Phys. Lett. **102** B (1981) 167.
[22] N.V. Krasnikov, A.A. Pivovarov, Phys. Lett. **B116** (1982) 168.
[23] J.D. Bjorken, Preprint, SLAC-PUB-5103, 1989; Proceedings of the Cargese Summer Institute, Cargese, France, 1989, ed. M. Levy *et al.*, NATO Advanced Institute, Series B: vol. 223, Plenum, New York, 1990.
[24] I.L. Solovtsov, Phys. Lett. **B327** (1994) 335; Phys. Lett. **B340** (1994) 245.
[25] H.F. Jones and I.L. Solovtsov, Phys. Lett. **B349** (1995) 519.
[26] H.F. Jones, I.L. Solovtsov and O.P. Solovtsova, Phys. Lett. **B357** (1995) 441.
[27] J. Schwinger, Proc. Natl. Acad. Sci. USA **71** (1974) 3024; 5047.
[28] E. Braaten, Phys. Rev. Lett. **60** (1988) 1606; E. Braaten S. Narison and A. Pich, Nucl. Phys. **B373** (1992) 581.
[29] P.A. Raczka and A. Szymacha, Phys. Rev. D **54** (1996) 3073.
[30] I.L. Solovtsov and O.P. Solovtsova, Phys. Lett. **B344** (1995) 377.
[31] W. Celmaster and R.J. Gonsalves, Phys. Rev. D **20** (1979) 1420.
[32] P.M. Stevenson, Phys. Rev. D **23** (1981) 2916.
[33] P.A. Raczka, Z. Phys. **C 65** (1995) 481.
[34] A.C. Mattingly and P.M. Stevenson, Phys. Rev. D **49** (1994) 437.
[35] J. Chyla, A.L. Kataev and S.A. Larin, Phys. Lett. **B267** (1991) 269.
[36] E.C. Poggio, H.R. Quinn and S. Weinberg, Phys. Rev. D **13** (1976) 1958.

# Nucleon electromagnetic form factors in a single-time constituent quark model

**Ilichova T.P., Shulga S.G.**

*Skaryna University, Gomel, LPP JINR, Dubna*

Abstract

The main statement of the nucleon constituent quark model with a fixed number of particles as basic ansatz are considered in a framework of the single-time (quasipotential) approach to the bound state problem. The scaling law breacking for the proton form factor=20 are investigated for=20 $Q^2 = 0 \div 2\text{Gev}^2$.

The problem of the relativistic treatment of the constituent quark model (CQM) have been solved by several manners [1, 2, 3], which have general feature - fixed number of the particles assumption and additive assumption for nucleon current expression in terms of quarks currents [5]. A popular approach to the problem is the light-front dynamics [2]. In present work we propose to use the old quasipotential approach [6] for formulation of CQM with fixed number of particles.

In proceeding we suggest that Fock momentum-space for nucleon has $N = 3$ quarks Dirac basis $|\, \alpha_1\mathbf{p}_1, \alpha_2\mathbf{p}_2, \alpha_3\mathbf{p}_3\rangle \equiv |\, \alpha\mathbf{p}\rangle$:

$$|\, \lambda\mathbf{K}\rangle \approx \sum_{\alpha} \int d\Omega_{\mathbf{p}_1} d\Omega_{\mathbf{p}_2} d\Omega_{\mathbf{p}_3} \,|\, \alpha\mathbf{p}\rangle\langle\alpha\mathbf{p} \,|\, \lambda\mathbf{K}\rangle. \qquad (1)$$

We will take it for granted that all nontrivial effects of the QCD vacuum (e.g., gluon and quark-antiquark conde= nsates) can be absorbed into the effective parameters of the CQM.

To find a equation for wave function (WF) $\langle\alpha\mathbf{p} \mid \lambda\mathbf{K}\rangle$ we consider covariant single-time WF [7] ($N = 3$):

$$\Psi^{QP}_{\lambda\mathbf{K},\alpha}(x) = \Psi^{BS}_{\lambda\mathbf{K},\alpha}(x)\delta(n_K(x_1 - x_2)) \dots \delta(n_K(x_{N-1} - x_N)),$$
$$\Psi^{BS}_{\lambda\mathbf{K},\alpha}(x) = \langle 0 \mid T[\phi^{(1)}_{\alpha_1}(x_1) \dots \phi^{(N)}_{\alpha_N}(x_N)] \mid \lambda\mathbf{K}\rangle, \qquad (2)$$

where $\Psi^{BS}_{\lambda\mathbf{K},\alpha}(x)$ is Bethe-Salpeter WF; $(n_K)_\mu = \frac{K_\mu}{\sqrt{K^2}} = \frac{K_\mu}{M_n}$ - 4-velocity, $\delta$-functions in (2) covariantly equal times in the center-of-mass of system.

=20 Using a translational invariance $\phi(x_i) = \exp(i\hat{H}t_i)\phi(0, \mathbf{x}_i)\exp(-i\hat{H}t_i)$, expression $\phi_\alpha(0, \mathbf{x}) = 1/(2\pi)^3 \int d\Omega_q \sum_r \left[b_r(\mathbf{q})u^{(r)}_\alpha(\mathbf{q})\exp(-iqx) + \dots\right]$ and



according to fixed number of particles assumption notice that the anti-particle operator do not give a contribution into the one-time WF we can obtain the Fourier-momentum representation WF (2) ($D$ - the Wigner rotation matrix;$\overset{o}{\mathbf{p}} \equiv \overset{o}{\mathbf{p}}_1, \overset{o}{\mathbf{p}}_2, \overset{o}{\mathbf{p}}_3$, $\overset{o}{\mathbf{p}}_i = \vec{L}^{-1}_K p_i$) [8, 7, 9]:

$$\tilde{\Psi}_{\lambda\mathbf{K},\alpha}(p) = (2\pi)\delta^{(1)}(\overset{o}{P}_0 - M_P)\left[\sum_r \prod_{i=1}^N u^{(r'_i)}_{\alpha'_i}(\mathbf{p}_i)\prod_{i=1}^N \overset{+}{D}{}^{r'_i r_i}_K(p_i)\right]\langle r\ \overset{o}{\mathbf{p}}|\ \lambda\mathbf{0}\rangle$$
$$= (2\pi)\delta^{(1)}(\overset{o}{P}_0 - M_P)\prod_{i=1}^N u^{(r_i)}_{\alpha_i}(\mathbf{p}_i)\langle r\mathbf{p} \mid \lambda\mathbf{K}\rangle. \qquad (3)$$

As in [7] we determine WF projection into positive-frequencial states:

$$\tilde{\Psi}^{(+)(r)}_{\lambda\mathbf{K}}(p) \equiv \bar{u}^{r_1}_{\alpha_1}(\mathbf{p}_1)\dots\bar{u}^{r_N}_{\alpha_N}(\mathbf{p}_N)\tilde{\Psi}_{\lambda\mathbf{K},\alpha}(p) = 2\pi\delta(\overset{o}{P}_0 - M_P)\langle r\mathbf{p} \mid \lambda\mathbf{K}\rangle; \quad (4)$$

$$\langle r\mathbf{p} \mid \lambda\mathbf{K}\rangle = (2\pi)^3\delta^{(3)}(\sum_{i=1}^N \overset{o}{\mathbf{p}}_i)\prod_{i=1}^N \overset{+}{D}{}^{r'_i r_i}_K(p_i)\Phi^{(+)(r)}_{\lambda 0}(\overset{o}{\mathbf{p}}). \quad (5)$$

The connection established between CQM WF with fixed number of particle $\langle r\mathbf{p} \mid \lambda\mathbf{P}\rangle$ and WF $\Phi^{(+)(r)}_{\lambda 0}$ give us a chance to obtain equation for relative motion WF by standart form [6, 7]($\sum \overset{o}{\mathbf{p}}_i = \sum \overset{o'}{\mathbf{p}}_i = 0$):

$$(\sum E^o_{\mathbf{p}_i} - M_P)\Phi^{(+)(r)}_{\lambda 0}(\overset{o}{\mathbf{p}}) = \int \prod_{i=2}^N d\Omega_{\overset{o'}{\mathbf{p}}_i} V^{(r'r)}(\overset{o}{\mathbf{p}}, \overset{o'}{\mathbf{p}})\Phi^{(+)(r')}_{\lambda 0}(\overset{o'}{\mathbf{p}}) \qquad (6)$$

To construct a three-particle state with given total angular momentum $J = 1/2$ and helisity $\lambda$ we use the same method as in Ref. [10]:

$$\Phi^{(+)(r)}_{\lambda 0}(\overset{o}{\mathbf{p}}_1, \overset{o}{\mathbf{p}}_2, \overset{o}{\mathbf{p}}_3) = \varphi^{model}_0 \chi^{SU(6)}_\lambda(r_1, r'_2, r'_3)D^{(r_2, r'_2)}_{(p_2+p_3)}(\overset{o'}{\mathbf{p}}_2)D^{(r_3, r'_3)}_{(p_2+p_3)}(\overset{o'}{\mathbf{p}}_3), \quad (7)$$

where $\overset{o'}{\mathbf{p}}_1 = -\overset{o'}{\mathbf{p}}_2 = \vec{L}^{-1}_{p_1+p_2}$. We used the oscillator WF [11] and Coulomb-like WF for calculati= on of the proton form factor:

$$\varphi^{osc}_0 = N\exp\left[-\frac{2m}{3\gamma^2}\left(E^o_{\mathbf{p}_1} + E^o_{\mathbf{p}_2} + E^o_{\mathbf{p}_3} - 3m - \sum_{i\neq k}\frac{(\overset{o}{\mathbf{p}}_i\overset{o}{\mathbf{p}}_k)}{\sqrt{(E^o_{\mathbf{p}_i}+m)(E^o_{\mathbf{p}_k}+m)}}\right)\right];$$
$$\varphi^{Coulomb}_0 = N/(E^o_{\mathbf{p}_1} + E^o_{\mathbf{p}_2} + E^o_{\mathbf{p}_3})^2 - 9m^2 + \gamma^2)^2. \qquad (8)$$

Let us consider electromagnetic current matrix element. Assuming that $J_\mu(0) = \sum_{s=1}^N j^{(s)}_\mu(0)$ we first expand in sets of free-particle states (1) and current matrix element takes the form:

$$\langle n'\mathbf{P}'|J_\mu(0)|n\mathbf{0}\rangle = \sum_{s=1}^N \int \prod_{k=1}^N d\Omega_{\mathbf{p}'_k} d\Omega_{\mathbf{p}_k} \sum_{\alpha',\alpha} \langle n'\mathbf{P}'|\alpha'\mathbf{p}'\rangle\langle\alpha'\mathbf{p}|j^{(s)}_\mu(0)|\alpha\mathbf{p}\rangle\langle\alpha\mathbf{p}|n\mathbf{0}\rangle.$$

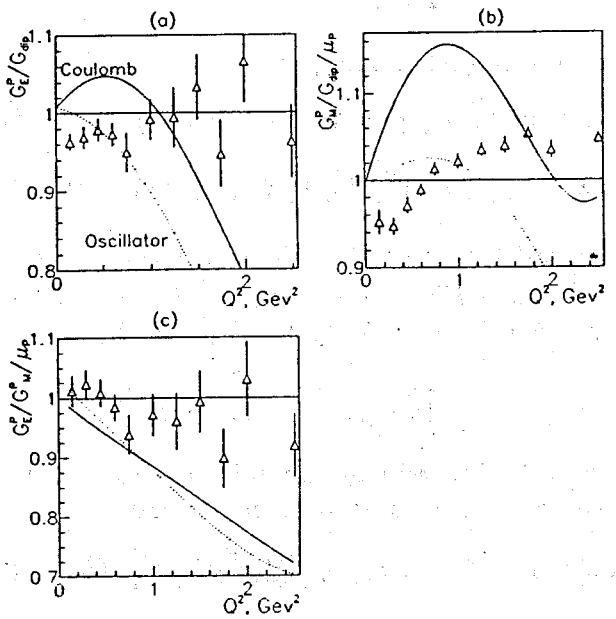


Figure 1: $G_E^P/G_{dip}$, $G_M^P/G_{dip}/\mu_P$ and $G_E^P/G_M/\mu_P$ *in oscillato= r and Coulomb-like model with best parameters for fit : Coulomb (solid curve):* $m_q = 150Mev, \gamma^2 = 0.5Gev^2$ *; Oscillator (dashed curve):* $m_q = 162$ *Mev,*$\gamma^2 = 0.35$ *Gev*$^2$. *Experimental data from [4].* $G_{dip} = 1/(1 + Q^2/0.71)$.



For 3-quark system with symmetrical WF we obtained ($\overset{o}{\mathbf{p}}'_1 + \overset{o}{\mathbf{p}}_2 + \overset{o}{\mathbf{p}}_3 = \mathbf{p}_1 + \mathbf{p}_2 + \mathbf{p}_3 = 0$):

$$\langle n'\mathbf{P}'|J_\mu(0)|n\mathbf{0}\rangle = 3\int d\Omega_{\mathbf{p}_2} d\Omega_{\mathbf{p}_3} \frac{m^2}{\overset{o}{E}_{\mathbf{p}_2+\mathbf{p}_3}\overset{o}{E}_{\mathbf{p}_2+\mathbf{p}_3}} \overset{\star}{\Phi}{}^{(+)(r'_1,r'_2,r'_3)}_{\lambda' 0}(\overset{o}{\mathbf{p}}'_1, \overset{o}{\mathbf{p}}_2, \overset{o}{\mathbf{p}}_3) *$$
$$* D^{r'_1\alpha'_1}_{P'}(\mathbf{p}'_1) j_\mu^{\alpha'_1\alpha_1}(\mathbf{p}'_1, \mathbf{p}_1) D^{r'_2\alpha_2}_{P'}(\mathbf{p}_2) D^{r'_3\alpha_3}_{P'}(\mathbf{p}_3) \Phi^{(+)(\alpha_1,\alpha_2,\alpha_3)}_{\lambda 0}(\mathbf{p}_1, \mathbf{p}_2, \mathbf{p}_3) \quad (9)$$

If $\overset{o}{\mathbf{s}} = 0$ then $s = \frac{\overset{o}{s}_0}{M_P} P$ and f= or $s = p'_1 + p_2 + p_3, s = p_1 + p_2 + p_3$ we have

$$p'_1 + p_2 + p_3 = P' \frac{\overset{o}{E}_{\mathbf{p}'_1} + \overset{o}{E}_{\mathbf{p}_2} + \overset{o}{E}_{\mathbf{p}_3}}{M_P}; p_1 + p_2 + p_3 = P \frac{E_{\mathbf{p}_1} + E_{\mathbf{p}_2} + E_{\mathbf{p}_3}}{M_P}. \quad (10)$$

Thus, (9) approximatly satisfies to current conservation condition: if $(p'_1 - p_1)_\mu \langle \alpha'_1 \mathbf{p}'_1 | j_\mu^{(1)}(0) | \alpha_1 \mathbf{p}_1 \rangle = 0$ then $(P' - P)_\mu \langle n'\mathbf{P}'|J_\mu(0)|n\mathbf{0}\rangle \approx \approx 0$, $P$=$(M_n, \mathbf{0})$. The numerical calculation are shown that this condition approximatly satisfy for wide region of the model parameters. 6 - dimensional integrals of this model calculated by the Monte-Carlo method.

Eq. (9) in nonrelativistic limit (additive quark model) is given by:

$$\langle n'\mathbf{P}'|J_\mu(0)|n\mathbf{0}\rangle \approx 3 \overset{\star}{\chi}{}^{\alpha'_1,\alpha_2,\alpha_3}_{\lambda'} \langle \alpha'_1 \mathbf{P}'|j_\mu^{(1)}(0)|\alpha_1 \mathbf{0}\rangle \chi^{\alpha_1,\alpha_2,\alpha_3}_\lambda F(t), \quad (11)$$

where form factor is $F(t) = \int d\Omega_{\mathbf{p}_2} d\Omega_{\mathbf{p}_3} \overset{\star}{\varphi}_0(\overset{o}{\mathbf{p}}'_1 \overset{o}{\mathbf{P}}_2, \overset{o}{\mathbf{P}}_3) \varphi_0(\mathbf{p}_1, \mathbf{p}_2, \mathbf{p}_3)$. Relation (11) provides the scaling law of the space-like Sachs nucleon form factors=20 ($G_E^P \approx G_M^P/\mu_P$). Dziembowski [2] obtained that the so-called soft contributions (CQM) reproduce the experimental data extremely well=20 up to the scale $Q^2 \approx 2.5\ GeV^2$ for the nucleon. Analogous results were obtaited by Cardarelli [2] within light-front CQM without quark form factors. We have reproduced it in our model (see fig. 1, experimental data from [4]). The Coulomb-like model describe best the experimental data up to=20 $Q^2 \approx 3\ GeV^2$ for quark mass $m_q = 166Mev, \gamma^2 = 1.1Gev^2$. The magnetic moment ($\mu_P = G_M(0)$) was become in this model (with $\gamma^2 = 1.1Gev^2$) for $m_q = 105$Mev but $G_E^P/G_{dip} \gg 1, G_M^P/G_{dip}/\mu_P \gg 1$ for $Q^2 = 0 \div 2Gev^2$, $(G_{dip} = 1/(1 + Q^2/0.71)$.

# References

[1] R.Bijker, F.Iachello and A.Levitan//Ann.Phys.(N.Y.)**236**(1994)69; F.Iachello and A.Levitan//Phys.Rev. **C54**(1996)1935. S.Capstick and B.D.Keister//Phys.Rev.**D51**(1995)3598.

[2] Z.Dziembowski//Phys.Rev.**D37**(1988)778. F.Cardarelli e. a. // Phys.Lett.**B357**(1995)267. F.Schlumpf//Phys.Rev.**D47**(1993)4114. F.Coester, K.Dannbom, D.O.Riska//Nucl.Phys.**A634**(1998)335.

[3] P.-L.Chung,F.Coester//Phys.Rev.**D44**(1991)229. F.Cardarelli e.a.//Few Body Syst.Suppl.**11**(1999)66.

[4] R.C.Walker e.a.//Phys.Lett.**B224**(1989)353; **B240**(1990)522(E); P.E.Bosted e.a.//Phys.Rev.Lett.**68**(1992)3841; A.F.Sill e.a.// Phys.Rev.**D48**(1993)29; R.C.Walker e.a.//Phys.Rev.**D49**(1994) 5671; L.Andivahis e.a.//Phys.Rev.**D50**(1994)5491.

[5] A.P.Kobushkin, V.P.Shelest// Sov.Journ.Part.Nucl.**14**(1983)1146.

[6] A.A. Logunov, A.N. Tavkhelidze//Nuovo Cimento. **29**(1963)380.

[7] R.N.Faustov//Ann.Phys.**78**(1973)176.

[8] E.Wigner//Ann.Math.**40**(1939)149. Yu.M.Shirokov//Dokl.Akad.Nauk SSSR.**99**(1954)737.

[9] N.B.Skachkov, I.L.Solovtsov//Sov.Journ.Part.and Nucl 9(1978)5. V.A.Karmanov//Nucl.Phys.A 644(1998)1653.

[10] L.A.Kondratyuk, M.V.Terentyev//Yad.Fiz. **31**(1980)1087 (Sov.J.Nucl.Phys. **31**(1980)561).

[11] T.P. Ilichova, S.G. Shulga //In:Second Opened Scientific Conference of Young Scientists and Specialists JINR.Procceding conference. Dubna.(1998)55.



## List of participants

| First name, Family name | Institution, Country |
|---|---|
| Konstantin Afanas'ev | NC PHEP, Belarus |
| Dmitry Aleinikov | IP NASB, Belarus |
| Tatyana Alferova | GSU, Belarus |
| Vasily Andreev | JINR, Russia |
| Viktor Andreev | GSU, Belarus |
| Alexandr Babich | GSTU, Belarus |
| Vladimir Baryshevsky | INP BSU, Belarus |
| Konstantin Batrakov | INP BSU, Belarus |
| Svetlana Belousova | GSU, Belarus |
| Andrei Bogush | IP NASB, Belarus |
| Aleksander Borissov | DESY, Hamburg |
| Oleg Boyarkin | MSPU, Belarus |
| Sergei Chatrchan | JINR, Russia |
| Sergei Cherkas | INP BSU, Belarus |
| Yury Chernichenko | GSTU, Belarus |
| Alberto De Min | CERN |
| Evgeny Dei | GSU, Belarus |
| Oksana Deryuzhkova | GSU, Belarus |
| Didier Ferrere | CERN |
| Liudmila Filimonceva | GSTU, Belarus |
| Aleksander Fursin | GSTU, Belarus |
| Viktor Gaisyonok | SCST, Belarus |
| Aida Galoyan | JINR, Russia |
| Mikhail Galynsky | IP NASB, Belarus |
| Aleksandr Garkun | BSU, Belarus |
| Ashat Gazisov | IP NASB, Belarus |
| Petr Glasov | GSTU, Belarus |
| Vladimir Gritsev | IP NASB, Belarus |
| Petr Homyakov | BSU, Belarus |
| Aleksander Il'ichev | NC PHEP, Belarus |
| Tatyana Il'icheva | JINR, Russia |
| Aleksei Illarionov | JINR, Russia |
| Igor Ivanov | JINR, Russia |
| Laslo Jenkovsky | INP, Ukrain |
| Leonid Kadovba | IMMPS, Belarus |
| Elena Kalantai | GSU, Belarus |
| Valery Kapshai | GSU, Belarus |
| Ivan Karnaukhov | KIPT, Ukrain |
| Vladimir Kashkan | IP NASB, Belarus |
| Andrei Khomich | NC RHEP, Belarus |
| Vadim Khotilovich | NC PHEP, Belarus |
| Elena Kokoulina | GSTU, Belarus |
| Maksim Komogorov | JINR, Russia |
| Evgeny Korshunov | GSTU, Belarus |
| Lidiya Korsun | GSTU, Belarus |
| Eduard Kuraev | JINR, Russia |
| Sergei Kurlovich | GSTU, Belarus |
| Yuri Kurochkin | IP NASB, Belarus |
| Vyacheslav Kuvshinov | IP NASB, Belarus |
| Polina Kuzhir | NC PHEP, Belarus |
| Andrei Kuzmin | IP NASB, Belarus |
| Maksim Kuzmin | JINR, Russia |
| Rupert Leitner | CERN |
| Michail Levchuk | IP NASB, Belarus |
| Dmitry Linkevich | NPSU, Belarus |
| Wolfgang Lohmann | DESY, Zeuthen |
| Vasily Lyashkevich | GSTU, Belarus |
| Viktor Mahnach | IP NASB, Belarus |
| Nikolai Maksimenko | GSU, Belarus |
| Aleksandr Margolin | NC PHEP, Belarus |
| Viktor Matveev | INR, Russia |
| Emilio Meschi | CERN |
| Oleg Metelitsa | INP BSU, Belarus |
| Sergei Mishin | JINR, Russia |
| Maksim Nazarenko | JINR, Russia |
| Mikhail Nemchenko | IMMPS, Belarus |
| Aleksandr Pankov | GSTU, Belarus |
| Yuri Pleskachevsky | IMMPS, Belarus |
| Igor Potrap | JINR, Russia |
| Aleksander Prohorov | JINR, Russia |
| Fedor Prokoshin | JINR, Russia |
| Valery Prokoshin | SCST, Belarus |
| Vitaly Pronskih | JINR, Russia |
| Sergei Rahmanov | BSU, Belarus |
| Herbert Rohringer | CERN |
| Viktor Rumyantsev | NC PHEP, Belarus |
| Elena Russakovich | JINR, Russia |
| Nikolai Russakovich | JINR, Russia |
| Nikolai Sakhno | GSU, Belarus |
| Maria Savina | JINR, Russia |
| Sergei Scherbakov | GTU, Belarus |
| Anna Sen'ko | GRSU, Grodno |
| Albert Shaginyan | GSTU, Belarus |
| Valery Shaporov | IP NASB, Belarus |
| Gennady Shatilo | GSTU, Belarus |
| Binuradden Shaykhatdenov | JINR, Russia |
| Leonid Shemetkov | GSU, Belarus |
| Vitaly Shevtsov | NC PHEP, Belarus |
| Tatyana Shishkina | BSU, Belarus |
| Sergei Shmatov | JINR, Russia |
| Sergei Shulga | JINR, Russia |
| Nikolai Shumeiko | NC PHEP, Belarus |
| Aleksei Sissakyan | JINR, Russia |
| Nikolai Skachkov | JINR, Russia |
| Anna Skachkova | JINR, Russia |
| Il'ya Slepnev | JINR, Russia |
| V. Smirnov | IMMPS, Belarus |
| Igor Solovtsov | JINR, Russia |
| Aleksandr Soroko | NC PHEP, Belarus |
| Pavel Starovoitov | NC PHEP, Belarus |

## List of participants

| | |
|---|---|
| Nadegda Stepanova | Ministry of Finance, Belarus |
| Vasily Strazhev | Ministry of Education, Belarus |
| Vladimir Strotsky | NC PHEP, Belarus |
| Juan Suares | NC PHEP, Belarus |
| Sergei Sushkov | NC PHEP, Belarus |
| Anatoly Sverg | Ministry of Finance, Belarus |
| Stefan Tapprogge | CERN |
| Viktor Tikhomirov | INP BSU, Belarus |
| Sergei Timoshin | GSTU, Belarus |
| Arkady Tolkachev | NC PHEP, Belarus |
| Lev Tomilchik | IP NASB, Belarus |
| Chris Tully | CERN |
| Gennady Tyumenkov | GSU, Belarus |
| Vladimir Uzhinsky | JINR, Russia |
| Irina Zainakova | GSTU, Belarus |
| Pavel Zarzhitsky | NC PHEP, Belarus |
| Fedor Zyazyulya | NC PHEP, Belarus |
| Vladimir Zykunov | GSTU, Belarus |



**Proceedings of International School–Seminar «Actual Problems of Particle Physics»**

**Труды международной школы–семинара «Актуальные проблемы физики частиц»**

**E1,2-2000-208**

Том I

Ответственные за подготовку сборника к печати
П.Старовойтов, С.Шульга

Рукопись сборника поступила 06.09.2000. Подписано в печать 25.09.2000
Формат 60 × 90/16. Офсетная печать. Уч.-изд. листов 14,0
Тираж 170. Заказ 52237

Издательский отдел Объединенного института ядерных исследований
Дубна Московской области